



**TECHNISCHE
UNIVERSITÄT
DRESDEN**



Atomic Energy Commission of Syria

Assessment of Low-Dose Radiotoxicity in Microorganisms and Higher Organisms

DISSERTATION

zur Erlangung des akademischen Grades

Doctor rerum naturalium
(Dr. rer. nat.)

Vorgelegt

der Fakultät Mathematik und Naturwissenschaften
der Technischen Universität Dresden

Von

M.Sc. Muhammad Hassan Obeid

geboren am 04.11.1983 in Damaskus, Syrien

Eingereicht am 27.10.2015

Verteidigt am 11.01.2016

Gutachter:

Prof. Dr. Thorsten Stumpf Helmholtz-Zentrum Dresden- Rossendorf (HZDR)

Prof. Dr. Karim Fahmy Helmholtz-Zentrum Dresden- Rossendorf (HZDR)

Die Dissertation wurde in der Zeit von Februar 2012 bis Oktober 2015 im Institut für Ressourcenökologie des Helmholtz-Zentrums Dresden-Rossendorf angefertigt.

Dedication

To each person who stood by me during my work, and to any person who may scientifically benefit from it, I dedicate this thesis.

Dresden, Germany, the 27th of October 2015.

Muhammad Hassan Obeid

Acknowledgements

I cannot recall in which book of biology I read the likening of cell biology to the wonderland of Alice from the English novel “Alice’s Adventure in Wonderland” by Lewis Carroll. When I browsed the web to check it up, I found that there were a lot of researchers in cell biology who had used this motif when describing how amazing and interesting the systems they investigated were. Frankly speaking, any person who would have watched the eight-minute-movie “Inner life of the cell”¹ on YouTube, and saw how Kinesin (a motor protein) “carries” its cargo and “walks” along its microtubule track to transport it from one compartment to another in the cell, would undoubtedly agree with the fact that the inner life of the cell looks like a wonderland. Sometimes I wonder how “Alice’s Adventure in Wonderland” would look like if Lewis Carroll could have ever had the chance to watch that movie! It was this kind of movie that I knew that I would never get enough of, and now with every time I watch it I get goosebumps with the same feelings as I did the first time of amazement and awe from realizing how complicated our bodies are and how great our creator is. However, Alice would have never made it into the wonderland without eating those pieces of cake and mushroom to scale her body to the needed size. This makes all microscopy, spectroscopy, and any other biophysical method the tasty cookies that scientists needed in order to get into the world of molecular cell biology, and later to make it possible to produce that movie.

In this work, I was introduced to microcalorimetry as a tool to investigate the effects of radiotoxicity on the cellular metabolism under environmentally

¹ <https://www.youtube.com/watch?v=FzcTgrxMzZk>

Acknowledgements

relevant low doses, rather than using known methods based on lethality, which is absent under such low doses. This instrument was my piece of cookie that allowed me to investigate the behavior of the bacterial cells under stressful conditions, and to see them fighting back to protect themselves against toxicity. Although calorimetry has been used since the 1980's to investigate bacterial growth, I was given the honor to be the first student to use it in the field of radiation biophysics and to investigate coupling microcalorimetry with genetics. This scientific breakthrough has shown how this non-specific instrument, which monitors the overall metabolically released heat from a sample, can be related to a very specific interaction when combined with genetics. During my work, the more my knowledge grew, the more I could see that I know nothing. For this, I am all thankful to my almighty God, who granted me these and other uncountable honors and gifts, helped me with each single breath, and guided me to reach this important scientific achievement, without him I am nothing, and I ask him to continue to increase my knowledge. I am thankful to him, and that he has helped me fulfil my dream and finish my higher education in Germany, while surrounding me with the best people I have ever met, without whom the completion of this work would not have been possible, and whose help is gratefully appreciated and sincerely acknowledged:

I am all grateful to my supervisor Prof. Dr. Karim Fahmy, who showed by his friendly personality an example of how an excellent supervisor, besides being an excellent teacher, can be like a father, a brother, and a friend to his student. He was the person who had all the patience in the world, for that he, for many times, listened to me while defending my wrong analyses, and then showed me my committed mistakes with a friendly attitude and a very nice friendly smile on his face. I am thankful to him for giving me the great honor of

Acknowledgements

working in his group. I am thankful to Prof. Dr. Gert Bernhard and Prof. Dr. Thorsten Stumpf for the great honor they gave me by supervising my project, and for all the kindness and friendly relations they showed to me. Knowing the three of them has been a great honor for me.

I am thankful to the Atomic Energy Commission of Syria for the financial support.

I am thankful to Prof. Dr. Marc Solioz, Dr. Jana Oertel, Dr. Andrea Cherkouk, Prof. Dr. Satoru Tsushima, Dr. Sonja Selenska-Pobel, Dr. Johannes Raff, Dr. Matthias Suhr and Dr. Manja Vogel for all the valuable help, advices, and encouragements they gave.

I am thankful to my colleagues in the biophysics group: Dr. Ahmad Sayed, Dr. Lisa Fischermeier, Dr. Sawsan Abu Sharkh, Dr. Enas Attia, Mrs. Jenny Philipp and Ms. Gisela Gabernet-Garriga for advices, encouragements, the friendly atmosphere they provided, and for all the good times we spent together, and special thanks to Mrs. Jenny Philipp for the help in the lab.

I am thankful to Mrs. Monika Dudek and Mrs. Katrin Flemming for their valuable help in the lab.

I am thankful to Dr. Laura Lütke, Dr. Erik Johnstone, Mrs. Aline Ritter, Mrs. Miriam Bader, Dr. Ulrike Weinert, and Dr. Franziska Lederer for the encouragements and help in the lab.

I am thankful to Mr. Jérôme Kretzschmar, Dr. Matthias Schmid, Dr. Juliane März, Dr. Nina Huittinen, Mr. Björn Drobot, Mr. Robert Barthen, and Dr. Sabine Kutschke for the encouragements and valuable advices.

I am thankful to Prof. Dr. Ibrahim Othman the director General of the AECS, Prof. Dr. Mohammad Said Al-Masri, Prof. Dr. Riad Shweikani, Prof. Dr. Hazem Suman, Prof. Dr. Mohammad Hassan Kharita, Dr. Abdalkader

Acknowledgements

Bitar, Mrs. Azza Kashlan and Mr. Issam Khiami for the help, encouragements, and support they provided me with.

I am thankful to my father Dr. Ayman Obeid, my mother, siblings, my wife Ward Al Baghajati (who stood by me and helped me facing the stresses and difficulties with all her patience and love), my daughter Leen (with her delightful smile), and all the members of my family for the endless love, support and encouragements they provided me with, and for all the prayers they did for me. And I am especially grateful to my grandfather Mr. Abdulkarim Albayat for the great deal of trust he put in me.

Ich bedanke mich bei Frau Ursula Gruhl (meiner Vermieterin) und ihrem Mann Herrn Christian Gruhl und meinen Nachbarn: Frau Sylvia Herschel, Herrn Frank Schonert, Frau Katrin Stenker und Herrn Jürgen Kretzschmar für all die Hilfe, Sorge, Liebe und die familiäre Atmosphäre die sie mir und meiner Familie während unseres Aufenthalts in Dresden gegeben haben.

And finally, I am thankful to all my friends and colleagues.

Dresden, Germany, the 27th of October 2015.

Muhammad Hassan Obeid

Contents

Table of Figures	ix
Abstract	1
1 Introduction	3
1.1 Basic aspects about ionizing radiation and its interaction with matter.....	3
1.1.1 Ionizing radiation	3
1.1.2 Basic definitions	5
1.1.3 Direct and indirect effects of ionizing radiation.....	6
1.1.4 Effects of ionizing radiation on biological molecules.....	8
1.1.5 Free radical scavengers	9
1.2 Assessment of chemi- and radiotoxicity of uranium in the low dose regime using metabolic monitoring: Motivations and aims of the study.....	10
1.3 Investigating Bacterial growth by isothermal microcalorimetry.....	13
1.3.1 Bacterial growth	13
1.3.2 Isothermal microcalorimetry	14
1.4 The use of isothermal microcalorimeter to study inhibitory actions on living cells .	17
2 Influence of low concentrations of natural uranium on different bacterial strains isolated form a uranium mining waste pile.....	20
2.1 Abstract.....	20
2.2 Introduction	20
2.3 Materials and Methods	22
2.3.1 Bacterial culture and isothermal calorimetry	22
2.3.2 Data analysis	23
2.3.3 Cell counting measurements	24
2.3.4 Dose estimation	26
2.3.5 Data interpretation and calibration experiments	28
2.4 Results	32
2.4.1 The effect of U_{nat} on the waste pile isolate <i>Lysinibacillus sphaericus</i> JG-A12 .	32
2.4.2 The effect of U_{nat} on the waste pile isolate <i>Lysinibacillus sphaericus</i> JG-B53 .	35
2.4.3 The effect of U_{nat} on the waste pile isolate <i>Paenibacillus</i> JG-TB8.....	37
2.4.4 The effect of U_{nat} on the reference strain <i>Lysinibacillus sphaericus</i> NCTC 9602 40	
2.4.5 Investigation of the effect of U_{nat} at concentrations below 10 μ M	42
2.4.6 Calibration experiments	44
2.5 Discussion.....	48
2.5.1 Distinction of two adaptive regimes of uranyl-dependent bacterial growth	49
2.6 Conclusions	53

Table of Figures

3	Comparison of radiotoxicity and chemitoxicity of uranium	56
3.1	Abstract.....	56
3.2	Introduction	56
3.3	Material and methods	57
3.3.1	Bacterial culture and isothermal calorimetry	57
3.4	Results	59
3.4.1	Effect of the isotope ²³³ U on the metabolic activity of the strain JG-B53 and the reference strain NCTC 9602	59
3.4.2	Effect of the isotope U _{nat} on the isolated strain JG-B53 and the reference strain NCTC 9602:	63
3.5	Discussion.....	66
3.6	Conclusions	71
4	Copper and uranyl toxicity in <i>Lactococcus lactis</i> regulated by intracellular glutathione	74
4.1	Abstract.....	74
4.2	Introduction	75
4.3	Materials and methods.....	78
4.3.1	Bacterial culture and isothermal microcalorimetry	78
4.3.2	Isothermal titration calorimetry of GSH uranyl complex formation.....	78
4.3.3	Continuous turbidity measurements	79
4.4	Results	79
4.4.1	Metabolic activity of <i>L. lactis</i> in the presence of copper	79
4.4.2	Metabolic activity of <i>L. lactis</i> in the presence of uranyl.....	84
4.4.3	Isothermal titration calorimetry of GSH uranyl complex formation.....	88
4.4.4	Continuous turbidity measurements	89
4.5	Discussion.....	91
4.6	Conclusions	94
5	Measuring uranyl-sensitivity in the nematode <i>Caenorhabditis elegans</i>	96
5.1	Abstract.....	96
5.2	Introduction	96
5.3	Materials and Methods	97
5.4	Results and Discussion	98
5.5	Conclusions	100
	Conclusions	101
	Outlooks	103
	References	105

Table of Figures

Figure 1-1: Ionizing radiation vs. non-ionizing radiation.	4
Figure 1-2: The specific energy loss along a charged particle track.	5
Figure 1-3: Direct and indirect effects of ionizing radiation.	6
Figure 1-4: Free radicals formation from water radiolysis.	7
Figure 1-5: Examples of consequences of free radicals interaction with biomolecules.	9
Figure 1-6: Mechanisms of radionuclide–microbe interactions.	12
Figure 1-7: Phases of bacterial growth.	14
Figure 1-8: Isothermal microcalorimeter.	15
Figure 1-9: The thermocouple and the thermopile.	15
Figure 2-1: CFU counting of <i>Lysinibacillus sphaericus</i> JG-B53.	25
Figure 2-2: Light microscopic pictures of the bacterial strains.	27
Figure 2-3: Effect of natural uranium on the metabolic heat flow of <i>Lysinibacillus sphaericus</i> JG-A12.	33
Figure 2-4: Effect of natural uranium on the metabolic heat flow of <i>Lysinibacillus sphaericus</i> JG-B53.	35
Figure 2-5: Effect of natural uranium on the metabolic heat flow of <i>Paenibacillus</i> JG-TB8.	38
Figure 2-6: Effect of natural uranium on the metabolic heat flow of <i>Lysinibacillus sphaericus</i> NCTC 9602.	41
Figure 2-7: Normalized maximal heat flow vs. Uranyl concentration.	43
Figure 2-8: Calibration experiments for retardation vs. initial OD relation.	45
Figure 2-9: Isothermal microcalorimetry experiment with stirrer.	48
Figure 2-10: Comparison of the cell envelopes of A: <i>Lysinibacillus sphaericus</i> strains and B: <i>Paenibacillus</i>	51
Figure 2-11: TEM micrograph of isolated S-layer of <i>Lysinibacillus sphaericus</i> JG-A12.	52
Figure 2-12: Release of the uranium saturated S-layers and synthesis of fresh protein.	53
Figure 3-1: Effect of ²³³ U on the metabolic heat flow of <i>Lysinibacillus sphaericus</i> JG-B53.	59
Figure 3-2: Effect of ²³³ U on the metabolic heat flow of <i>Lysinibacillus sphaericus</i> JG-B53.	61

Table of Figures

Figure 3-3: Effect of ^{233}U on the metabolic heat flow of <i>Lysinibacillus sphaericus</i> NCTC 9602.	62
Figure 3-4: Effect of natural uranium on the metabolic heat flow of <i>Lysinibacillus sphaericus</i> JG-B53.	64
Figure 3-5: Effect of natural uranium on the metabolic heat flow of <i>Lysinibacillus sphaericus</i> NCTC 9602.	65
Figure 3-6: Radiation-induced excluded volume model.	69
Figure 4-1: Copper dependence of the metabolic heat flow of <i>L. lactis</i> in the absence of nisin.	81
Figure 4-2: Copper dependence of the metabolic heat flow of <i>L. lactis</i> in the presence of nisin.	83
Figure 4-3: Uranyl dependence of the metabolic heat flow of <i>L. lactis</i> in the absence of nisin.	84
Figure 4-4: Uranyl dependence of the metabolic heat flow of <i>L. lactis</i> strain in the presence of nisin.	86
Figure 4-5: Comparison of growth rates during first and second phase of logarithmic growth.	87
Figure 4-6: Isothermal titration calorimetry of GSH uranyl complex formation.	89
Figure 4-7: Comparison of biomass production and metabolic heat flow production of <i>L. lactis</i> 3203 strain under the stress of uranyl, and the role of GSH.	90
Figure 5-1: Metabolic heat flow of developing <i>C. elegance</i> under the effect of diferent uranium isotopes with different concentration.	98
Figure 5-2: Life cycle development of <i>C. elegans</i> grown at 22 $^{\circ}\text{C}$ with the related duration of each transformation stage.	99

Abstract

This work was dedicated to quantify and distinguish the radio- and chemitoxic effects of environmentally relevant low doses of uranium on the metabolism of microorganisms and multicellular organisms by a modern and highly sensitive microcalorimetry. In such low-dose regime, lethality is low or absent. Therefore, quantitative assays based on survival curves cannot be employed, particularly for multicellular organisms. Even in the case of microbial growth, where individual cells may be killed by particle radiation, classical toxicity assessments based on colony counting are not only extremely time-consuming but also highly error-prone. Therefore, measuring the metabolic activity of the organism under such kinds of conditions would give an extremely valuable quantitative measure of viability that is based on life cell monitoring, rather than determining lethality at higher doses and extrapolating it to the low dose regime. The basic concept is simple as it relies on the metabolic heat produced by an organism during development, growth or replication as an inevitable byproduct of all biochemical processes. A metabolic effect in this concept is defined as a change in heat production over time in the presence of a stressor, such as a heavy metal. This approach appeared to be particularly versatile for the low dose regime. Thus, the thesis attempted in this case to measure the enthalpy production of a bacterial population as a whole to derive novel toxicity concepts. In the following chapters, an introduction about the properties of ionizing radiation will be briefly presented, in addition to a review about the isothermal calorimetry and its application in studying the bacterial growth. Later in chapter 2, the effect of uranium on the metabolic activity of three different bacterial strains isolated from a uranium mining waste pile together with a reference strain that is genetically related to them will be investigated. Due to the lack of published dedicated calibration techniques for the interpretation of heat production of bacterial cells under the conditions of calorimetric recordings, additional experiments, thorough investigations of the effects of experimental conditions, have been carried out in order to guide the interpretation of calorimetric results. In chapter 3, the differentiation between chemi- and radiotoxicity of uranium has been addressed by isotope exchange, which was a key effort in this thesis as it opens new experimental approaches in radioecology. In chapter 4, through investigating the role of the tripeptide glutathione (GSH) in detoxifying uranium, it will be shown to which degree the intrinsically

Abstract

unspecific signal provided by metabolic heat can be related to highly specific metabolic pathways of an organism, when combined with genetic engineering. The demonstration of gaining molecule-specific information by life metabolic monitoring was another experimental challenge of this thesis and provides proof of principle that can be extended to many organisms. Finally in chapter 5, an attempt has been undertaken to establish a minimal food chain, in order to study the effects of the exposure of a multicellular organism to uranium through its diet.

Chapter 1

1 Introduction

Anthropogenic sources of radiation have increased our exposure to ionizing radiation; as a consequence, the risk of radiation has become a significant societal concern. It is absolutely necessary when discussing the future of man-made sources, like power plants and medical applications to provide hazard assessment and understanding the molecular basis of health risks originating particularly in the more common and potentially long-lasting exposures to low doses. The latter are particularly important for radioecological effects that need to be addressed in studies of environmental radioactivity in the far field of nuclear fuel repositories. In this chapter, an introduction about ionizing radiation and the interaction of microorganisms with uranium and heavy metals in general will be briefly presented. Additionally, a review about the isothermal calorimetry, its application in studying the bacterial growth, and its potential role as tool to be used in assessment of the effects of low doses radiotoxicity will be introduced.

1.1 Basic aspects about ionizing radiation and its interaction with matter

1.1.1 Ionizing radiation

The term “radiation” refers to the emission and the propagation of radiant energy (Webster, 2004). This energy might be in the form of electromagnetic radiation, which has a wide spectrum of energies, or in the form of particles like α , β and neutrons. When radiation interacts with a medium, the atoms will be ionized if the energy of the radiation is high enough, and then this radiation is called “ionizing radiation”. Ionization of an atom by radiation is the process of removing one or more electrons from the atom. On the other hand, if the radiation energy is not sufficient to ionize the atoms of the irradiated medium, then this radiation is called “non-ionizing radiation” as illustrated in Fig. 1-1. This project was meant to assess the effects of low doses of ionizing radiation emitted from uranium isotopes on the metabolic activity of organisms.

Ionizing radiation is classified into “directly ionizing radiation” and “indirectly ionizing radiation”. Directly ionizing radiation includes the charged particles like α and β . When these charged particles pass through the irradiated medium, they ionize the atoms by the columbic force between the particles and the electrons of these atoms. Therefore, charged particles travelling through the medium can directly disrupt its atomic structure along their tracks. Indirectly ionizing radiation, on the other hand, includes neutrons and photons of X-

ray and γ -ray. These kinds of radiation do not possess electrical charge. Here, the ionizations within the medium are due to secondary ionizations caused by liberated electrons (in case of photons) or protons (in case of neutrons) which carry a large fraction of the initially absorbed energy (IAEA, 2010).

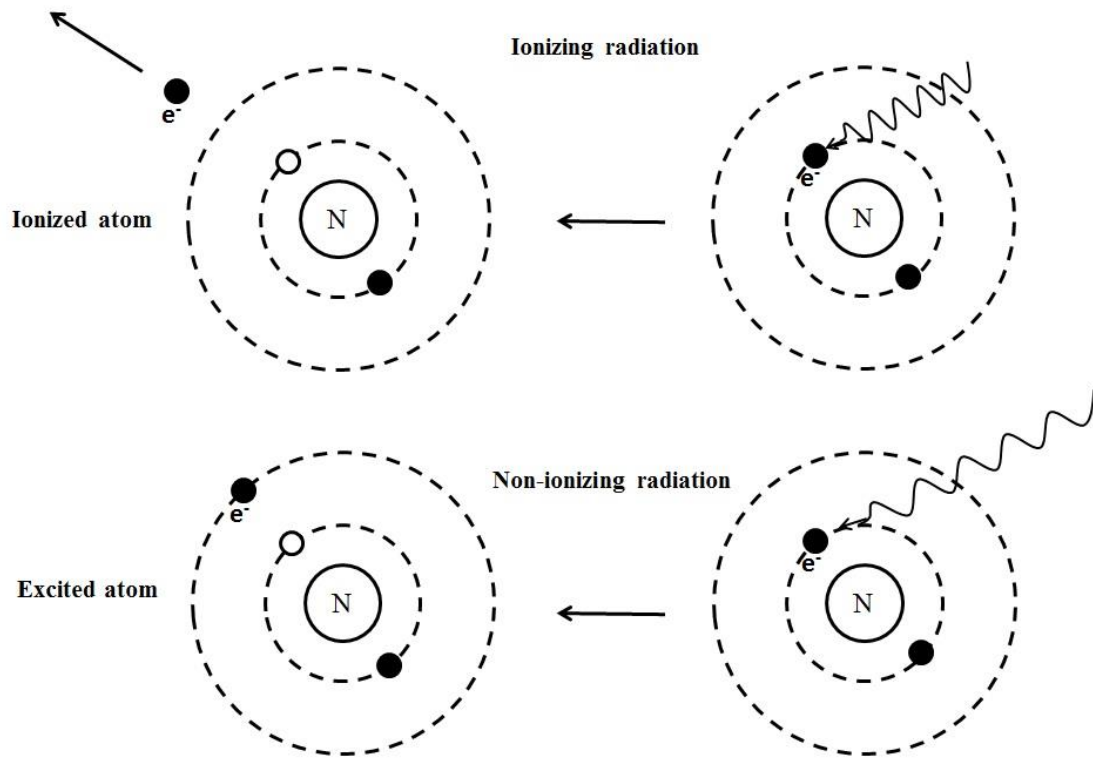


Figure 1-1: Ionizing radiation vs. non-ionizing radiation.

The energy of ionizing radiation is sufficient to remove one or more electron from the atom resulting in negative electrons and positive ion, while the energy of non-ionizing radiation may only excite the atom by transferring one of its orbital electrons to higher-energy-orbital.

The loss of radiation energy within a medium depends on the energy of the radiation, the type of radiation and the density of the medium. The average energy deposited per unit length of radiation track is called Linear Energy Transfer (LET) measured in $\text{keV}/\mu\text{m}$. The energy that charged particles lose along their tracks is greater than the loss related to X- and γ -rays, therefore, charged particles have higher LET than photons. The events of energy transfer to the medium of a low LET radiation along its track are dispersed over larger distances than the dimension of biomolecules like the DNA; a photon might pass through such a molecule without depositing any energy. On the other hand, the events of energy loss of high LET radiation along its track are more closely spaced, and a significant amount of energy will be deposited within the dimensions of typical biomolecules. Furthermore, charged particles deposit their energy at higher densities the slower their speed becomes within the medium. This causes a peak of transferred energy density at the end of the track known as Bragg peak as illustrated in Fig. 1-2 (IAEA, 2010; Knoll, 2010). Accordingly, the biological effects of equal doses of different types of radiation are different.

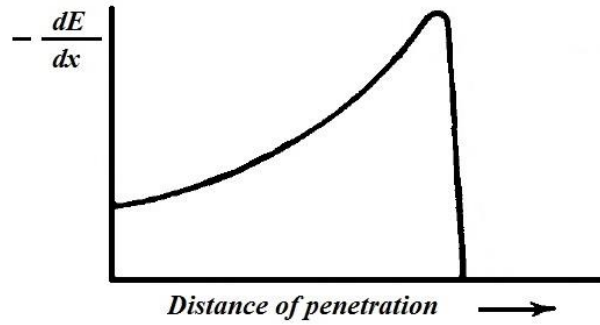


Figure 1-2: The specific energy loss along a charged particle track.

As the charged particle traverse through the medium it loses its energy and become slower, which causes more ionizations per length unit of its track, and therefore they deposit more energy at the end of their track. This figure was adapted from (Knoll, 2010).

1.1.2 Basic definitions

The following definitions were taken from: (Eckerman et al., 2013; IAEA, 2010; Kratz and Lieser, 2013).

- 1- **Radioactivity:** it is the spontaneous emission of radiation by an unstable nucleus.
- 2- **Becquerel (Bq):** it is the SI unit of radioactivity, and it is defined as the decay of one nucleus per second and therefore $1 \text{ Bq} = 1/\text{sec}$.
- 3- **Absorbed dose:** the amount of energy absorbed by the unit mass. It is measured in SI system by J/kg, or gray (Gr). $1 \text{ Gr} = 1 \text{ J/kg}$, and it is given by:

$$D = \frac{dE}{dm} .$$

- 4- **Radiation weighting factor (W_R):** it is a dimensionless factor that is based on the type of radiation.
- 5- **Equivalent dose ($H_{T,R}$):** it is the product of the absorbed dose ($D_{T,R}$) in the tissue T exposed to the radiation R multiplied by the radiation weighting factor W_R :

$H_{T,R} = W_R \cdot D_{T,R}$. It is measured in Sievert (Sv). When different types of radiation exist simultaneously, it is given by the weighted sum over the radiation types:

$$H_T = \sum_R W_R \cdot D_T$$

- 6- **Tissue weighting factor (W_T):** it is a dimensionless factor that is based on the type of tissue or organ that has been exposed to radiation.
- 7- **Effective dose (E):** it is the sum of the weighted equivalent doses in all tissues and organs of the body, it is measured in Sievert, and it is given by:

$$E = \sum_T W_T \cdot H_T$$

8- Relative biological effectiveness (RBE): it is defined as the ratio of doses of γ ray (D_γ) and the dose of any other type of radiation (D_R) that is required to produce the same amount of a particular biological effect, and it is given by:

$$RBE = \frac{D_\gamma}{D_R}$$

For a particular radiation, RBE increases with the LET till it reaches about 100 keV/ μ m, then it declines upon further increase of the LET in mammalian cells. This is called “overkill” effect.

1.1.3 Direct and indirect effects of ionizing radiation

Radiation can affect and ionize biomolecules directly like carbohydrates, DNA, proteins and lipids; this action is called “direct effect of radiation”. On the other hand, water molecules that form about 80 % of living cells might be ionized or excited by the radiation, which will lead to form free radicals which in turn will affect neighboring biomolecules; this effect is called “indirect effect of radiation”. Fig. 1-3 illustrates both effects (IAEA, 2010).

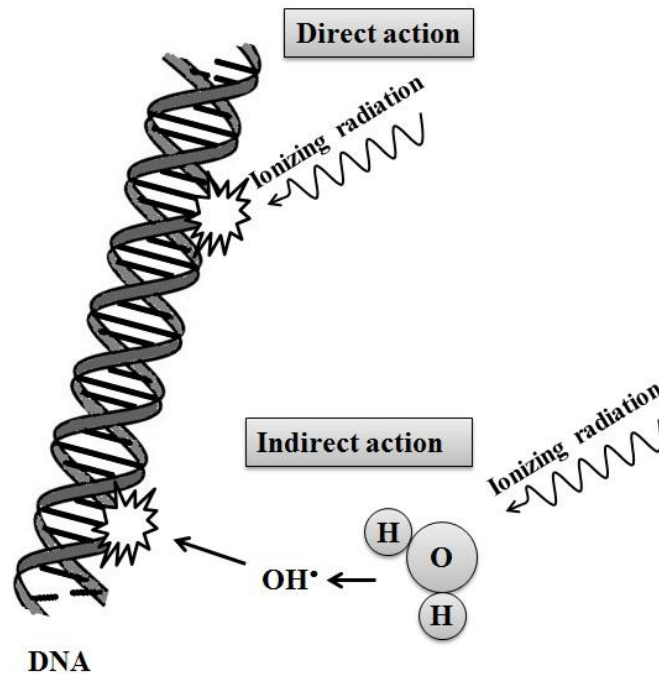
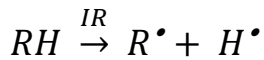


Figure 1-3: Direct and indirect effects of ionizing radiation.

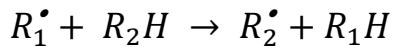
Radiation can directly interact with and affect biomolecules like DNA causing broken bonds and free radicals (direct action), and it can interact with cellular water resulting in water radiolysis and producing free radicals that interact with neighboring biomolecules (indirect action). This figure was adapted from (IAEA, 2010).

1.1.3.1 Direct effects

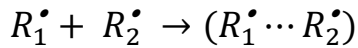
When biomolecules like carbohydrates (RH) are exposed to ionizing radiation (IR), their chemical bonds may break resulting in molecules or atoms with unpaired electrons. Such free radicals are very reactive and have a short life time:



with R^\bullet the radical formed from the biomolecule, and H^\bullet hydrogen free radical. Both radicals can interact with other biomolecules like DNA, proteins and lipids:



The broken bonds might be repaired or radical-radical interactions may lead to cross linking:



The occurrence of direct effects increases with high LET radiation like α -particles (IAEA, 2010).

1.1.3.2 Indirect effects

Since about 80 % of biomass is water, the major portion of radiation energy would be absorbed by cellular water, and therefore the chemical changes in water after being exposed to radiation play an important role in the radiation effects on living cells. These changes are the result of a series of interactions that are illustrated in Fig. 1-4.

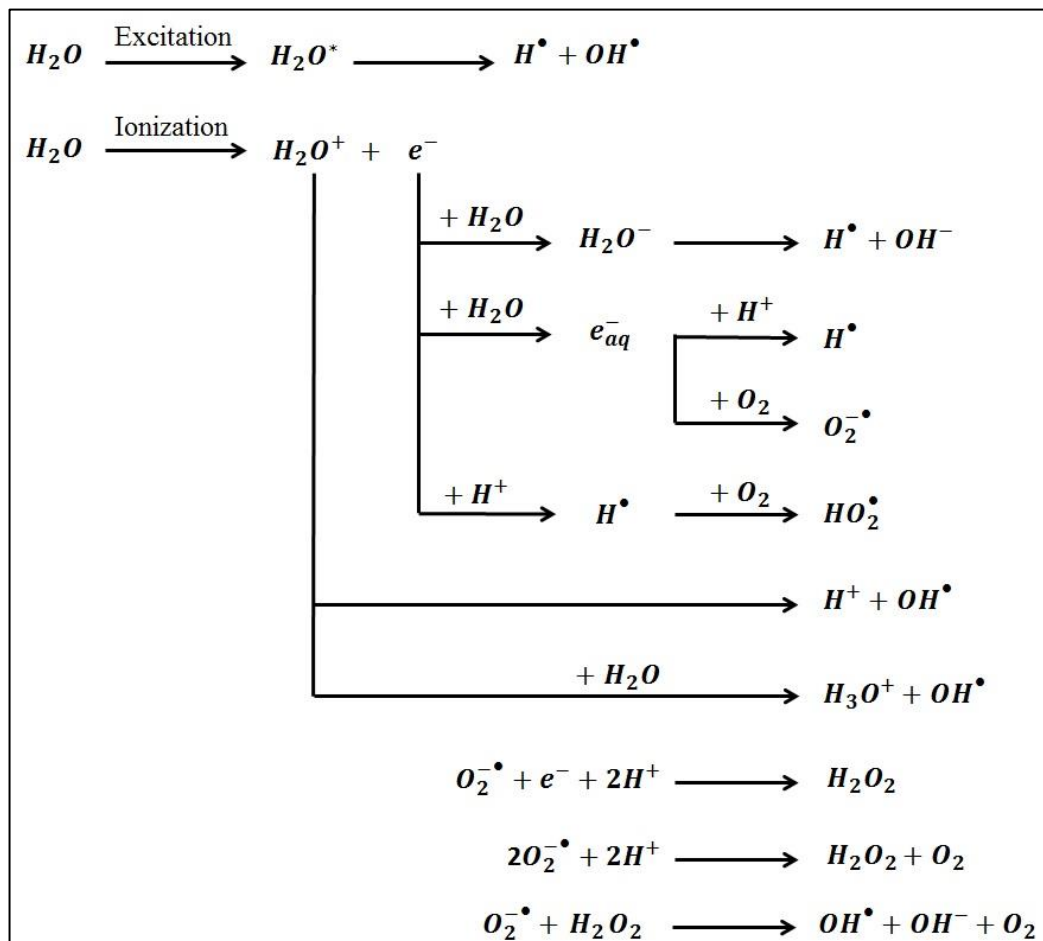


Figure 1-4: Free radicals formation from water radiolysis.

When water molecules are exposed to ionizing radiation a series of interactions will take place within 10^{-13} to 10^{-15} seconds that results in producing free radicals. The information in this figure was adapted from (Alpen, 1998; IAEA, 2010; Cheeseman and Slater, 1993; Riley, 1994).

When water molecules are exposed to radiation they become ionized and excited. Both, water cations H_2O^+ and excited water molecules H_2O^* are unstable and they dissociate to form OH^\bullet and H^\bullet free radicals. The liberated electron from the water molecule after being ionized can interact with water to form hydroxyl ions and hydrogen radicals. They can also interact with hydrogen ions to produce hydrogen radicals which can interact with oxygen and produce hydroperoxyl radicals HO_2^\bullet . They might also lose their energy due to interacting with the medium until they reach the range of thermal energies after about 10^{-11} sec. The thermal electrons interact with the neighboring water molecules dielectrically to form solvated electrons (e_{aq}^-). The solvated electrons interact with hydrogen ions to produce hydrogen radicals. It is possible also that they interact with oxygen to produce superoxide O_2^- which is the precursor of hydrogen peroxide (H_2O_2) (Alpen, 1998; IAEA, 2010).

Among all formed radicals from these interactions, the hydroxyl radical (OH^\bullet) is the most reactive, and therefore, the most hazardous radical that reacts with neighboring biomolecules indiscriminately at a rate close to the diffusion limit (Riley, 1994). Even the significant cellular damage action of superoxide (O_2^-) and hydrogen peroxide (H_2O_2), which are relatively stable, is related to their potential ultimately lead to hydroxyl radical formation as illustrated in Fig. 1-4 and to Fenton reactions (Cheeseman and Slater, 1993; Riley, 1994).

1.1.4 Effects of ionizing radiation on biological molecules

Regardless of the type of ionizing radiation to which biological tissue is exposed, ionized atoms or molecules are generated within the tissue which either return to their parent state or produce free radicals. The conversion of ionized or excited atoms and molecules to free radicals happens in 10^{-13} to 10^{-15} seconds. These free radicals play a central role in radiotoxicity. They interfere with metabolic and redox processes and their high reactivity leads to pathologies and can induce cancer (IAEA, 2010). The radiation-induced persistent chemical alterations of carbohydrates, DNA, protein and lipids further affect the structure and function of biomolecules (Cheeseman and Slater, 1993; Gilbert et al., 1984; Riley, 1994) leading to long lasting disorders. Lipids of cell membranes are more affected by free radicals than proteins and DNA because their unsaturated fatty acids contain particularly reactive carbon double bonds which are the substrate of lipid peroxidation that proceeds in a chain reaction. This chain reaction damages the structure of the cell membrane and produces aldehydes that can damage other parts of the cell (Cheeseman and Slater, 1993). On the other hand, protein and nucleic acids have low possibility to produce these destructive chain reactions when they are affected by free radicals.

The effect of free radicals on proteins leads to functional and structural alterations. This may not be very critical at the cellular level unless this damage accumulates, or the damage concerns a specific functional site which is known as “site specific damage”. DNA is easily affected by free radicals in its vicinity, and a significant damage is considered when strands break or when the damage is not repaired and entails mutations (Cheeseman and Slater, 1993). The flowchart in Fig. 1-5 shows some examples of the effects and consequences of free radicals when they interact with biomolecules.

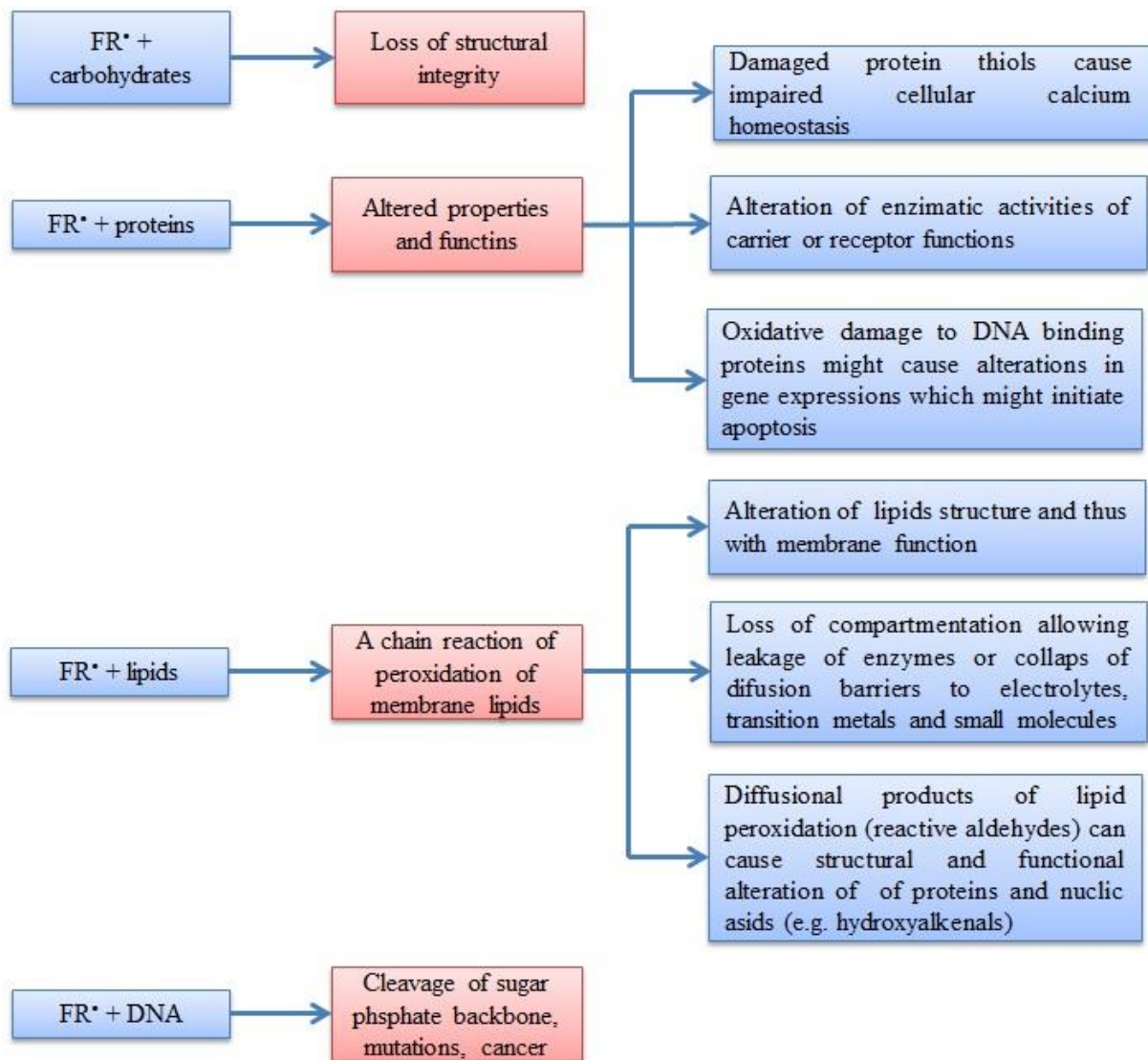


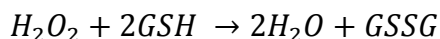
Figure 1-5: Examples of consequences of free radicals interaction with biomolecules.

Free radicals can cause structural and functional alteration to biomolecules leading to long lasting disorders. The information in this figure was adapted from (Gilbert et al., 1984 ; Riley, 1994).

1.1.5 Free radical scavengers

Generally, free radicals are produced in animal cells either accidentally by electron leakage from the electron transfer chain to molecular oxygen generating superoxide, or in a functionally required process when enzymes generate and utilize free radicals in their active sites, such as in ribonucleotide reductase. Therefore, cells have developed defensive mechanisms to prevent free radical-induced cellular damage (Cheeseman and Slater, 1993). There are compounds that can scavenge free radicals, and hydrated electrons can be scavenged by oxygen producing oxygen-centered radicals. A number of thiol-containing compounds like

glutathione (GSH) can scavenge free radicals like hydrogen peroxide as in the following reaction:



where glutathione disulfide (GSSG) is the oxidized state of glutathione. Glutathione has been found to be also involved in heavy metal stress responses. In the context of this work, it was thus of particular interest to study its potential role in uranium detoxification (Chapter 4). Radical scavengers can also donate hydrogen atoms to the radical sites on biological molecules like DNA. However, they mostly react with free radicals generated from water radiolysis, and their availability influences the final degree of radiation damage (Riley, 1994). However, the efficiency of these scavengers is reduced for high LET radiation, where the direct effect of radiation predominates (IAEA, 2010). Likewise, the formation of free radicals by ionizing radiation may exceed the amount of scavengers such that at high doses serious and immediate tissue damage can occur (Cheeseman and Slater, 1993).

1.2 Assessment of chemi- and radiotoxicity of uranium in the low dose regime using metabolic monitoring: Motivations and aims of the study

Radiation and radioactive nuclides have always been a natural part of our environment, and by their existence in soil, water and air they contribute to our exposure to ionizing radiation. Anthropogenic sources of radiation resulting from industry like mining, petroleum industry, nuclear energy, nuclear medicine, consumer products, military, and other industrial applications have increased our exposure to ionizing radiation (Eisenbud and Gesell, 1997a; Eisenbud and Gesell, 1997b). Consequently, the risk of radiation has become a significant societal concern. Hazard assessment and understanding the molecular basis of health risks originating particularly in the more common and potentially long-lasting exposures to low doses emanating from man-made sources, like power plants and medical applications, is absolutely necessary when discussing the future of these applications (Brenner, 2011). The estimation of radiotoxicity has been a field of research since the discovery of biological radiation damage. High doses of ionizing radiation (e.g. ≥ 1 Gy) produce severe health damages including the induction of cancer beside the acute radiation syndromes (Brenner, 2009; Christensen et al., 2014; Donnelly et al., 2010). The effects of low doses (~ 10 mGy) and very low doses (e.g. ≤ 1 mGy), on the other hand, are stochastic and as the dose decreases, the probability of cancer induction might decrease (Brenner, 2009; Brenner, 2011; Christensen et al., 2014). Therefore, the assessment of low dose radiotoxicity requires monitoring of a very large low-dose-exposed population along their lifetime in order to detect a significant increase in cancer development. Unfortunately, this measurement is very difficult to be accomplished if not impossible (Brenner, 2011; Brenner et al., 2003). About 40% of the studied human populations develop cancer at some point of their lives (Brenner, 2009), and it is not possible to distinguish between cancers according to their molecular causes. Furthermore, the number of cancers related to low doses of radiation would always be lower than the natural background of cancer (Brenner, 2009; Brenner and Sachs, 2006). Thus, uncertainties will always greatly affect the estimation of low doses radiotoxicity (Brenner, 2009). To solve this problem, some scientists extrapolated the risks of cancer induction at low doses and very low doses from intermediate doses using the linear no-threshold model (LNT) (Brenner et al., 2003; Brenner and Sachs, 2006). The use of this

method is controversial and it was found to overestimate the risk at low and very low doses (Brenner, 2009; Tubiana, 2005; Tubiana et al., 2006). Consequently, the reliance on monitoring the exposed population to low doses of radiation would not be sufficient alone. However, studying the biological effects of low doses of ionizing radiation at the cellular and subcellular level may provide valuable information on molecular mechanisms of low dose radiotoxicity and estimate the chance for long-term damages (Brenner, 2011). Thus, developing new experimental approaches to study biological responses to radiation at the cellular and subcellular level is of prominent importance to quantify radiotoxicity and to ultimately identify defense mechanisms against low doses of radiation.

The present work focuses on the detection of biological responses on the cellular and subcellular level by measuring the reaction enthalpy of all biochemical processes occurring in a population of cells or in a multicellular organism. Such an approach is entirely independent of previous knowledge of specific metabolic processes, and could thus provide a novel and versatile method in radioecological studies. Here, an assessment of radioecological adaptation or radiotoxicity needs to be accomplished with a selection of the given *in situ* organisms rather than with genetically and metabolically fully described model organisms. Bacteria are of prominent interest because they exhibit high adaptability to the most diverse environmental stress. Their study may lead to the identification of defense mechanisms against radionuclides which may open routes for their use in bioremediation. For example, bacteria have been isolated from uranium mining waste piles (Selenska-Pobell, 2002), and these microorganisms can interact with uranium and other radionuclides as well as heavy metals without suffering in their viability. On the other hand, through this interactions, bacteria can influence the mobility and bioavailability of uranium in the environment (Lloyd and Macaskie, 2002a; Selenska-Pobell, 2002) such that microbial metabolism can play an important role in the environmental spread of radionuclides. According to Jon R. Lloyd and Lyme E. Macaskie (Lloyd and Macaskie, 2002b) these interactions occur by different mechanisms as illustrated in Fig. 1-6, and they are classified as following:

- a) Biosorption: Adsorption of a heavy metal to the surface of dead or life cells independently of metabolism.
- b) Bioaccumulation: Metabolism-dependent uptake of a heavy metal by the cell.
- c) Biotransformation: Transformation of a heavy metal into less soluble or more volatile compounds by means of bioreduction and biothylation respectively.
- d) Biomeneralization: Precipitation of heavy metals by ligands of biogenic origin, such as phosphate, sulfide and carbonate.
- e) Microbe-enhanced chemisorption of heavy metals: Microbial cells deposit one metal to be used as a host to deposit further targeted metal chemically.

Several studies showed that U(VI) binds to the negatively charged hydroxyl, carboxyl and phosphate groups of the cell surface via biosorption (Merroun et al., 2005; Merroun and Selenska-Pobell, 2008; Pollmann et al., 2005; Reitz et al., 2014). The existence of microorganisms in an environment polluted by heavy metals or radionuclides is a prime motivation to study the metabolic response of microorganisms to these pollutants and raises the following questions:

- Are the bacterial strains that exist in a uranium waste pile adapted to uranium toxicity, and how would low doses of uranium affect the metabolic activity of these strains?
- Is it possible to differentiate radiotoxicity from chemitoxicity of uranium?
- Is it possible to identify molecular mechanisms that mediate the detoxification of radionuclides?
- How are radionuclides transferred to the food chain?

Each of the questions will be addressed in a separate chapter after some general considerations of bacterial growth and its relation to metabolic heat release. Chapter 2 provides a general description of the effects of different concentrations of uranium on the metabolic activity of bacterial strains from a uranium mining waste pile, while chapters 3 and 4 address the more specific questions.

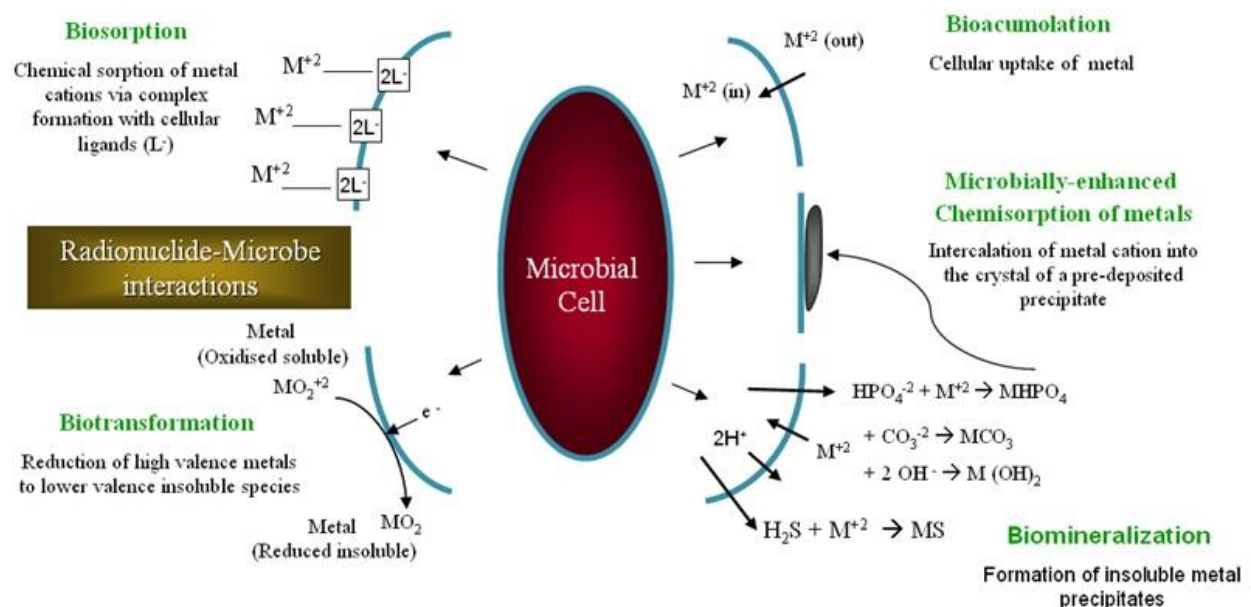


Figure 1-6: Mechanisms of radionuclide–microbe interactions.

This figure was adapted from (Lloyd and Macaskie, 2002).

According to Bricheux *et al.*, Forrest was the first who demonstrated in 1961 that the heat released by a growing bacterial culture scales with the increment of the biomass (Bricheux *et al.*, 2013; Forrest, 1961). Additionally, due to its relative ease and wide applicability, it is expected that an isothermal microcalorimeter would be a perfect instrument to address these radioecological questions. In this respect, the experiments represent pilot studies that allow introducing this entirely model-free experimental approach into quantitative radioecological research. On the other hand, the selected organisms cover both, microbial isolates that are of direct radioecological relevance since they have been isolated from uranium mining sites, as well as reference organisms and genetically engineered bacteria which allow relating the results to specific adaptational or molecular processes, respectively. However, in order to achieve this goal, basic knowledge about the growing behavior of

bacterial cultures and how to monitor their metabolic activity by isothermal microcalorimeter is necessary.

1.3 Investigating Bacterial growth by isothermal microcalorimetry

1.3.1 Bacterial growth

In general, bacterial growth refers to both increase of cell size and increase of cell number. Only the latter will be discussed here. Assuming a volume of nutrient medium that contains at time ($t = 0$) a number of bacterial cells N_0 . Then, after a certain time called the doubling (or generation) time ($t = d$) each cell will have divided into two new cells, and then the number of cells will be:

$$N = N_0 \cdot 2 \quad (\text{Eq. 1-1})$$

After time (t) the number of divisions will be (n) then:

$$N = N_0 \cdot 2^n \quad (\text{Eq. 1-2})$$

But $n = t / d$. Therefore:

$$N = N_0 \cdot 2^{\left(\frac{t}{d}\right)} \quad (\text{Eq. 1-3})$$

According to the properties of natural logarithm: ($2 = e^{\ln(2)}$). Then we can rewrite equation 1-3 as following:

$$N = N_0 \cdot e^{\left(\frac{\ln(2) \cdot t}{d}\right)} \quad (\text{Eq. 1-4})$$

By defining: ($k = \ln(2) / d$), then:

$$N = N_0 \cdot e^{k \cdot t} \quad (\text{Eq. 1-5})$$

The variable (k) represents the growth rate, which is constant and specific for a given bacterial strain. This equation describes the exponential growth phase of bacterial cultures. In ideal conditions where the nutrient is unlimited and by-products of the growth are removed, then the bacterial growth described by equation 1-5 would last forever. Under the conditions of the microcalorimetric experiments, bacteria are grown in a batch culture, which is a closed system with specific amount of nutrients and air. Therefore, when nutrients are not added to the culture, nor the by-products are removed during incubation, then the growth rate will change according to the status of the nutrients and toxins and all other potential changes in the medium. Thus, the bacterial batch cultures can follow the exponential growth model only for a limited time of the culture's life. The changes of the growth rate characterize successive phases of bacterial growth as illustrated in Fig. 1-7 (Monod, 1949).

These phases were well classified by Martin Forbisher (Forbisher, 1965) as following:

1. Lag phase: During this phase the non-dividing bacterial cells start to adapt to their new environment.
2. Acceleration phase: Growth rate increases.
3. Exponential phase: Growth rate is constant. The bacterial growth in this phase is described by Eq. 1-5.
4. Deceleration phase: Growth rate drops down due to insufficiency of nutrients and accumulation of by-products.
5. Stationary phase: the number of dead cells is in equilibrium with the rate of increase thus, the total population stays unchanged and the overall growth rate is zero.

6. Decline phase: During this phase bacterial cells die or become “dormant” by formation of non-metabolizing states, such as spores. The growth rate is negative.

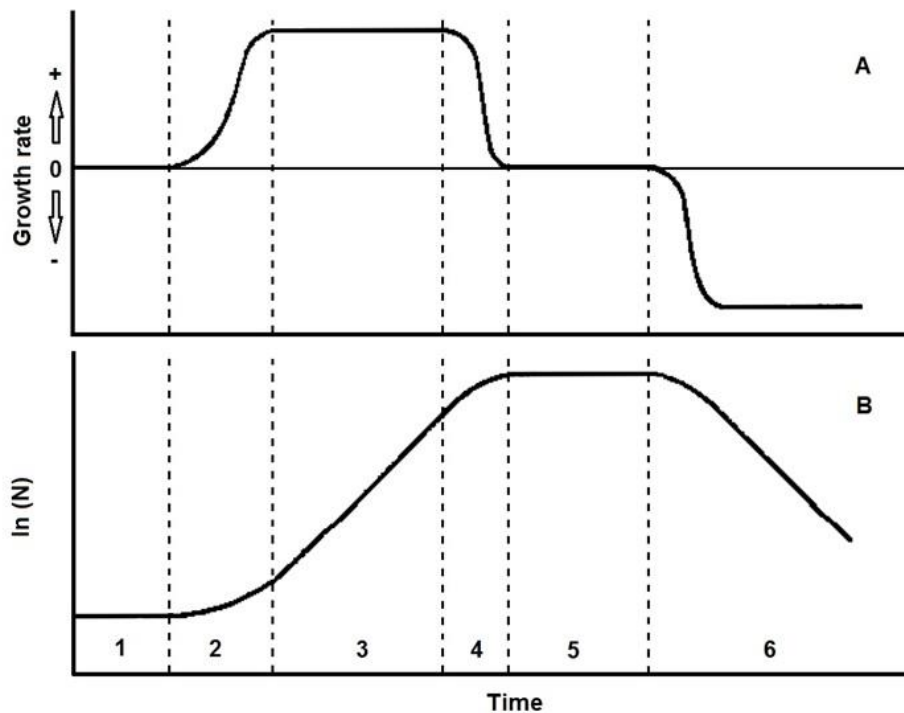


Figure 1-7: Phases of bacterial growth.

A: variation of growth rate. B: Natural logarithm of the number of bacteria vs. time. This curve shows the different phases of bacterial growth as following: 1- lag phase, 2- acceleration phase, 3- exponential phase, 4- deceleration phase, 5- stationary phase and 6- decline phase. This figure was adapted from (Monod, 1949).

1.3.2 Isothermal microcalorimetry

All metabolic reactions of living cells produce heat (Wadso, 1995; Xie et al., 1988). Monitoring the released metabolic heat allows investigating bacterial growth under different conditions. The measurement of the heat released or absorbed by a system is called “calorimetry”, and the instrument that performs this measurement is called “calorimeter”. The isothermal microcalorimeter (IMC) is an instrument that measures the heat flow from or to a sample, with sensitivity in the range of 1 μ W or less, at constant temperature (Wadso, 1995; Wadso, 2002).

Most of the IMCs used in these days to measure living systems are of the heat conduction type (called also heat flow type) (Wadso, 1997; Wadso, 2002). These calorimeters are designed as twin instruments that possess two vessels: a sample vessel and a reference vessel, as illustrated in Fig. 1-8. A heat detector separates the vessels from the isothermal heat sink. This detector consists of several “thermocouples” that are connected to each other in series, forming “thermopile” (Fig. 1-9).

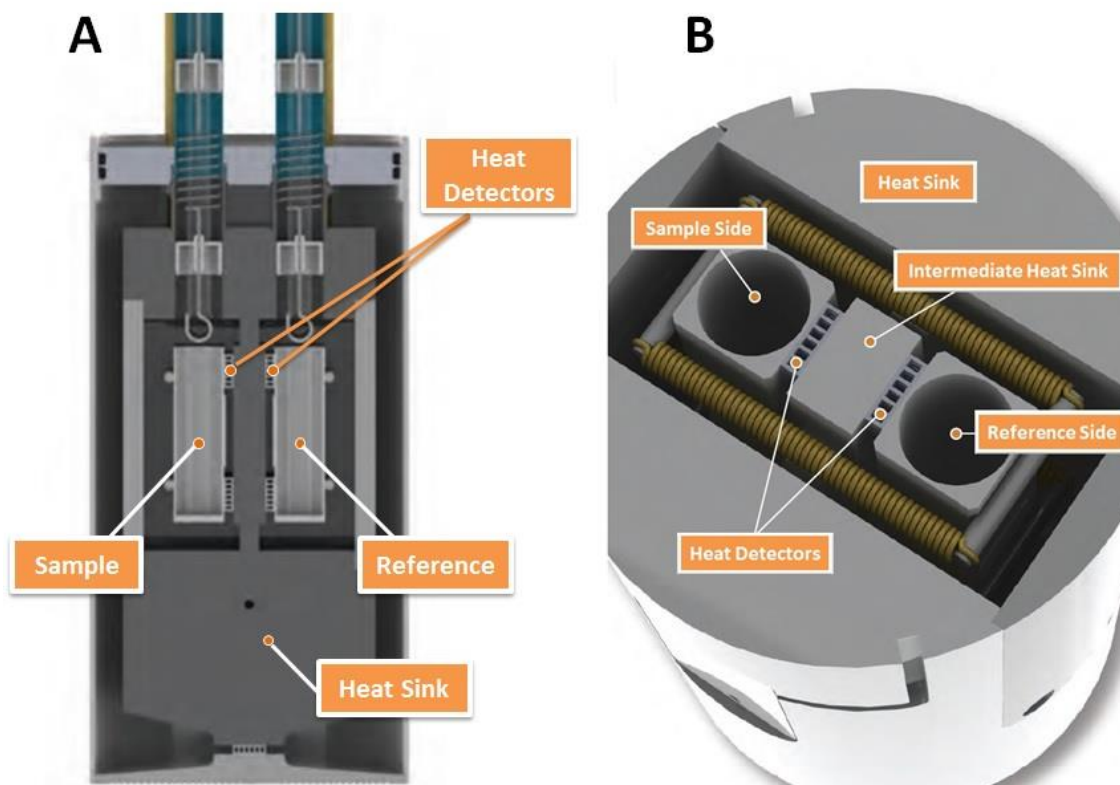


Figure 1-8: Isothermal microcalorimeter.

This figure shows the place of sample and reference positions together with the thermal detector and the heat sink in A: Longitudinal section. B: Cross section. This figure was adapted from (TA Instruments microcalorimeter brochure, 2012).

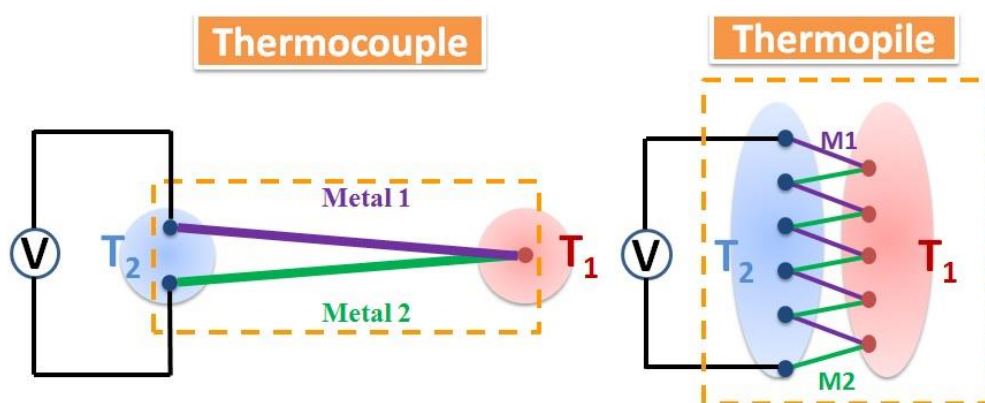


Figure 1-9: The thermocouple and the thermopile.

The thermocouple is a device that converts the differences of temperature between the ends of two connected different metals directly into electricity as illustrated. This conversion process is named Seebeck effect after the German physicist Thomas Johann Seebeck who discovered it. This figure was adapted from:

<http://physics.stackexchange.com/questions/17756/understanding-the-seebeck-effect>

The thermocouple is a device that measures the temperature differences by converting thermal energy into electrical energy by means of the Seebeck effect as illustrated in Fig 1-9. When the heat is released from the sample vessel, a difference in the temperature between the sample and the heat sink will occur, this will create a voltage in the thermopile in accordance with the Seebeck effect. This voltage is proportional to the difference in temperature between the sample and the heat sink, and thus it would be proportional to the heat release per time unit “heat flow”² produced or consumed by the sample. The output that comes from the IMCs is the continuously measured difference in the heat flow between the sample and the reference (Wadso, 1997; Wadso, 2002; Wadso and Goldberg, 2001). The heat flow vs. time plot is called “thermogram”.

Studying bacterial growth by IMC showed that thermograms exhibit a general pattern that corresponds to the aforementioned three distinctive phases of bacterial growth: a lag phase followed by exponential growth that consists of one or more phases and which ends with a maximal heat flow before the signal declines to the base line level or a low stable production. The latter indicates that the nutrients have been exhausted in the vicinity of the typically sedimented bacterial population (Braissant et al., 2013; Bricheux et al., 2013). The calorimetrically recorded growth phase correlates well with those measured in a conventional way (typically by turbidity) (Holzel et al., 1994; Xie et al., 1988).

Assuming that the heat flow released by each bacterial cell (m) during the exponential phase is constant, the time-dependent heat flow produced by the culture is:

$$P(t) = m \cdot N(t) = m \cdot N_0 \cdot e^{k \cdot t} = P_0 \cdot e^{k \cdot t} \quad (\text{Eq. 1-6})$$

with $P_0 = m \cdot N_0$. The accumulated heat over time is the integrated heat flow:

$$Q(t) = \int_0^t P(t) \cdot dt = \left[\frac{1}{k} \cdot P_0 \cdot e^{k \cdot t} \right]_0^t = \frac{P_0}{k} (e^{k \cdot t} - 1) = \frac{1}{k} \cdot P - \frac{P_0}{k} \quad (\text{Eq. 1-7})$$

then it can be rewritten as:

$$P = k \cdot Q + P_0 \quad (\text{Eq. 1-8})$$

Equations 1-6 and 1-7 are the simplest models that describe the exponential bacterial growth phase, and there are other more complicated models that have been used by some of the groups in this field (Braissant et al., 2013). It is very complicated and difficult to generate a full mathematical description for an entire thermogram. Therefore, the analysis of the thermograms presented here is mostly restricted to the exponential phase, where no additional assumptions on complex growth behavior are made. Likewise, the maximal heat flow reached after the exponential phase will be shown to be useful in assessing toxicities. Consequently, three parameters have been extracted from the thermograms for further analysis: the maximal heat flow (P_{\max}), its time coordinate (T_{\max}) and the growth rate (k) of the exponential phase. The values of P_{\max} and T_{\max} can be obtained directly from the raw data in the thermograms. On the other hand, the values of the growth rates have been determined by plotting the heat flow vs. heat. In these plots the exponential phase corresponds to a linear dependence as shown in Eq. 1-8. The slopes of linear fits of these parts of the plots are the growth rates. Using this approach to define the growth rates, there is no need of defining the lag phase and

² Also it might be found under other names like “power”, “thermal power” and “heat rate” and the latest is the most accurate when it comes to physics, but the working groups in the field of calorimetry mostly use the term “heat flow”.

it ease finding the correct portion of the curve to be fitted, unlike the case relating the other two models of equations 1-6 and 1-7.

1.4 The use of isothermal microcalorimeter to study inhibitory actions on living cells

When monitoring the metabolic activity of microorganisms, calorimeters measure the net summation of the heat, whether released or absorbed, by the overall processes that take place in the metabolism, without being able to specify each one of these interactions. This renders calorimetry non-specific but at the same time extremely versatile for the detection and quantification of otherwise non-identifiable metabolic effects in a living organism under well-controlled conditions (Johansson and Wadso, 1999; Wadso, 1995).

Calorimeters in general have been used as an analytical tool in a wide range of sciences. It has been used in soil and environmental science (Kimura and Takahashi, 1985; Rong et al., 2007; Wadso, 2009), in food science (Alklint et al., 2005; Stulova et al., 2011; Wadso and Galindo, 2009), in Pharmaceutical science (Braissant et al., 2010a; Buckton, 1995; Howell et al., 2012; Vemuri et al., 2004), in the medical field (Baldoni et al., 2009; Monti, 1990), to study tumor tissues (Karnebogen et al., 1993), it was used in diagnosis (Trampuz et al., 2007), in determination of allergic drug reactions (Murigande et al., 2009), determining the effects of antibiotics on microorganisms (von Ah et al., 2009), in finding adequate antimicrobial in relatively short time (Braissant et al., 2014) and many other fields (Kemp and Lamprecht, 2000; Wadso, 1985; Wadso, 1995). Through these different fields the metabolic activity of different kinds of living systems has been measured like: fungi (Wadso et al., 2004), yeasts (Schuler et al., 2012; Sivaprakasam et al., 2011), bacteria (Braissant et al., 2010b; Xie et al., 1988), plant tissue and plant cells (Criddle et al., 1988; Sivaprakasam et al., 2011; Wadso et al., 2004), animal cells (Guan et al., 1999; Kemp, 1991; Kemp and Guan, 2000), human cells (Barbero et al., 2005; Monti et al., 1980; Santoro et al., 2011), nematodes (Braeckman et al., 2002), fishes, frogs, lizards and other small animals (Regan et al., 2013; Wadso, 1997) and even humans (Dauncey et al., 1978). Although the IMC has been used in diverse commercial or medical applications, its routine use in science would be the investigation of the inhibitory action of a substance on the growth of microorganisms. During the last 30 years the IMC was found to be a powerful instrument to study the growth of microorganisms. The microcalorimetric measurements allow expressing the microbial growth behavior much more accurately and quantitatively than it would be possible by conventional turbidity-based methods, which have a much lower signal to noise ratio and are prone to optical artifacts related to cell shape and colony formation. Efforts have been spent to set up models of microbial growth in the IMC (Braissant et al., 2013). These models provided a frame work to use the IMC for toxicity assessment and investigating inhibitory actions on microbial growth of some compounds like pesticides (Prado and Airoidi, 2000) and herbicides (Bricheux et al., 2013) and antibacterial viability (Garedew et al., 2004; Lin et al., 2011; Xu et al., 2014), and a recent work has also studied the effect of gamma rays (Wirkner et al., 2002). Several groups have improved in this field, and each one has used its own method to assess the inhibitory action of particular conditions on microbial growth by the IMC. Some of these groups used the universal inhibitory ratio of the growth rate (Lin et al., 2011; Xu et al., 2014; Yang et al., 2008; Zhang et al., 2012; Zhao et al., 2014), which is very

simple to derive by comparing the growth rate under inhibiting or promoting conditions in relation to reference conditions:

$$I_K = \left(\frac{K_{(0)} - K_{(i)}}{K_{(0)}} \right) \times 100 \% \quad (\text{Eq. 1-9})$$

with k_0 and k_i the growth rate constants under the reference conditions and inhibiting or promoting conditions, respectively. Another model has been proposed to describe the deceleration / acceleration of growth caused by growth inhibitors or enhancing factors in comparison to reference conditions (Honglin et al., 1995):

$$\frac{dN(t)}{dt} = \mu \cdot N(t) - \beta \cdot N(t)^2 \quad (\text{Eq. 1-10})$$

with $N(t)$ the number of cells at time t , μ : growth rate constant and β a factor that accounts for the effect of inhibitors or promoters on the growth rate. However, this model did not give a satisfying quantitative description of toxicity. According to the best of our knowledge, Katsutada Takahashi, who started in 1990 to assess drug actions on living cells by calorimetry (Takahashi, 1990), was the first to relate the metabolic heat measurement to the toxicological terms “bactericidal” (the effect of a substance that kills the bacteria) and “bacteriostatic” (the effect of a substance that prevents reproduction of the bacteria) (Takahashi, 2000). Shortly after that, he developed a quantitative measurement of the of bactericidal action of a drug based on the concentration dependence of the drug effects (Wirkner and Takahashi, 2000). Although this seminal work in the field the IMC is greatly appreciated, some conclusions about the calorimetric signatures of the bactericidal and bacteriostatic actions still ambiguous as will be discussed in the following chapter. Moreover, his model is not applicable for low dose of inhibitory actions, when cells activate defense mechanisms to adapt to environmental stress.

In the realm of this work, the determination of the inhibitory ratios (I) that compare the three growth parameters, P_{\max} , T_{\max} and k is found to be the best way to assess toxicity by the IMC. Unlike other groups who used I_k , and ignored those of P_{\max} and T_{\max} , it became clear during this thesis that valuable information is gained from the combination of all these characteristic numbers.

Chapter 2

2 Influence of low concentrations of natural uranium on different bacterial strains isolated from a uranium mining waste pile

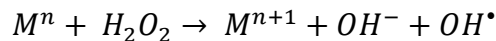
2.1 Abstract

In this study, the toxicity of natural uranium in the bacterial strains of *Lysinibacillus sphaericus* JG-A12, JG-B53 and *Paenibacillus* JG-TB8, previously isolated from a uranium mining waste pile at Johann-Georgenstadt, Saxony, Germany, (Selenska-Pobell, 2002) was quantified by deriving the growth parameters from the metabolic heat measurements of their culture growth under different concentrations of natural uranium. Additionally, similar experiments were performed with the strain *Lysinibacillus sphaericus* NCTC 9602 which is genetically closely related to the strains JG-A12 and JG-B53 and, therefore, was used as a reference. The metabolic activity of these strains was monitored during their growth in an isothermal microcalorimeter (IMC) by recording the metabolically released heat flow of the bacterial cells under the stress of low concentrations (0-150 μM) of uranyl nitrate. The objective of this work is to quantify the toxicity of a radionuclide and to define it as a measurable effect on the metabolic activity under low environmentally relevant doses, rather than using existing assays which are based on lethality that is absent under such low doses. The results showed that all four strains reacted to the presence of uranium. Strain JG-TB8 was the most sensitive followed by JG-B53, JG-A12 and, unexpectedly, NCTC 9602 was the least sensitive strain to uranium in terms of changes in metabolic heat production.

2.2 Introduction

Uranium is an abundant natural element that is widespread in the environment, exhibiting average concentrations of 1-5 mg/kg in the earth's crust (25.4 to 127 Bq/kg) and 0.1-5 $\mu\text{g/l}$ in water (0.00254 to 0,127 Bq/l) (Handley-Sidhu et al., 2010; Parrish et al., 2008). Consequently, uranium is found in our food and drink water, and the average daily intake is between 1.0 and 1.4 $\mu\text{g/day}$. Thus, the general population is exposed through food and water

to chronically low doses of uranium (Llobet et al., 1991; Paternain et al., 1989). Chemically, it can be found in four different oxidation states U(III), U(IV), U(V) and U(VI), but it is commonly found in nature and in the mammalian body as U(VI) in the form of uranyl ion (UO_2^{2+}), which is the most stable and most soluble species (Domingo, 2001; Harvey et al., 1986). Industrial and military use of uranium in nuclear power plants, nuclear weapons, ammunition as well as armors made of depleted uranium (Domingo, 2001) represent additional anthropogenic source of uranium in the environment. Natural uranium contains 99.3 % ^{238}U , 0.7 % ^{235}U and about 0.005 % ^{234}U (Domingo, 2001; Handley-Sidhu et al., 2010), and has a specific activity 25400 Bq/g (Li et al., 2009). The hazardous risk of uranium is due to both: its interference with metabolism similarly to other heavy metals, and to its alpha particle emission, rendering it a radiobiological toxin when it is introduced to the body through inhalation, ingestion or through a contaminated wound (Christensen et al., 2014). Alpha particles can cause DNA damage either by direct ionization or indirectly by water radiolysis leading to reactive oxygen species (ROS) as discussed in chapter 1. On the other hand, uranium also possesses considerable chemical toxicity represented, for example, by its ability to interact with hydrogen peroxide (H_2O_2) to form hydroxyl radicals (OH^\bullet) in a Fenton's reaction (Miller et al., 2002):



where M and n refer to the “metal” and its cationic charge, respectively.

It is thus an interesting question how we can differentiate between radio- and chemitoxicity, and to what extent general heavy metal detoxification mechanisms that have evolved to prevent oxidative stress may also attenuate uranyl toxicity. These questions will be addressed in more detail in chapters 3 and 4 respectively. Here, the focus is on the quantitative assessment of toxicity of low doses of uranium by a rather new technique in the field of radioecology.

Interestingly, bacteria are present also in heavily polluted uranium mining waste piles (Selenska-Pobell, 2002). The experiments performed here were motivated by the question how these bacterial strains are affected by uranium and whether they have adapted to this environment. Large numbers of *Bacillus* strains were previously isolated from a uranium mining waste pile in Saxony, Germany (Lederer et al., 2013; Reitz, 2011; Selenska-Pobell et al., 1999), where the concentrations of uranium in this site varied between 18 and 178 mg/kg in the soil (between 457.2 and 4521.2 Bq/kg), and up to 5 mg/l in water samples (that is equivalent to a concentration of 21 μM and to ~ 126 Bq/l) (Selenska-Pobell, 2002). Three of these isolated strains, *Lysinibacillus sphaericus* JG-A12, *Lysinibacillus sphaericus* JG-B53

and *Paenibacillus* JG-TB8 were used in this project as model organisms to study the effect of low doses of radiotoxicity exerted by uranium on the bacterial metabolic activity. Additionally, the strain *Lysinibacillus sphaericus* NCTC 9602 was purchased from the national collection of type cultures, London, UK (Pollmann et al., 2005), and was used in this study as a reference for the two strains JG-A12 and JG-B53 (Lederer et al., 2013; Selenska-Pobell et al., 1999).

When a cell is exposed to radiation any of its molecular constituents might get affected. Therefore, in order to monitor the effects on the metabolic activity of the irradiated cells, the used method should be “unspecific” such that it can be used without prior molecular knowledge. This renders the isothermal microcalorimetry a perfect method for this study (Wadso, 1995; Wadso, 1997). Wirkner *et al.* were the first to use the isothermal microcalorimeter (IMC) to study the effect of radiotoxicity of γ -rays on bacterial growth (Wirkner et al., 2001; Wirkner et al., 2002). They irradiated bacterial cells with high γ -ray doses up to 10 kGy using a ^{60}Co source before culturing them in the IMC to thermally monitor the influence of radiotoxicity on their metabolic activity and growth development. They showed the inadequacy of the colony counting method to evaluate the sterility of irradiated samples as this method does not provide information about the bacteriostatic action of the irradiation in the microbial cells.

The aim of this work is to assess the effect of low doses of radiotoxicity on microorganisms by monitoring their metabolic activity by IMC, and to derive quantitative parameters that can be used to define toxicity qualitatively and quantitatively. Four different bacterial strains were investigated; three isolated bacterial strains and the reference strain were cultivated with different concentrations of natural uranium in the IMC. The obtained thermograms (heat flow vs. time curves) reflect the changes of the metabolism of the samples and were used to quantify uranyl sensitivity. The study covered the concentration range 0.1 to 150 μM . Inhibitory ratios were derived from the thermograms using the parameters, (T_{max}), (P_{max}) and (k) (see section 2.3.2). The objective in this approach is to find the strain that is less affected by the toxicity of uranium nitrate.

2.3 Materials and Methods

2.3.1 Bacterial culture and isothermal calorimetry

The bacterial strains *Lysinibacillus sphaericus* JG-A12, *Lysinibacillus sphaericus* JG-B53, *Paenibacillus* JG-TB8 and *Lysinibacillus sphaericus* NCTC 9602 were exposed to

different concentrations of natural uranium (U_{nat}) in the form of $UO_2(NO_3)_2$ within liquid cultures. Bacterial cultures were grown in 50% R2A medium containing, per liter, 0.25 g yeast extract, 0.25 g peptone, 0.25 g casamino acids, 0.25 g glucose, 0.25 g soluble starch, 0.15 g sodium pyruvate, 0.15 g K_2HPO_4 , and 0.025 g $MgSO_4 \times 7H_2O$. The mixture was autoclaved at 120 °C for 20 min. The bacterial strains were freshly precultured from a frozen glycerol stock before each experiment by growing them overnight in 50% R2A at 30 °C. For microcalorimetry experiments, autoclaved glass ampoules were filled with 1990 μl medium supplemented, as required, with $UO_2(NO_3)_2$ to final concentrations of 0 – 150 μM . The samples were inoculated with 10 μL of the appropriate bacterial culture, adjusted to an optical density (OD_{600}) of 0.1, resulting in an initial OD_{600} of 0.0005 at the start of microcalorimetric measurements in 2 ml final volume of the samples. In each experiment the samples were prepared in duplicates. Two blank samples that contained only medium were run in order to check the sterility of the medium and two samples that contained only medium with bacteria without any uranium were run as a control. Finally, the ampoules were sealed tightly and introduced into the calorimeter in two steps: first the samples were lowered to the equilibration position, where they were kept for 15 min, after that they were further lowered to the measuring position, at that point the instrument takes additional 45 min for thermal stabilization before it starts acquiring real time data. Isothermal microcalorimetry was performed with the multi-channel IMC TAM III instrument (Waters GmbH, Eschborn, Germany) equipped with 12 identical minicalorimeters, to monitor in real time the metabolic heat produced by the bacterial cultures at 30 °C. In order to monitor a dose response, a wide range of $UO_2(NO_3)_2$ concentrations was covered for each of the bacterial strains, i.e., 0.1 – 1.5 μM , 2.22 – 13.35 μM and 10 – 150 μM . Additionally, equivalent experiments were performed with $Mg(NO_3)_2$ as a reference to evaluate the possible effect of the nitrate present in $UO_2(NO_3)_2$ on the growth of the strains.

2.3.2 Data analysis

The software of the TAM III “TAM AssistantTM” records the real time changes of the heat flow of the samples and plots them in the form of heat flow vs. time curves called thermograms. As mentioned in section 1.3.2, thermograms of bacterial growth have a general pattern with three distinctive phases, and the analysis of the thermograms was restricted to the exponential phase and the following peak heat flow. The maximal heat flow (P_{max}) and the time coordinate of the maximal heat flow (T_{max}) were extracted from the thermograms. The

integration of the heat flow gives the total released heat as a function of time as provided by the software. By plotting the heat flow vs. heat, the growth rate constant (k) was determined by linear regression as described in section 1.3.2.

The addition of uranium to the bacteria affected their metabolic activity, as it is evident, for example, from the change of T_{\max} values in comparison to those of the controls (0 μM uranium). Therefore, inhibitory ratios (I) which compare the three determined growth parameters under different concentrations of uranium with those of the controls were calculated as follows:

$$I_p = \left(\frac{P_{\max(i)} - P_{\max(0)}}{P_{\max(0)}} \right) \times 100 \% \quad (\text{Eq. 2-1})$$

$$I_T = \left(\frac{T_{\max(i)} - T_{\max(0)}}{T_{\max(0)}} \right) \times 100 \% \quad (\text{Eq. 2-2})$$

$$I_K = \left(\frac{K_{(i)} - K_{(0)}}{K_{(0)}} \right) \times 100 \% \quad (\text{Eq. 2-3})$$

Where: $P_{\max(i)}$ is the maximal heat flow at the i^{th} uranium concentration. $P_{\max(0)}$ is the maximal heat flow in the absence of uranium. $T_{\max(i)}$ is the time of maximal heat flow at the i^{th} uranium concentration. $T_{\max(0)}$ is the delay maximal heat flow in the absence of uranium. $k_{\max(i)}$ and $k_{\max(0)}$ are the corresponding values of the growth rates at the i^{th} uranium concentration uranium concentration and the control without uranium, respectively.

2.3.3 Cell counting measurements

2.3.3.1 Correlating OD_{600} with cell number

Since a flow cytometry was not available in the controlled area, relative measurements of the cell number were performed based on the optical density at 600 nm (OD_{600}). The flow cytometer system CyFlow® space (Partec, Germany) was then used to correlate the OD with absolute cell numbers. The bacterial cultures were grown in 50% R2A medium overnight. The cultures were centrifuged (10000 rpm for 10 min at 4 °C each time) and washed with phosphate buffered saline containing, per liter, 8 g NaCl, 0.2 g KCl, 1.44 g $2\text{H}_2\text{O} \times \text{Na}_2\text{HPO}_4$ and 0.24 g KH_2PO_4 . The washing process was repeated three times. The OD_{600} was measured for the samples, and then different dilutions of each sample were prepared to be measured by the flow cytometer. The initial number of cells N_0 that correlates with OD_{600} of 0.0005 regarding each bacterial strain is included in Table 2.1. However, because of the extremely low number of cells, neither were pellets formed after centrifugation, nor did the samples show turbidity that would have allowed measuring its optical density.

Table 2-1. Generation time and the average initial number of cells N_0 in the samples of each strain grown in 50 % R2A medium at 30 °C in the absence of uranium.

Bacterial strain	Generation time G (h)	N_0 (cell)	Std
A12	0.54	69740	12202
B53	0.64	100669	2404
TB8	0.89	141878	7790
NCTC	0.51	52724	2389

2.3.3.2 Colony forming units (CFU) counting

CFU counting of the strain JG-B53 was performed to correlate the thermal signal measured by the microcalorimeter to the number of viable bacterial cells in the ampoule. Agar plates of 50 % R2A were prepared by adding 15 g/l agar to the ingredient of R2A medium before autoclaving. The mixture was autoclaved at 120 °C for 20 min then it was distributed on the plates. Calorimetric experiments were performed as described in section 2.3.1 only with using six minicalorimeters for controls (only medium and bacteria), and the other six were used for one uranium concentration.

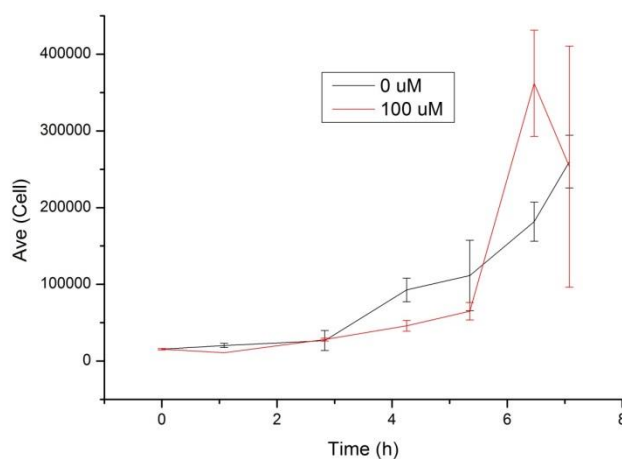


Figure 2-1: CFU counting of *Lysinibacillus sphaericus* JG-B53.

A colony forming unit counting for the strain JG-B53 was performed to correlate the thermograms of the calorimetry to the viable cell numbers.

As the calorimetric experiment was running, one control together with one sample with uranium were taken at a specific time of the experiments to be diluted and used to inoculate agar plate for CFU counting. This sampling was done six times at different time-

points that cover the exponential phase, the peak and one point after the peak. Unfortunately, it was very difficult to obtain plates with defined colonies, therefore, this experiment was repeated several times with 10, 50, 100 and 150 μM uranyl. Nevertheless, the results of the successfully grown plates exhibit very large error bars as shown in Figure 2-1, therefore these results will not be used for the correlation or any further discussion. This demonstrates the extremely high sensitivity and time resolution of calorimetric data versus CFU counting.

2.3.4 Dose estimation

To calculate the activity related to each concentration of uranium the following formula was used:

$$A [Bq/sample] = C [mol/l] \times M [g/mol] \times V [l] \times A_s [Bq/g] \quad (\text{Eq. 2-4})$$

with A: the activity in the sample, C: the molarity, M: the molar mass, V: volume of the sample and A_s : the specific activity of the radioactive element. Table 2-2 shows the activity given to each sample.

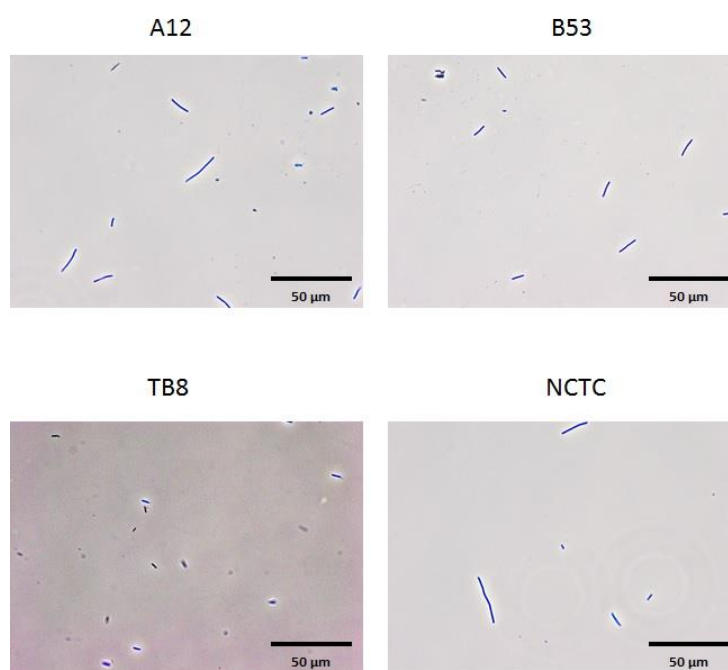
A rough estimation of the absorbed dose can be calculated after considering several assumptions using “MIRD cellular S-values” (Goddu et al., 1997). This reference gives the self-absorbed dose per unit cumulated activity for specific radionuclides and monoenergetic electron and alpha particle emitters incorporated into different compartments eukaryotic cells. It assumes that the cell and the nucleus are two centered spheres. The dose is calculated for the whole cell together with the nucleus or separately, and tabulated according to the radius of the cell, the nucleus, the part of the cell where the activity is distributed and the energy of the emitted particle.

As mentioned in section 2.2, uranium is deposited on the cell surface for all four studied strains. Therefore, the self-absorbed dose of the cell as a target when the activity is distributed on the cell surface was used ($S(C \leftarrow CS)$). Furthermore, the studied bacterial strains are all rod-like shaped with an average diameter of 1 μm and length between 7 and 10 μm and they tend to form chains (Fig. 2-2).

The smallest cell radius considered in the above- mentioned reference is 3 μm and was used here for further evaluations. However, this radius for the bacterial cells probably overestimates the dose. The energies of α -particles emitted by the isotopes of natural uranium are: 4.27 MeV for ^{238}U , 4.68 MeV for ^{235}U and 4.86 MeV for ^{234}U (IAEA, 2015).

Table 2-2. The Radioactivities of U_{nat} that were introduced to the samples and the related roughly estimated self-absorbed dose.

[U] per sample (μM)	Activity of U_{nat} (Bq/sample)	Roughly estimated self-absorbed dose D (mGy/cell)			
		JG-A12	JG-B53	JG-TB8	NCTC 9602
0.1	0.001	0.005	0.004	0.004	0.007
0.5	0.006	0.032	0.026	0.026	0.04
1	0.012	0.064	0.053	0.052	0.08
1.5	0.018	0.096	0.079	0.078	0.12
2.22	0.027	0.145	0.119	0.117	0.181
4.45	0.054	0.289	0.237	0.234	0.361
10	0.121	0.648	0.532	0.525	0.809
13.35	0.161	0.862	0.707	0.698	1.076
50	0.605	3.238	2.659	2.623	4.045
100	1.209	6.471	5.313	5.242	8.083
150	1.814	9.709	7.971	7.865	12.128

**Figure 2-2:** Light microscopic pictures of the bacterial strains.

The set of α -particle energies available in the reference is integers between 3-10 MeV, therefore it was assumed for this estimation that the energy of the α -particle is 5 MeV, which again overestimates of the dose. The average life time of the cell (generation time $G = \ln(2)/k$) and the number of irradiated cells (considered to be equal to the initial cell number N_0) are listed in Table 2-1.

In summary, the assumptions are: 1) cells are spheres of 3 μm radius, 2) the activity is deposited on the cell surfaces, 3) the energy of α -particles is 5 MeV, 4) the average life time of the cell is G (h) and 5) the number of irradiated cells is N_0 . According to these assumptions, the converting factor of activity to absorbed dose given by the reference is $d = 0.192 \text{ Gy/Bq s}$. The dose is then calculated by the following formula:

$$D [\text{Gy/cell}] = A [\text{Bq/sample}] \times d [\text{Gy/Bq s}] \times G [\text{s}] / N_0 [\text{Cell/sample}] \quad (\text{Eq. 2-5})$$

Table 2-2 shows this roughly estimated self-absorbed dose D (mGy/cell). This assumption may overestimate the self-absorbed dose, but allows comparison with the literature.

2.3.5 Data interpretation and calibration experiments

As mentioned in section 1.4, Katsutada Takahashi was the first to qualitatively distinguish antimicrobial toxic effects as “bacteriostatic” or “bactericidal” using calorimetry. It was shown that the decrease in the growth rate is related to the bacteriostatic effect of the toxin, while the delayed appearance of the maximal heat flow at preserved growth rate (retardation) is related to bactericidal effect. Retardation of the maximal heat flow is a common feature of both bactericidal and bacteriostatic effects (Takahashi, 2000). Many toxins may exhibit both actions, however, their action pattern is assumed to change with their concentrations (Wirkner and Takahashi, 2000). In other words, retardation only indicates a bactericidal effect, whereas retardation would be accompanied by growth inhibition for bacteriostatic action. Additionally, as will be seen in section 2.4.3 with strain JG-TB8 (Fig. 2-5 (A) and Table 2-5) at concentrations of 10-150 μM uranium, the decrement in growth rate was not accompanied by retardation, rather the maximal heat flow was reduced, indicating that Takahashi’s interpretation of the “retardation” should be reconsidered. “Retardation” is in fact not a lag phase in growth but it can be attributed to a reduced number of initially dividing cells due to lethality or to cell cycle arrest already in the fresh inoculates. It may also arise from the reorientation of the cell metabolism before the onset of growth and can be

accompanied by change in growth rate. It is difficult to relate the observed retardation to its real cause without cell counting of the uranium-containing samples. Nevertheless, it was possible to relate the observed retardation caused by uranium to the initial cell number that causes the same retardation under normal conditions by control experiments, where initial cell numbers were varied on purpose to be used as a reference. It was not necessary to perform these control experiments with all the strains. Instead, these experiments could be restricted to JG-B53, which showed the largest retardations, and to NCTC 9602 as the reference strain. These experiments were performed as described in section 2.3.1. The initial OD_{600} was varied as following: 0.00025, 0.0005, 0.001, 0.002 and 0.004. The samples of each experiment were prepared in duplicates, and two blank samples that contained only medium were run in order to check the sterility of the medium.

On the other hand, the factors that affect the maximal heat flow were not discussed neither by Takahashi nor, to the best of my knowledge, by any other research group. In this project there were cases where P_{max} decreased with k decrement as would be expected for bacterial growth. In other cases (chapter 3) the reduction of P_{max} was accompanied by a retardation while k was not affected. In other cases, there was no clear relation between the change of maximal heat flow, retardation and growth rate. Therefore, it is important to investigate the factors that affect the maximal heat flow. In addition to cell number N and metabolic heat flow per cell m as seen in Eq. 1-6, a very important factor is the supply with nutrients in the medium. Therefore, the following assumptions and definitions were made to take nutrient supply into account:

- n_{tot} : the total amount of nutrients in the medium at $t = 0$ (in J).
 - $n_{tot} = h \cdot V$;
 - (h) is the energy provided by the nutrients per the volume of the medium, it should be constant for each medium, and it should decrease with bacterial growth due to the consumption. (in J/l).
 - (V) is the volume of the medium. (in l)
- n_c : the amount of energy provided by the nutrient for one cell from its creation until its division (in J/cell).
 - n_c should be constant in ideal conditions during growth phase.
 - n_c is transformed into biomass and metabolic heat, thus:

$$n_c = j \cdot M_{cell} + Q_c$$

- j : is the energy transferred into biomass- factor (J/kg)

Chapter 2

- M_{cell} : is mass of one cell (kg/cell)
- Q_c : is the heat released by one cell (J/cell)
- n_t : the remaining nutritional energy in the medium at time (t) (in J).
 - $n_t = n_{\text{tot}} - n_c \cdot N(t)$
 - $N(t) = N_0 \cdot e^{k \cdot t}$ number of cells at time (t).
 - $N(t)$ is the number of the bacterial cells at time (t).
 - N_0 is the number of the bacterial cells at time (t=0)
 - k is the growth rate.
- n_{tc} : the remaining nutrients per cell. (in J/cell).
 - $n_{tc} = \frac{n_t}{N(t)}$
 - $P(t) = m \cdot N(t)$ the heat flow at time (t).
 - m : the metabolic heat flow released by each bacterium. It keeps a constant value during the growth phase.

Taking all assumptions above into consideration then at (t=0):

$$n_t = n_{\text{tot}}$$

At time (t):

$$n_t = n_{\text{tot}} - n_c \cdot N(t)$$

A drastic change in the growth phase will occur when the nutrient left per cell provides less energy than that needed for one further life cycle:

$$n_{tc} < n_c \quad \Rightarrow \quad \frac{n_t}{N(t)} < n_c \quad \Rightarrow \quad \frac{n_{\text{tot}} - n_c \cdot N(t)}{N(t)} < n_c \quad \Rightarrow$$

$$n_{\text{tot}} < 2 \cdot n_c \cdot N(t) \quad \Rightarrow \quad N(t) > \frac{n_{\text{tot}}}{2 \cdot n_c}$$

At the boundaries:

$$n_{tc} = n_c, t = t_b \quad \Rightarrow \quad N(t_b) = \frac{n_{\text{tot}}}{2 \cdot n_c} \quad \Rightarrow \quad N(t_b) = \frac{h \cdot V}{2 \cdot n_c} \quad \Rightarrow$$

$$P(t_b) = \frac{h \cdot V \cdot m}{2 \cdot n_c}$$

With the reasonable approximation $P_{\text{max}} \approx P(t_b)$:

$$P_{\text{max}} = \frac{h \cdot V \cdot m}{2 \cdot n_c} \quad (\text{Eq. 2-6})$$

Another important factor needs to be considered in the quantitative model. Bacterial growth in the unstirred microcalorimetric ampoules leads to the sedimentation of the cells, which, therefore, will consume the nutrients at the bottom of the ampoule. Accordingly, nutrient

consumption and by-product formation will be restricted primarily to the vicinity of the cells (effective volume or V_{eff}). The nutrients in this volume proceed faster than diffusion of nutrients from the top layer to the bottom of the ampoule. Consequently, only small portion of the nutrient in the medium is available to sustain exponential bacterial growth. Then equation 2-6 should be rewritten as:

$$P_{max} = \frac{h \cdot V_{eff} \cdot m}{2 \cdot n_c} \quad (\text{Eq. 2-7})$$

keeping in mind that this equation can be applied only at the transition point from exponential to stationary phase and that it is not valid during the growth phase. This equation shows that maximal heat flow is governed by metabolism-related parameters (m and n_c) and medium-related parameters (h and V_{eff}). When the cell is subjected to heavy metal stress, its metabolism will get affected. This leads to a decrease of m accompanied by lowering the growth rate k^3 , and as a consequence to a distinguished change P_{max} , typical of a bacteriostatic effect. On the other hand, h is a constant that is related to the nutrient concentration in the medium, which will not affect P_{max} when the studies use the same medium. Finally, a change in V_{eff} is not expected to be induced by metal stress. Therefore, it is not a parameter from which bacteriostatic or bactericidal effects can be deduced.

In this study, 50% R2A medium was used for all experiments, therefore, h was constant and it did not affect P_{max} . (It is noteworthy that h slightly changes between different charges of freshly prepared medium. This is the reason behind the slight change in P_{max} among the control samples of identical strains in different experiments as seen in tables 2-3 to 2-6). Additionally, there is no reason to assume a change in the effective volume by the addition of natural uranium. Therefore, in this study the measured P_{max} will be related to the metabolic activity of cells. Nevertheless, calculating the effective volume may help to understand how P_{max} of bacterial culture could also be affected under certain conditions as will be seen in chapter 3.

In order to calculate the effective volume, a control sample that included only medium and bacteria as described in section 2.3.1 was prepared in the ampoule of the isothermal titration calorimeter (ITC). In contrast to the typical IMC ampoule experiment, however, the

$$\begin{aligned} n_c &= j \cdot M_{cell} + Q_c \quad \rightarrow \quad Q_c = n_c - j \cdot M_{cell} \quad \rightarrow \quad N(t) \cdot Q_c = N(t) \cdot (n_c - j \cdot M_{cell}) \rightarrow \\ Q(t) &= N(t) \cdot (n_c - j \cdot M_{cell}) \quad \rightarrow \quad P(t) = k \cdot (n_c - j \cdot M_{cell}) \cdot N(t) + P_0 \quad \rightarrow \\ m &= k \cdot (n_c - j \cdot M_{cell}) \quad \rightarrow \quad k = \frac{m}{(n_c - j \cdot M_{cell})} \end{aligned}$$

culture medium was constantly stirred. Stirring the culture assures the regular distribution of the cells in the medium, which leads to identify of the total volume of the sample as effective volume in this case. The stirrer was set at 70 rpm. This experiment was performed with JG-B53 and NCTC 9602. Both ampoule and stirrer were sterilized with 70 % ethanol. The heat flow caused by the stirrer was measured and subtracted from the thermogram. Since in this experiment, V_{eff} is equal to the total volume of the medium ($V_{tot} = 2$ ml), one can write with Eq. 2-7:

$$V_{eff} = \frac{(P_{max})_{without\ stirring} \cdot V_{tot}}{(P_{max})_{stirrer}} \quad (\text{Eq. 2-8})$$

The average of the measured maximal heat flow of the control samples was calculated for both strains and used for defining V_{eff} .

2.4 Results

In order to study the effect of uranium on the metabolic activity of the waste pile isolates *Lysinibacillus sphaericus* JG-A12, *Lysinibacillus sphaericus* JG-B53 and *Paenibacillus* JG-TB8 as well as the reference strain *Lysinibacillus sphaericus* NCTC 9602, these cells were grown in 50 % R2A at 30 °C. R2A is a phosphate-poor medium which prevents excessive uranium precipitation at the studied pH of ~7. The metabolic heat production of the cultures was monitored under different concentrations of U_{nat} . Equivalent experiments performed with $Mg(NO_3)_2$ addressed the effect of nitrate on the metabolic activity of the mentioned strains.

2.4.1 The effect of U_{nat} on the waste pile isolate *Lysinibacillus sphaericus* JG-A12

Figure 2-3 (A) shows thermograms for the growth of JG-A12 under the stress of 0, 10, 50, 100 and 150 μ M uranyl. The curves are the average of duplicate experiments. After a short lag phase, the metabolic heat flow increased exponentially and was maximal after 3.73 to 4.27 h. Then the signal declined and reached a shoulder after ~ 6 h at 15 μ W before it attained a steady level after 11 h at around 5-10 μ W indicating that at this point some cells were still alive but the surrounding medium was not sufficient for proliferation. The thermogram at 10 μ M uranyl appeared to be not affected in comparison to the control except for a small retardation. The increased addition of U_{nat} caused a successive reduction of P_{max} accompanied by an increase of T_{max} . The addition of 150 μ M U_{nat} reduced the maximal heat flow by ~ 40.6 % and caused a retardation by ~ 14.5 % (Table 2-3).

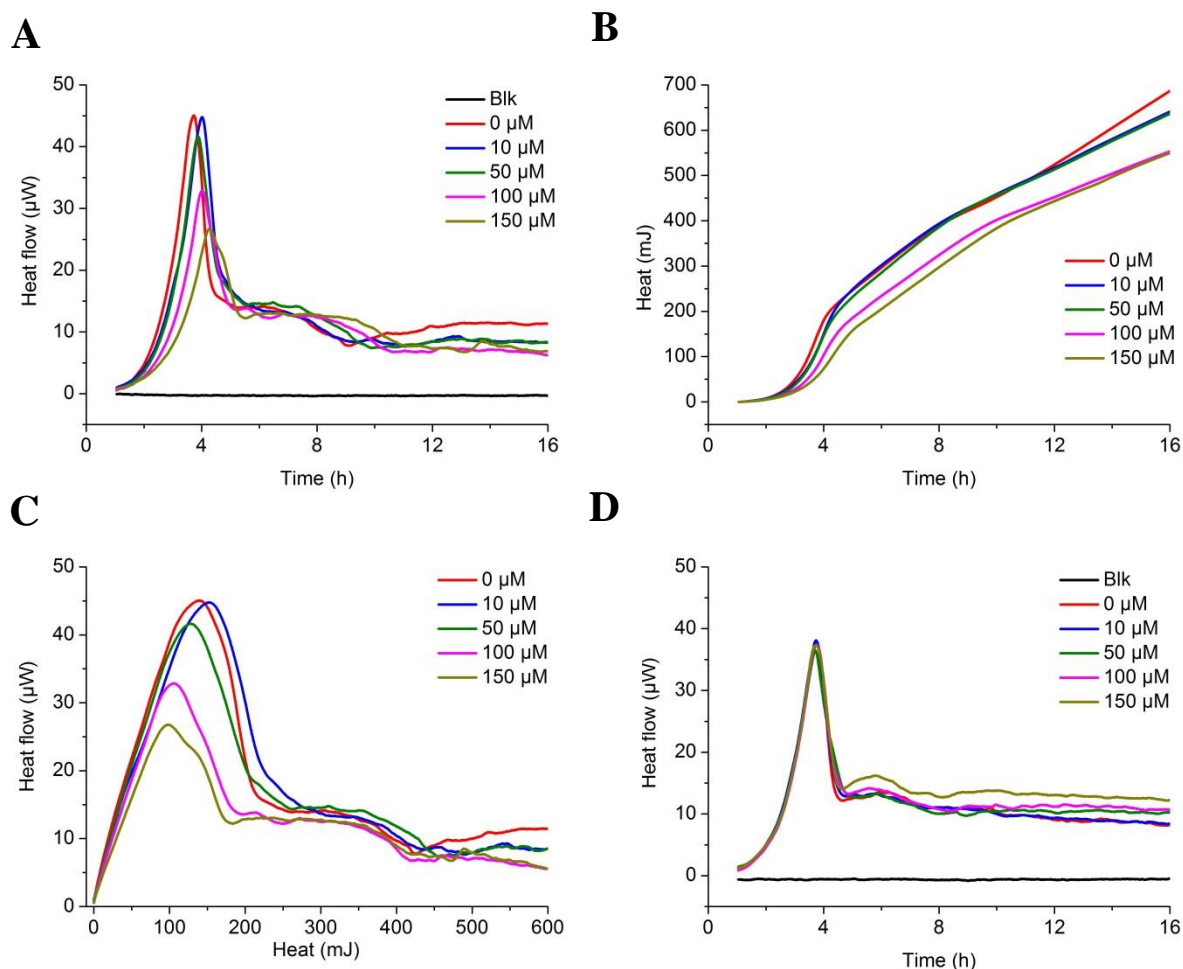


Figure 2-3: Effect of natural uranium on the metabolic heat flow of *Lysinibacillus sphaericus* JG-A12.

A: Heat flow is plotted vs. time. Bacteria were cultured at 30 °C in 2 ml 50% R2A medium. Natural uranium was added as $\text{UO}_2(\text{NO}_3)_2$ at the indicated final concentrations. B: Heat vs. time. C: Heat flow vs. heat. Regression lines were calculated for the linear segments of the plot. Growth rate constants for the phase of exponential growth were derived from the slopes (Table 2-3). The curves correspond to the average of duplicate.

Integration of the heat flow over time produces heat vs. time diagrams (Fig.2- 3 B). Assuming that the amount of heat produced during the formation of an individual bacterial cell stays constant during the entire growth phase, the total heat scales with cell number in this phase. Thus, the heat vs. time diagram approximates the increase in cell number during growth phase (Braissant et al., 2013; Bricheux et al., 2013). The quantitative analysis of the thermograms was restricted to the growth phases revealed by the heat flow measurements. These phases appear as linear segments in the heat flow vs. heat plots shown in Figure 2-3 (C). Their slopes determine the underlying growth rates because both heat and heat flow are proportional to the cell number in the growth phases (Table 2-3). The results show that the average growth rate of JG-A12 in absence of uranium was $k = 1.288 \pm 0.070 \text{ h}^{-1}$. The addition of 10 μM uranyl

reduced the growth rate by ~ 13 %. At 50 μM it seems that the growth was surprisingly recovered but still less than the control by ~ 2 %. Further increment of uranyl concentration reduced the growth rate again by ~ 9.5 % and ~ 21 % at 100 and 150 μM respectively.

Table 2-3. U_{nat} -dependent growth parameters of JG-A12; T_{max} (h), P_{max} (μW) and k (h^{-1}) together with percentage errors and the percentage inhibitory ratio of each of the three parameters.

$[U_{\text{nat}}]$ (μM)	T_{max} (h)	% Error of T_{max}	P_{max} (μW)	% Error of P_{max}	k (h^{-1})	R	$(I)_t$ (%)	$(I)_p$ (%)	$(I)_k$ (%)
0	4.02	0.29	39.35	0.61	1.255	0.998	0	0	0
0.1	3.99	0.24	37.27	2.16	1.302	0.998	-0.62	-5.29	3.76
0.5	4.04	0.09	35.69	3.47	1.356	0.998	0.48	-9.29	8.01
1	4.07	0.38	35.78	2.08	1.319	0.998	1.33	-9.07	5.13
1.5	4	0.48	36.31	0.97	1.354	0.997	-0.29	-7.72	7.85
0	4.44	2.77	33.88	1.04	1.252	0.999	0	0	0
2.22	4.48	0.29	28.83	1.75	1.227	0.999	0.92	-14.92	-2
4.45	4.6	4.08	27.21	8.06	1.343	0.998	3.6	-19.7	7.31
13.35	4.43	1.09	31.64	7.49	1.381	0.998	-0.15	-6.62	10.34
0	3.73	0.5	45.13	1.73	1.357	0.996	0	0	0
10	3.98	2.02	45.57	3	1.177	0.996	6.79	0.97	-13.31
50	3.88	0.53	41.76	1.92	1.327	0.998	3.99	-7.48	-2.24
100	4.02	0	32.86	1.81	1.228	0.998	7.85	-27.2	-9.51
150	4.27	0.84	26.81	7.69	1.068	0.999	14.5	-40.59	-21.31

The non-monotonous dependence of the growth rate with respect to the uranyl concentration is indicative of an adaptational behavior of the cells. Apparently, at a threshold of ~10 μM uranyl, a defense mechanism is induced in the cell. Such mechanisms are well known for heavy metal detoxification. For example, comparable μM concentrations induce the expression of a copper-detoxifying biomolecules in the cell (Dameron and Harrison, 1998). Similarly, uranyl above 10 μM appears to provide the signal for a heavy metal detoxifying system in the waste pile isolate of uranyl in the form of uranyl nitrate. These results show that microcalorimeter is a well suited instrument for sensitive and precise determinations of effects of uranium on bacterial metabolism.

Equivalent experiments were performed with $\text{Mg}(\text{NO}_3)_2$ as shown in Fig. 2-3 (D). The addition of $\text{Mg}(\text{NO}_3)_2$ did not affect the growth behavior of JG-A12 within the evaluated time range of the thermogram. Although NO_3 is a potential nitrogen source, it is not significantly used by the strain and thus does not interfere with the toxicity assessment.

2.4.2 The effect of U_{nat} on the waste pile isolate *Lysinibacillus sphaericus* JG-B53

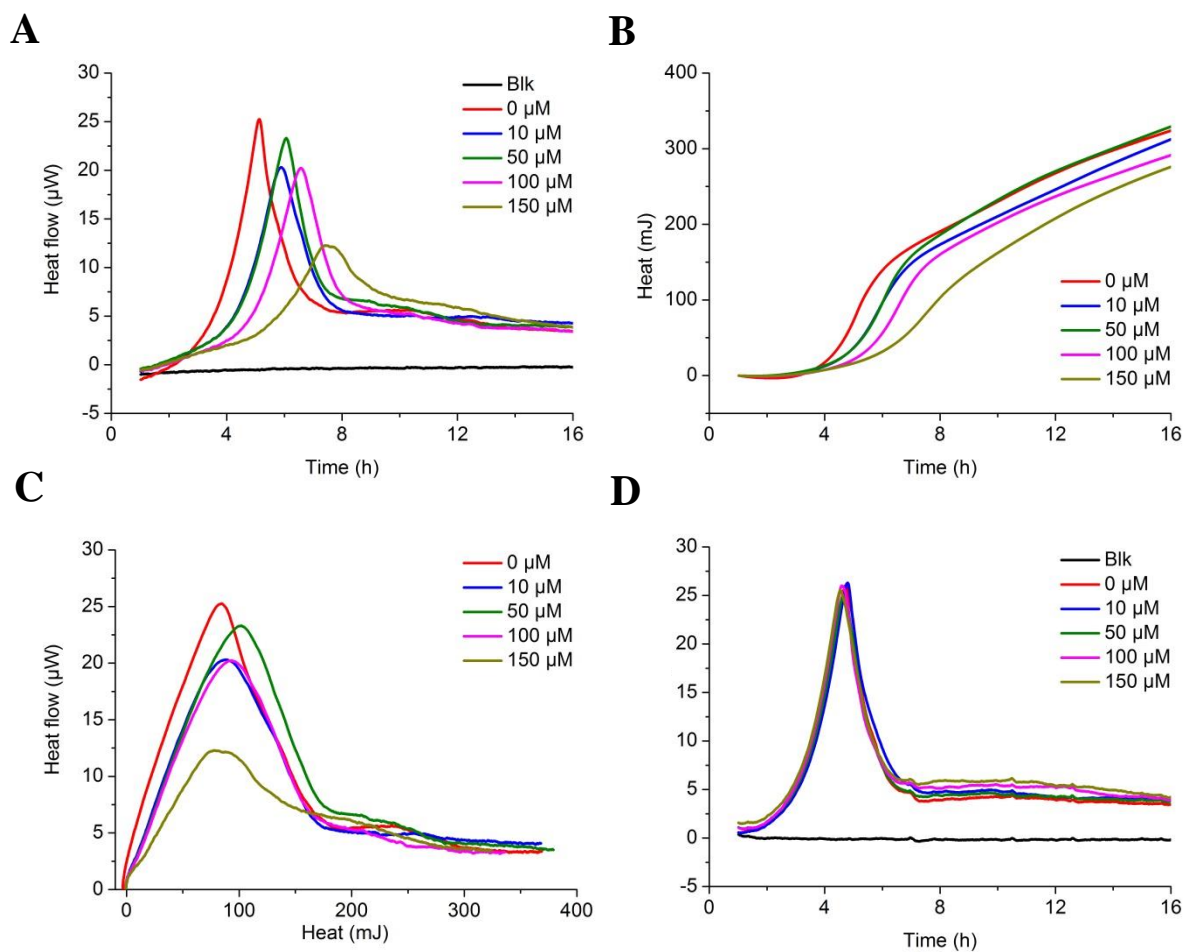


Figure 2-4: Effect of natural uranium on the metabolic heat flow of *Lysinibacillus sphaericus* JG-B53.

A: Heat flow is plotted vs. time. Bacteria were cultured at 30 °C in 2 ml 50% R2A medium. Natural uranium was added as $\text{UO}_2(\text{NO}_3)_2$ at the indicated final concentrations. B: Heat vs. time. C: Heat flow vs. heat. Regression lines were calculated for the linear segments of the plot. Growth rate constants for the phase of exponential growth were derived from the slopes (Table 2-4). The curves correspond to the average of duplicate.

Figure 2-4 (A) shows thermograms for the growth of JG-B53 in the presence of various $\text{UO}_2(\text{NO}_3)_2$ in the concentration range 0 to 150 μM under the same conditions used

for JG-A12. These curves correspond to the average of duplicates. The general appearance of the thermograms is very similar to that of JG-A12.

After a lag phase, the metabolic heat flow increased exponentially and reached P_{\max} after 5 to 8 h, before the signal declined to a rather stable thermal power of $\sim 5 \mu\text{W}$ after 14 h, indicating the persistence of life cells with low metabolic activity. Unlike JG-A12, the addition of $10 \mu\text{M}$ uranyl to the JG-B53 strain reduced the maximal heat flow by $\sim 16 \%$ and caused a retardation by $\sim 15.5 \%$. Interestingly, at $50 \mu\text{M}$ uranyl the thermogram peak appeared almost at the same time as with $10 \mu\text{M}$ and surprisingly, P_{\max} was higher than that with $10 \mu\text{M}$ uranyl (although still lower than the control by $\sim 7 \%$). At $100 \mu\text{M}$ uranyl, P_{\max} was almost of the same height as with $10 \mu\text{M}$ uranyl but delayed by $\sim 28.5 \%$ in comparison to the control. Further increment of $\text{UO}_2(\text{NO}_3)_2$ to $150 \mu\text{M}$ decreased and delayed the maximal heat flow by 51.27% and 44.69% respectively (Table 2-4). Figure 2-4 (B) shows the heat vs. time diagrams. The quantitative analysis of the thermograms was again restricted to the exponential growth phases revealed by the linear segments in the heat flow vs. heat diagram (see Fig. 2-4 C and Table 2-4). The results show that the average growth rate of JG-B53 in absence of uranium was $k = 1.092 \pm 0.029 \text{ h}^{-1}$. The addition of $10 \mu\text{M}$ uranyl reduced the growth rate by $\sim 13 \%$, and the addition of $50 \mu\text{M}$ did not cause further reduction in comparison to $10 \mu\text{M}$. Remarkably, however, the P_{\max} value increased at $50 \mu\text{M}$ uranium above that attained at $10 \mu\text{M}$. Thus the strain appears to be particularly adapted to the growth in presence of $50 \mu\text{M}$ uranium, where it growth slower than in the absence of uranium but, nevertheless, reaches a high metabolic activity. Further increment of uranyl concentration has reduced the growth rate by $\sim 18 \%$ and $\sim 47 \%$ at 100 and $150 \mu\text{M}$ respectively.

In summary, both the dependence of the peak heat flow and the growth rate on uranyl concentration exhibited an unexpected non-monotonous behavior with a critical change in metal-sensitivity in the 10 to $50 \mu\text{M}$ range of uranyl. This response indicates the activation of a heavy metal-detoxification mechanism at around $10 \mu\text{M}$ uranyl which allows the bacteria to resume improved growth above this concentration. Beyond $50 \mu\text{M}$, the detrimental effect of uranyl prevails.

The equivalent experiment performed with $\text{Mg}(\text{NO}_3)_2$ is shown in Fig. 2-4 (D) to address the possible effect of the nitrate (a potential nutrient) on the growth behavior. As in the case of JG-A12, it shows that the addition of $\text{Mg}(\text{NO}_3)_2$ did not affect the growth behavior of JG-B53 until the thermogram reached the saturation in the decline phase, where it shows a rise in the steady state thermal power with increasing $\text{Mg}(\text{NO}_3)_2$ concentrations. However,

this change would not affect the results related to the effect of $\text{UO}_2(\text{NO}_3)_2$ because the analysis is restricted to the growth phase and the maximal heat flow which are independent of $\text{Mg}(\text{NO}_3)_2$.

Table 2-4. U_{nat} -dependent growth parameters of JG-B53; $T_{\text{max}}(\text{h})$, $P_{\text{max}}(\mu\text{W})$ and $k(\text{h}^{-1})$ together with percentage errors and the percentage inhibitory ratio of each of the three parameters.

$[U_{\text{nat}}]$ (μM)	T_{max} (h)	% Error of T_{max}	P_{max} (μW)	% Error of P_{max}	k (h^{-1})	R	$(I)_t$ (%)	$(I)_p$ (%)	$(I)_k$ (%)
0	5.74	0.83	29	1.45	1.123	0.998	0	0	0
0.1	5.93	0.4	25.48	3.12	1.117	0.998	3.21	-12.12	-0.57
0.5	6.47	0.85	24.11	2.74	1.128	0.999	12.68	-16.87	0.44
1	6.64	1.13	23.54	2.74	1.077	0.999	15.65	-18.83	-4.08
1.5	6.69	2.45	23.4	1.01	0.98	0.999	16.49	-19.29	-12.73
0	5.53	0	29.23	3.96	1.065	0.999	0	0	0
2.22	6.53	0.54	23.44	0.34	1.089	0.999	18.08	-19.79	2.26
4.45	6.08	0.36	23.34	0.7	0.962	0.999	9.85	-20.16	-9.65
13.35	6.39	0.77	28.13	7.61	1.074	0.999	15.48	-3.77	0.86
0	5.13	0.42	25.35	1.95	1.088	0.996	0	0	0
10	5.93	2.26	21.23	4.2	0.945	0.999	15.52	-16.24	-13.14
50	6.06	1.15	23.57	5.39	0.949	0.999	18.16	-7.01	-12.79
100	6.59	1.42	20.68	3.33	0.892	0.999	28.51	-18.41	-18.03
150	7.42	1.01	12.35	1.38	0.579	0.998	44.69	-51.27	-46.81

2.4.3 The effect of U_{nat} on the waste pile isolate *Paenibacillus* JG-TB8

Figure 2-5 (A) shows the thermograms for the growth of JG-TB8 at $\text{UO}_2(\text{NO}_3)_2$ concentrations of 0 to 150 μM . These curves are averages of duplicates. The general pattern of the thermograms of JG-TB8 is slightly different from those of JG-A12 and JG-B53. After a short lag phase, the metabolic heat flow increased exponentially and was maximal after ~ 7 h. The addition of $\text{UO}_2(\text{NO}_3)_2$ reduced P_{max} successively but with almost no retardation. The addition of 150 μM U_{nat} reduced the maximal heat flow by $\sim 48\%$ (Table 2-5). The shoulder succeeding the peak is more pronounced than those in the other strains. It appeared at a heat

flow that is about 50 % of the preceding heat flow maximum, and decreased with increasing concentration of $\text{UO}_2(\text{NO}_3)_2$. Figure 3-3 (B) shows the heat vs. time diagrams demonstrating that the total released heat was reduced in the presence of $\text{UO}_2(\text{NO}_3)_2$. Assuming that the

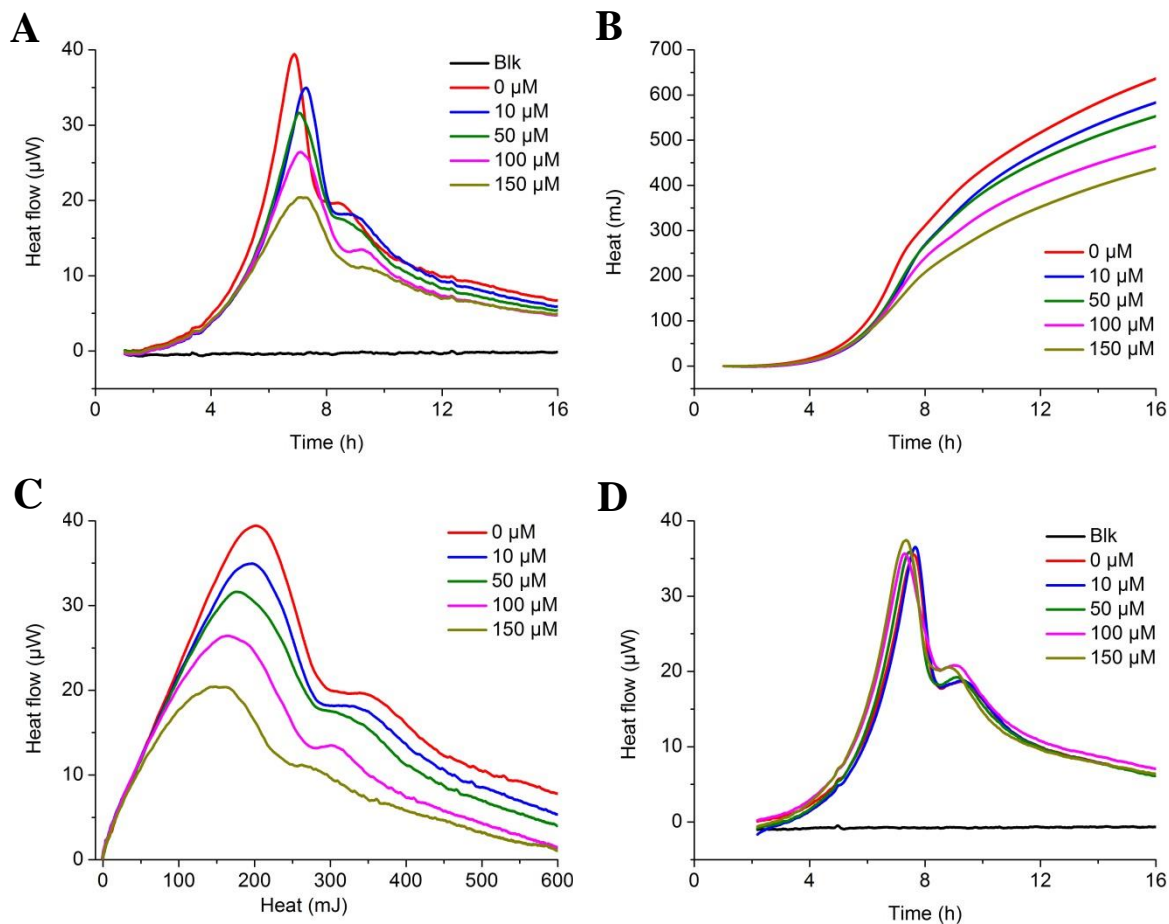


Figure 2-5: Effect of natural uranium on the metabolic heat flow of *Paenibacillus* JG-TB8.

A: Heat flow is plotted vs. time. Bacteria were cultured at 30 °C in 2 ml 50% R2A medium. Natural uranium was added as $\text{UO}_2(\text{NO}_3)_2$ at the indicated final concentrations. B: Heat vs. time. C: Heat flow vs. heat. Regression lines were calculated for the linear segments of the plot. Growth rate constants for the phase of exponential growth were derived from the slopes (Table 2-5). The curves correspond to the average of duplicate.

amount of heat produced during the formation of an individual bacterial cell stays constant during the entire growth phase, the total heat scales with cell number. Thus, the heat vs. time diagram approximates the increase in cell number during growth phase (Braissant et al., 2013; Bricheux et al., 2013). Fig. 2-5 (C) shows the exponential growth phases as linear segments in a heat flow vs. heat diagram. The growth rates were calculated using the linear regression method of these linear segments (Table 2-5). The results show that the average growth rate of JG-TB8 in absence of uranium was $k = 0.776 \pm 0.006 \text{ h}^{-1}$. The results show that the addition of 10 μM reduced the growth rate by $\sim 10\%$. At 50 and 100 μM the growth rate was less

affected than at 10 μM , but still reduced in comparison to the control by $\sim 7\%$ and 6% respectively. Further increase of uranyl concentration to 150 μM reduced the growth rate by $\sim 18.5\%$. The equivalent experiment performed with $\text{Mg}(\text{NO}_3)_2$ is demonstrated in Fig. 2-5 (D). It shows that the addition of $\text{Mg}(\text{NO}_3)_2$ did not affect the growth behavior of JG-TB8, thus excluding interference with nitrate metabolism.

Table 2-5. U_{nat} -dependent growth parameters of JG-TB8; $T_{\text{max}}(\text{h})$, $P_{\text{max}}(\mu\text{W})$ and $k(\text{h}^{-1})$ together with percentage errors and the percentage inhibitory ratio of each of the three parameters.

$[U_{\text{nat}}]$ (μM)	T_{max} (h)	% Error of T_{max}	P_{max} (μW)	% Error of P_{max}	k (h^{-1})	R	(I_t) (%)	(I_p) (%)	(I_k) (%)
0	7.91	0.87	34.98	2.8	0.769	0.999	0	0	0
0.1	7.95	0.23	35.03	4	0.743	0.999	0.5	0.15	-3.38
0.5	8.56	0.68	28.99	3.04	0.665	0.998	8.14	-17.11	-13.63
1	8.78	0.16	29.83	0.92	0.639	0.998	11.01	-14.73	-16.88
1.5	8.76	0.39	29.62	1.11	0.691	0.997	10.72	-15.33	-10.24
0	8.66	0.61	36.37	0.3	0.781	0.999	0	0	0
2.22	9.42	0.11	26.65	1.76	0.558	0.996	8.77	-26.72	-28.53
4.45	9.14	1.33	31.32	0.06	0.634	0.998	5.59	-13.9	-18.77
13.35	9	0.11	28.62	2.93	0.674	0.996	3.98	-21.32	-13.74
0	6.89	0.05	39.42	1.24	0.778	0.999	0	0	0
10	7.27	0.66	35.04	1.24	0.701	0.999	5.56	-11.11	-9.82
50	7.04	0.07	31.62	1.3	0.723	0.998	2.28	-19.78	-7.07
100	7.08	0.54	26.44	0.22	0.724	0.997	2.86	-32.93	-6.87
150	7.21	1.39	20.51	2.84	0.634	0.994	4.66	-47.96	-18.46

Clearly, the peak heat flow showed dependence on the uranyl concentration, but with no significant retardation, unlike the other strains. Additionally, JG-TB8 did not show the adaptational effect that was observed with JG-A12 and JG-B53; rather it showed the expected monotonous response to uranyl stress. Although there are no drastic differences in growth behavior among the isolates, JG-TB8 appears to be the most uranyl-sensitive strain.

2.4.4 The effect of U_{nat} on the reference strain *Lysinibacillus sphaericus* NCTC 9602

Figure 2-6 (A) shows thermograms for the growth of the reference strain NCTC 9602 in the presence of various $UO_2(NO_3)_2$ concentrations between 0 and 150 μM (trace are the average of duplicates). After a short lag phase, the metabolic heat flow increased exponentially and was maximal after 3.95 to 4.39 h, then the signal declined reaching a shoulder after ~ 6 h at 15 μW and attained a saturation after 10 h at around 5-10 μW similarly to the isolates. The increased addition of U_{nat} caused a successive reduction accompanied by a small retardation of the peaks. The highest uranyl concentration of 150 μM U_{nat} reduced the maximal heat flow by $\sim 30\%$ and caused a retardation by 11.14% (Table 2-6). Integration of the heat flow over time produces heat vs. time diagrams (Fig. 2-6 B). Assuming again that the amount of heat produced during the formation of an individual bacterial cell stays constant during the entire growth phase, this curve scales with cell number showing the successive decline of the population size with uranyl concentration. The linear segments in the heat flow vs. heat shown in Figure 2-6 (C) correspond to the growth rates listed in Table 2-6. The results show that the average growth rate of JG-A12 in absence of uranium was $k = 1.370 \pm 0.046 \text{ h}^{-1}$. The addition of 10 and 50 μM did not cause a reduction in the growth rate in comparison to the control. However, higher uranyl concentrations reduced the growth rate by $\sim 7\%$ and $\sim 11\%$ at 100 and 150 μM respectively. The equivalent experiment performed with $Mg(NO_3)_2$ is shown in Fig. 2-6 (D). It demonstrates that the addition of $Mg(NO_3)_2$ did not affect the growth behavior of NCTC 9602 until the thermogram reached the saturation in the decline phase, where it appears broader than the one related to $UO_2(NO_3)_2$. However, this change would not affect the results related to the effect of $UO_2(NO_3)_2$ because the analyses are restricted to the growth phase and the maximal heat flow, where the addition of $Mg(NO_3)_2$ shows no effect.

In general, it is remarkable that the thermograms of JG-A12 and JG-B53 showed the similar pattern to those of the reference strain NCTC 9602. Unexpectedly, however, the results show that NCTC 9602 was less affected by uranium stress than the isolates. This indicates that NCTC 9602 is more tolerant to uranium stress than the isolates.

In summary, the response of strain JG-B53 toward uranyl in the investigated range of concentrations showed unexpected behavior in the range of 10 – 50 μM in the dependence of both maximal heat flow and the growth rate. The growth-retardation caused by the addition of uranyl was more pronounced than those in the other strains. On the other hand, the strains JG-

A12, JG-TB8 and NCTC 9602 showed similar responses toward the presence of uranyl, but JG-TB8 was the most sensitive to uranyl.

Concentrations lower than 10 μM were tested to further address the capacity of the strains to adapt to the presence of uranyl in a threshold-dependent manner. The growth behavior at low concentrations will also be important for later studies (Chapter 3), where the high radioactivity of ^{233}U requires reduced nuclide concentrations to allow bacterial growth.

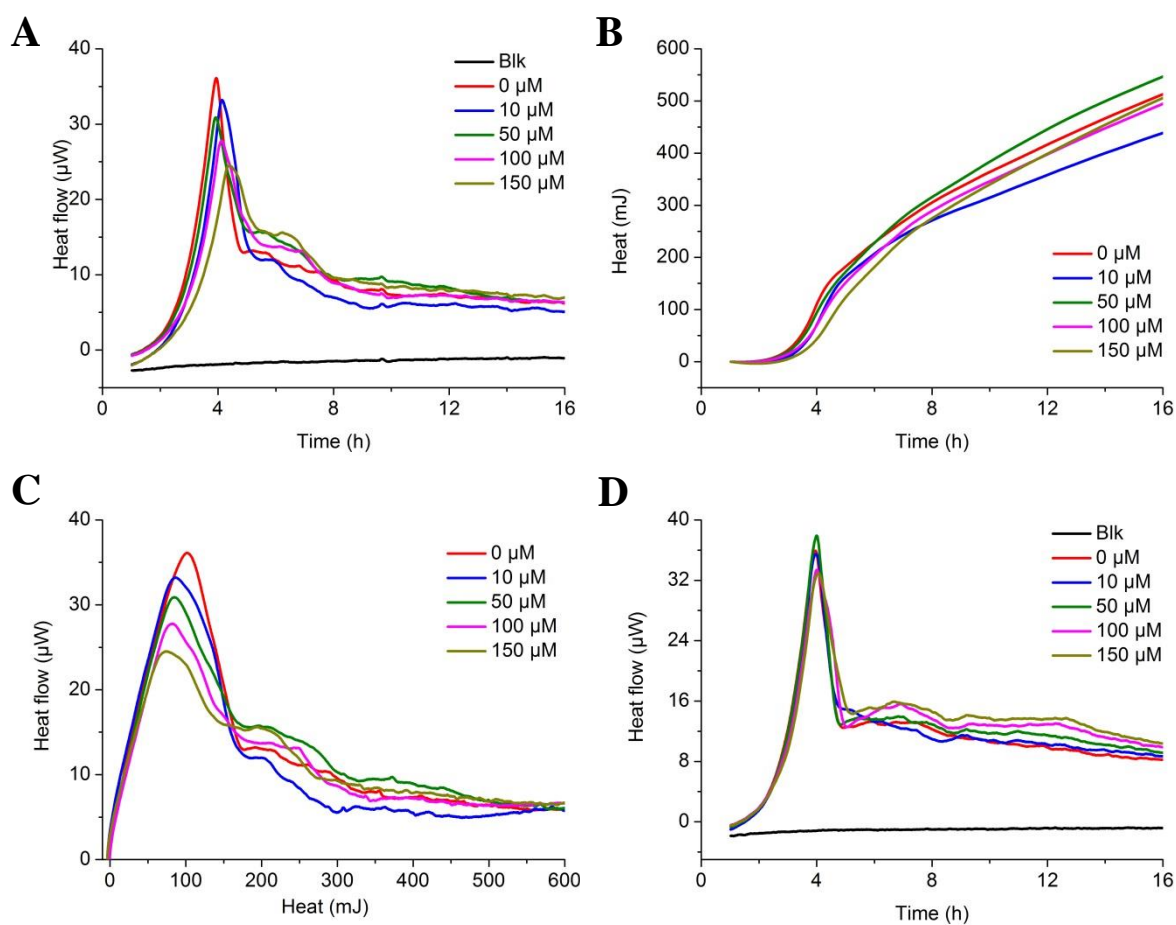


Figure 2-6: Effect of natural uranium on the metabolic heat flow of *Lysinibacillus sphaericus* NCTC 9602.

A: Heat flow is plotted vs. time. Bacteria were cultured at 30 $^{\circ}\text{C}$ in 2 ml 50% R2A medium. Natural uranium was added as $\text{UO}_2(\text{NO}_3)_2$ at the indicated final concentrations. B: Heat vs. time. C: Heat flow vs. heat. Regression lines were calculated for the linear segments of the plot. Growth rate constants for the phase of exponential growth were derived from the slopes (Table 2-6). The curves correspond to the average of duplicate.

Table 2-6. U_{nat} -dependent growth parameters of NCTC 9602; $T_{\text{max}}(\text{h})$, $P_{\text{max}}(\mu\text{W})$ and $k(\text{h}^{-1})$ together with percentage errors and the percentage inhibitory ratio of each of the three parameters.

$[U_{\text{nat}}]$ (μM)	T_{max} (h)	% Error of T_{max}	P_{max} (μW)	% Error of P_{max}	k (h^{-1})	R	$(I)_t$ (%)	$(I)_p$ (%)	$(I)_k$ (%)
0	3.53	1.08	34.28	1.92	1.392	0.998	0	0	0
0.1	3.47	1.34	33.81	3.07	1.336	0.998	-1.66	-1.36	-4.02
0.5	3.45	1.02	32.5	0.01	1.362	0.998	-2.28	-5.21	-2.21
1	3.6	1.98	32.94	1.5	1.393	0.999	2.23	-3.92	0.01
1.5	3.52	0.44	31.09	0.14	1.364	0.998	-0.27	-9.3	-2.05
0	4.86	2.01	29.64	9.57	1.318	0.999	0	0	0
2.22	5.28	2.46	26.13	9.54	1.381	0.999	8.7	-11.85	4.79
4.45	5.1	0.81	23.58	1.22	1.322	0.999	4.93	-20.45	0.35
13.35	5.16	1.83	27.09	4.86	1.204	0.999	6.27	-8.6	-8.62
0	3.95	0.44	36.18	0.87	1.401	0.997	0	0	0
10	4.13	0.08	33.21	4.79	1.412	0.998	4.76	-8.21	0.79
50	3.93	1.06	31.28	0.32	1.41	0.998	-0.53	-13.55	0.64
100	4.11	1.1	28.01	0.16	1.306	0.998	4.14	-22.57	-6.78
150	4.39	2.18	25.32	3.31	1.249	0.998	11.14	-30.03	-10.82

2.4.5 Investigation of the effect of U_{nat} at concentrations below 10 μM

The unexpected non-monotonous dependence of P_{max} and k on uranyl concentration for JG-B53 and JG-A12, respectively, as mentioned in section 3.4.2, was inspiring to explore the metabolic activities also below 10 μM uranyl. Therefore, the bacterial strains were tested in equivalent experiments with uranyl nitrate concentrations of (0.1 to 1.5 μM), and (2.22 to 13.35 μM) in the first and second data set, respectively. Thus, each bacterial strain was tested in total in three different sets of uranyl nitrate concentrations as summarized in tables 2-3 to 2-6. These experiments served to reveal the onset of detoxifying mechanisms which may not be activated at sub micro molar uranyl concentrations but may require a μM threshold above which metal resistance could increase.

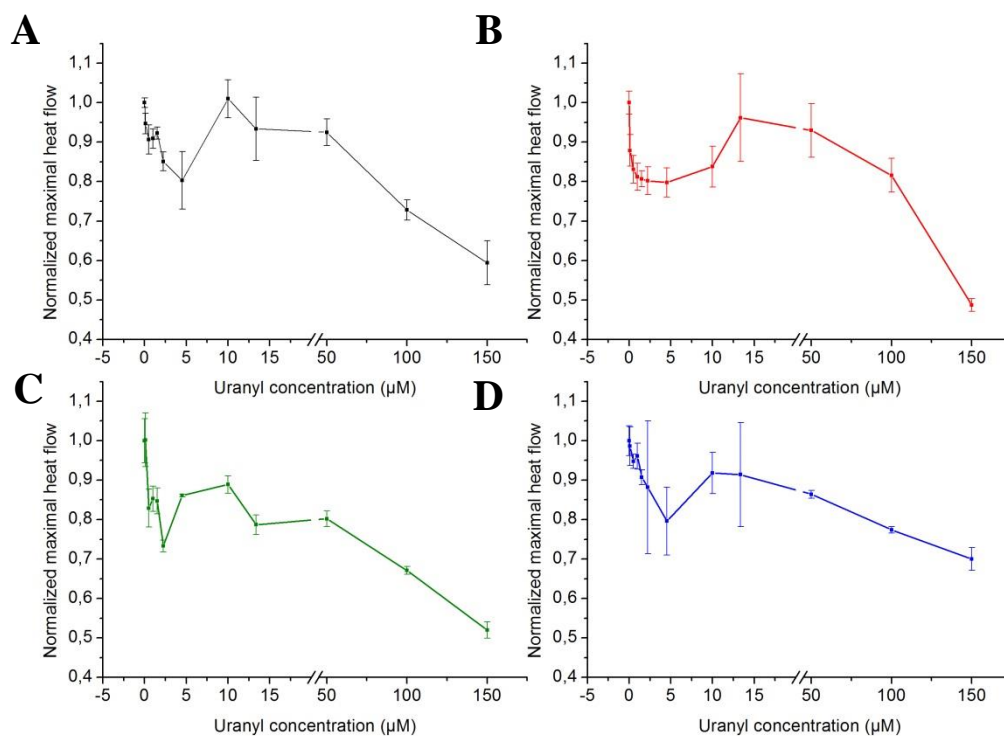


Figure 2-7: Normalized maximal heat flow vs. Uranyl concentration.

The P_{\max} at each uranium concentration was normalized by dividing it by the P_{\max} of the control sample (see tables 2-3 to 2-6) and the result was plotted versus uranium concentration for each bacterial strain: A: JG-A12, B: JG-B53, C: JG-TB8 and D: NCTC 9602. Data included in Table 2-7. This figure reveals the threshold concentrations at which the onset of the detoxification mechanisms is observed as an increase of P_{\max} with uranium concentrations.

Figure 2-7 shows four diagrams illustrating the normalized maximal heat flow *versus* uranyl nitrate concentrations for each of the investigated bacterial strains. Figure 2-7 (A) shows the diagram for JG-A12. P_{\max} was reduced by the increment of U_{nat} concentrations until 1 μM , increased again at 1.5 μM and reached a minimum at 4.45 μM . Unexpectedly, P_{\max} then increased and was maximal at 10 μM , before it declined again with increasing of U_{nat} concentrations. Figure 2-7 (B) shows the diagram related to JG-B53. The maximal heat flow was reduced successively by the increasing of U_{nat} concentrations until it reached a minimum at 4.45 μM followed by recovery of P_{\max} up to 13.35 μM uranyl before culture growth declined at higher U_{nat} concentration. The maximal heat flow values of JG-TB8 (Fig. 2-7 C) followed in general the same trend of JG-A12. It was reduced by U_{nat} concentrations up to 0.5 μM , but then it started to increase with uranyl concentration and peaked at 1.5 μM . Higher uranyl concentrations caused a reduction of P_{\max} , which became minimal at 2.22 μM . Again a recovery was observed, such that P_{\max} unexpectedly reached a peak at 10 μM , before it finally

decreased. Figure 2-7 (D) shows the diagram for NCTC 9602. The maximal heat flow followed the same pattern, it was initially reduced by U_{nat} at concentrations below 0.5 μM , after which P_{max} rose at 1 μM and dropped to a minimum again at 4.45 μM . Up to 10 μM uranyl P_{max} increased before finally declining at higher concentrations.

There was no necessity to investigate the effect of nitrate on the growth of the strains at these low concentrations, after it was found that the addition of nitrate in form of $\text{Mg}(\text{NO}_3)_2$ did not affect the growth under concentrations that are about 10 times higher than what is used in this case.

In summary, the isolates and the reference strain exhibited defense mechanisms against uranyl that are induced at $\sim 2 \mu\text{M}$ and $\sim 5 \mu\text{M}$, which allowed improved growth at 1-2 μM and 10-50 μM uranyl. Despite the similar uranyl sensitivity in all strains, the data show that the isolates exhibit better growth performance at concentrations close to 50 μM , i.e., after induction of a defense mechanism above the 10 μM threshold. In this narrow concentration range the isolates JG-A12 and JG-B53 show less uranyl sensitivity in their P_{max} value than the reference strain, whereas JG-TB8 is the most sensitive isolate and even less uranium tolerance than the reference strain.

2.4.6 Calibration experiments

Calibration experiments addressed the influence of initial cell numbers, nutrient supply and culture volume. These parameters significantly affect the thermograms and are crucial for the quantitative evaluation according to Eq. 2-7.

2.4.6.1 Different initial bacterial inoculations

Figure 2-8 Shows the thermograms of different inoculation volumes for JG-B53 and NCTC 9602, with the results included in tables 2-7 and 2-8 respectively. Similarly to what Katsutada Takahashi previously stated (Takahashi, 2000), thermograms in both strains showed retardation in reaching the maximal heat flow with decrement of the initial inoculation (represented by N_0), while they maintained approximately the same maximal heat flow value. These experiments allow calculating changes in the initial cell numbers between samples and controls that will be caused by the bactericidal effect of uranium isotopes of high α - activity, i.e, it would possible to relate the growth-retardation caused by a uranium isotope

(or with any other stressor) to the residual cell number that has survived a bactericidal effect and contributes to culture growth as under normal conditions (with no stressors).

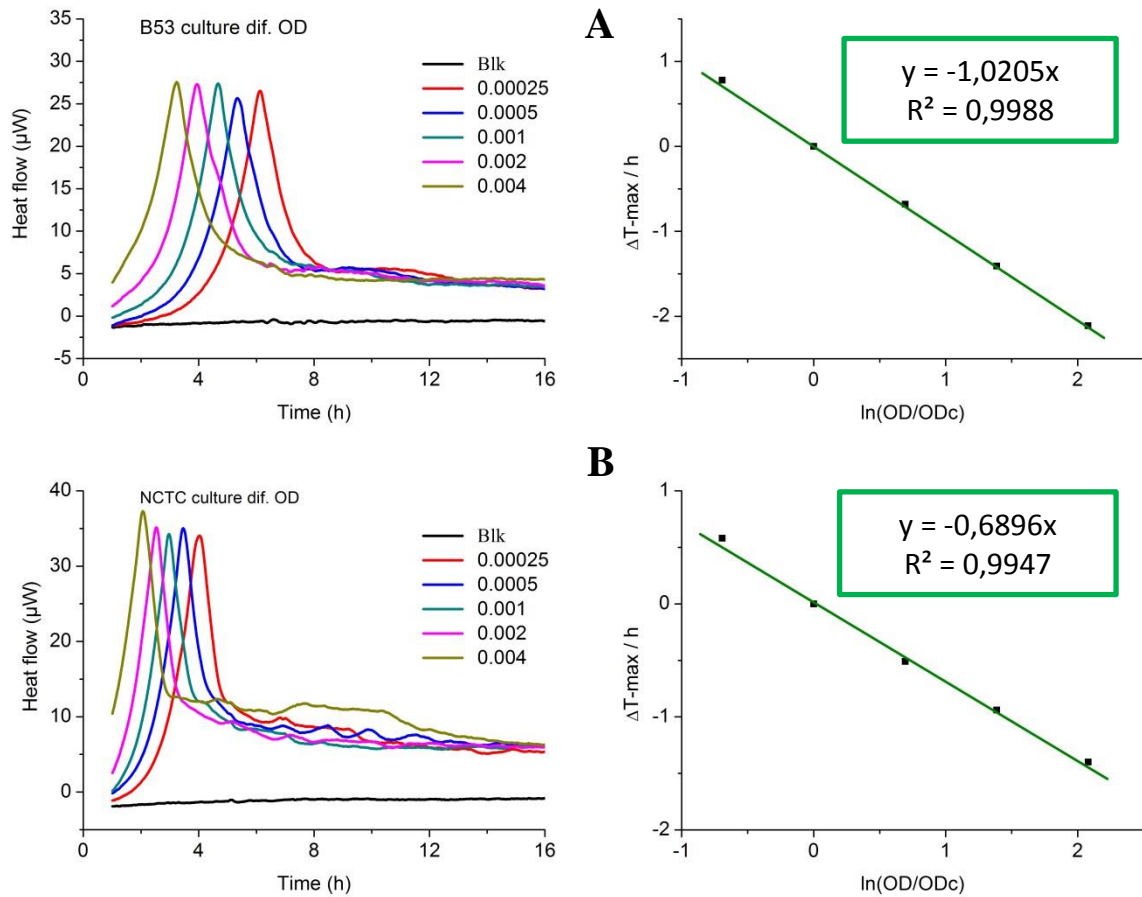


Figure 2-8: Calibration experiments for retardation vs. initial OD relation.

This figure shows the thermograms of A) JG-B53 and B) NCTC 9602 with different optical densities of the inoculations in 50 % R2A medium at 30 °C. It also show the linear relation between the retardation $\Delta T_{\max(i)}$ and the natural logarithm of the relative optical density $\ln\left(\frac{OD}{OD_c}\right)$.

Table 2-7. Different inoculation volume dependent growth parameters of JG-B53; $T_{\max}(h)$, $P_{\max}(\mu W)$ and $k(h^{-1})$ together with errors. $OD_c = 0.0005$.

OD	T_{\max}	P_{\max}	Err- T_{\max}	Err- P_{\max}	$k(h^{-1})$	R	$\ln(OD/OD_c)$
2.5E-4	6.13	26.7	0.037	0.328	1.07	0.999	-0.693
5E-4	5.35	25.93	0.044	0.285	1.09	0.999	0
1E-3	4.67	27.4	0.011	0.318	0.96	0.999	0.693
0.002	3.94	27.29	0	0	1.05	0.999	1.386
0.004	3.24	27.56	0.007	1.524	1.07	0.999	2.079

Table 2-8. Different inoculation volume dependent growth parameters of NCTC 9602; $T_{\max}(h)$, $P_{\max}(\mu W)$ and $k(h^{-1})$ together with errors. $OD_c = 0.0005$.

OD	T_{\max}	P_{\max}	Err- T_{\max}	Err- P_{\max}	$k(h^{-1})$	R	$\ln(OD/OD_c)$
2.5E-4	4.05	34.86	0.065	1.098	1.36	0.997	-0.693
5E-4	3.47	35.26	0.033	0.864	1.4	0.997	0
1E-3	2.96	34.25	0	0.589	1.5	0.995	0.693
0.002	2.53	35.66	0.044	1.494	1.45	0.996	1.386
0.004	2.07	37.33	0.018	0.426	1.23	0.998	2.079

Figures 2-8 (A) for JG-B53 and (B) for NCTC 9602 also show the expected linear relation between the retardation ($\Delta T_{\max(i)} = T_{\max(i)} - T_{\max(c)}$) and the natural logarithm of the relative optical density

($\ln\left(\frac{OD}{OD_c}\right)$), with $OD_c = 0.0005$ and $T_{\max(c)}$ is the time coordinate of the maximal heat flow for the sample that has the initial optical density OD_c . The formula of the linear fit for JG-B53 is:

$$\Delta T_{\max} = -1.0205 \cdot \ln\left(\frac{OD}{OD_c}\right) \quad (\text{Eq. 2-9})$$

Applying this formula to the experiments with uranium and taking into account that the OD is a measure of cell number; the formula can be rewritten as:

$$\Delta T_{\max(i)} = -1.0205 \cdot \ln\left(\frac{N_{0i}}{N_{0c}}\right) \quad (\text{Eq. 2-10})$$

With N_{0i} the number of viable initial cells survivors under uranium concentration (i) and N_{0c} initial cell number of cells in both the uranium-containing sample and control. Then N_{0i} can be calculated as following:

$$N_{0i} = N_{0c} \cdot e^{-\left(\frac{\Delta T_{\max(i)}}{1.0205}\right)} \quad (\text{Eq. 2-11})$$

Similarly, the equation related to strain NCTC 9602 is:

$$N_{0i} = N_{0c} \cdot e^{-\left(\frac{\Delta T_{\max(i)}}{0.6896}\right)} \quad (\text{Eq. 2-12})$$

From this equation the N_{0i}/N_{0c} for both strains JG-B53 and NCTC 9602 and the data are included in table 2-9.

Table 2-9. N_{0i}/N_{0c} ratio was calculated according to equations 2-11 and 2-12 for JG-B53 and NCTC 9602, respectively.

[Unat] (μM)	N_{0i}/N_{0c}	
	JG-B53	NCTC 9602
0	1	1
0.1	0.83	1.09
0.5	0.49	1.12
1	0.41	0.9
1.5	0.39	1.01
2.22	0.38	0.54
4.45	0.58	0.71
10	0.46	0.77
13.35	0.43	0.65
50	0.4	1.03
100	0.24	0.79
150	0.11	0.53

2.4.6.2 Experiments to calculate V_{eff}

It has been stated that cells form a sediment during growth in the calorimeter, thereby profiting from nutrients only within a small effective volume. Here this volume V_{eff} will be estimated by comparing growth in a sediment with that under floating conditions. Figure 2-9 shows the thermograms of (A) JG-B53 and (B) NCTC 9602 in 50 % R2A at 30 °C with stirring the medium inside the ampoule. It is clearly seen that for both strains the thermograms with stirring look different from those without stirring (Fig. 2-4 and 2-6 respectively), also the maximal heat flow in case of stirring is higher than those without stirring. The coordinates of the maximal heat flow for JG-B53 and NCTC 9602 were: (8.140 h, 131.846 μW) and (5.574 h, 137.179 μW), respectively. The effective volume was calculated using Eq. 2-8 for both strains: 0.424 ml for JG-B53 and 0.487 ml for NCTC 9602. Thus, only 20 - 25 % of the total culture medium is effectively used during growth in a resting ampoule.

The results agree with the assumption that the sedimentation of cells causes the apparent reduction of P_{max} as a consequence of the restriction of the bacteria to volume that is much smaller than the total volume of the ampoule.

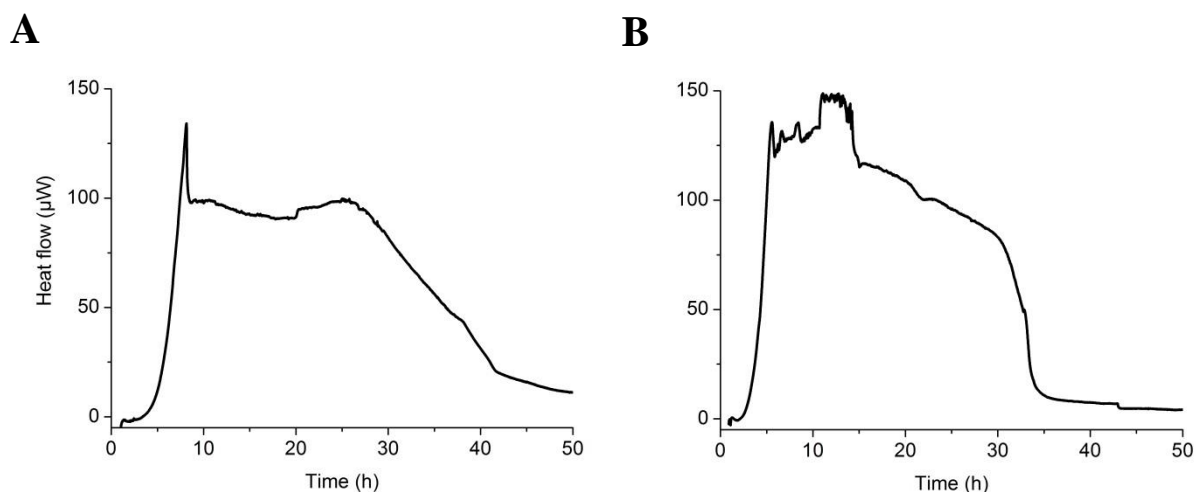


Figure 2-9: Isothermal microcalorimetry experiment with stirrer.

This figure shows the heat flow vs. time plots of A) JG-B53 and B) NCTC 9602 in 50 % R2A medium at 30 °C with stirring.

2.5 Discussion

In this study, the toxicity of natural uranium on the bacterial strains *Lysinibacillus sphaericus* JG-A12, JG-B53 and *Paenibacillus* JG-TB8, previously isolated from a uranium mining waste pile in Johann-Georgenstadt, Saxony, Germany, was quantified by deriving the growth parameters from the metabolic heat measurements of their culture growth under different concentrations of natural uranium in the form of uranyl nitrate $\text{UO}_2(\text{NO}_3)_2$. As a reference, similar experiments were performed with the reference strain *Lysinibacillus sphaericus* NCTC 9602 which is genetically related to the strains JG-A12 and JG-B53. These bacterial strains are Gram-positive, and have been shown to bind uranium to their surfaces layers (S-layers) by biosorption (Lederer et al., 2013; Merroun et al., 2005; Suhr et al., 2014), while the *Paenibacillus* JG-TB8 strain binds uranyl to the surface by bioaccumulation (Reitz, 2011) (see section 1-2).

The main goal of the study was to derive quantitative estimates of low doses toxicity by monitoring the metabolic activity using calorimetry. These estimates cannot be obtained with sufficient accuracy by classical methods such as turbidity measurements or colony counting. Instead, the obtained thermograms clearly show that the influence on metabolic activity can be measured directly at environmentally-relevant nuclide concentrations down to the sub-micro-molar range, where the resolution of other methods is much too low. In the following, the quantitative analysis of the thermograms will be discussed with the focus quantifying and understanding uranyl tolerance in the context of bacterial population dynamics. The latter

must be considered to be affected by both uranyl-induced cell death and uranyl-dependent metabolic effects on surviving cells. Both effects leave different traits in the thermograms. Initial cell death will mainly affect the retardation of culture growth, whereas metabolic interference will mainly affect the maximal heat flow and growth rates.

The study quantified the inhibitory action of 10, 50, 100 and 150 μM of $\text{UO}_2(\text{NO}_3)_2$ on the three waste pile isolates and the reference strain. The unexpected response of JG-B53 to 50 and 100 μM uranyl, i.e. the recovery of P_{max} at 50 μM vs. 10 μM uranyl, motivated the investigation of the inhibitory action at even lower uranyl concentrations in an attempt to find concentration thresholds, at which genetic detoxification mechanisms would be induced that caused gain in resistance against uranyl. Several parameters of the thermograms were derived to test which combination of them may be best suited to quantify toxicity or resistance. The bacterial metabolism was studied in the presence of uranyl nitrate from 0.1 to 150 μM and the parameters, T_{max} , P_{max} and k were determined to calculate the respective “inhibitory ratios” (see definition in section 2.3.2) as presented in tables 2-3 to 2-6. The analysis reveal two adaptive phases which will be discussed below.

2.5.1 Distinction of two adaptive regimes of uranyl-dependent bacterial growth

The addition of 0.5 to 1.5 μM U_{nat} to JG-A12 reduced the maximal heat flow by $\sim 8\%$ with a negligible retardation, but the growth rate was increased by $\sim 8\%$. This indicates that uranyl stimulated cell division but at the same time reduced the metabolic processes between replication, thereby leading to lower metabolic activity. The increment of uranyl concentration to 4.45 μM showed a growth-retardation by 3.6%, and a strong decrease in the maximal heat flow by $\sim 19.7\%$. Still, the prominent response of the cells to the heavy metal stress is increased replication by $\sim 7.31\%$.

This indicates that between 0 and 5 μM uranyl the cells show the same uranyl response, which will be designated adaptive phase (I). This phase is characterized by a higher replication at otherwise reduced metabolic activity, i.e. growth-retardation and earlier metabolic arrest leading to reduced P_{max} . 5 μM uranyl appears to be the threshold for the onset of a second adaptive phase II up to 10-13 μM when cells grow again without delay, little or no reduction in maximal metabolic activity but exhibit enhanced replication rate. In this concentration range, the results fluctuated but showed both $\sim 7\%$ retardation and growth rate fluctuation between ~ -13 and $\sim +10\%$. The culture was apparently in a non-uniform state regarding the induction of metal- defense mechanisms, such that phase (II) was induced in

some cases, leading to enhanced growth, whereas the adaptive mechanisms of the lower uranyl concentration regime in phase (I) were already at the limit of their effectiveness. They again feature increased replication, allowing recovery of maximal heat flow and onset of culture growth without delay in some cases. In the 50-150 μM range, however, the adaptive mechanisms are insufficient and the culture switches from the adaptive phase (II) to a purely uranyl-inhibited regime with decreasing growth rates and metabolic activities and increasing delay in growth. Eventually, the addition of 150 μM reduced and delayed the maximal heat flow by $\sim 40.6\%$ and $\sim 14.5\%$ respectively, and the growth rate was reduced by 20.31 %.

The defensive response exhibited by JG-A12 was also present in the other three strains. Generally, the dependence of the maximal heat flow on the uranyl concentration (Fig. 2-7) shows that all of the four *Bacillus* strains showed the same general pattern of metabolic heat production, i.e. the maximal heat flow was reduced by U_{nat} until it reached a minimum at 2-5 μM uranyl and then, unexpectedly increased again up to 10-50 μM U_{nat} before finally declining at higher concentrations. At 10-15 μM uranyl concentrations, i.e., near the switching point of phase (II), the growth parameters showed large error bars evidencing the metabolic reorientations and altered effectiveness of these defensive mechanisms. The resumption of metabolic activity above a threshold of 5 μM uranyl is a clear indication of an adaptational effect, i.e., gene expression is induced that leads to yet unknown detoxifying processes. All tested strains exhibit this adaptation. Since it is also seen with the reference strain NCTC, it is likely that general heavy metal detoxifying processes rather than uranyl-specific genes are involved. However, small differences among the diagrams might indicate that the uranyl sensitivity among the four strains differs slightly. The strains differ with respect to 1) the concentration at which the maximal heat flow gets depressed by uranium (the lower the concentration is the more sensitive is the strain to uranium), 2) the concentration where the maximal heat flow has reached a maximum (the higher the concentration is the more tolerant is the strain to uranium) and 3) the steepness of the decrease of the maximal heat flow with rising uranyl concentrations (the steeper the decrement the more sensitive is the strain to uranium). In this description, the strain JG-TB8 is the most sensitive followed by JG-B53, JG-A12 and finally comes NCTC 9602 as the least sensitive strain (or most tolerant strain) to uranyl-toxicity in this evaluation scheme. However, *Lysinibacillus sphaericus* isolates exhibited better performance than the reference strain at $\sim 50\ \mu\text{M}$ uranyl. Also only the isolates showed the recovery of growth in the 10 to 50 μM increase in uranyl. Therefore, the data suggest a genetic adaptation of the isolates in a narrow uranyl concentration window but no general advantage in uranyl tolerance over the reference. On the other hand, biomass in

the culture and binding capacity should be considered when comparing the sensitivity of the strains to uranium. JG-A12: ~ 94 mg uranium / g dry weight cells, JG-B53: ~163 mg mg/g, JG-TB8: ~ 138 mg/g and NCTC 9602: ~185 mg/g. These values were determined at pH 4.5 for JG-TB8 and pH 4 for other strains (Raff et al., 2006; Reitz, 2011; Suhr, 2015). The reason behind these differences in the binding capacity is related to the differences in cell membranes structure of these strains. In general, bacteria can rapidly adapt to the difficult conditions in their surrounding environment by different mechanisms including, but not only, changing their metabolism, gene modification, protein expression and surface modification (Lederer et al., 2013). The *Lysinibacillus sphaericus* strains NCTC 9602, JG-A12 and JG-B53 possess surface layer proteins (S-layer) (Fig. 2-10 A). These S-layer proteins self-assemble to form a porous lattice that represents the outermost layer of the cell surface (Fig 2-11), and covers the cell surface completely during all stages of bacterial growth and divisions. The S-layer functions as molecular sieve that provides the bacterial cells with a selective protective cover (Lederer et al., 2013; Merroun et al., 2005).

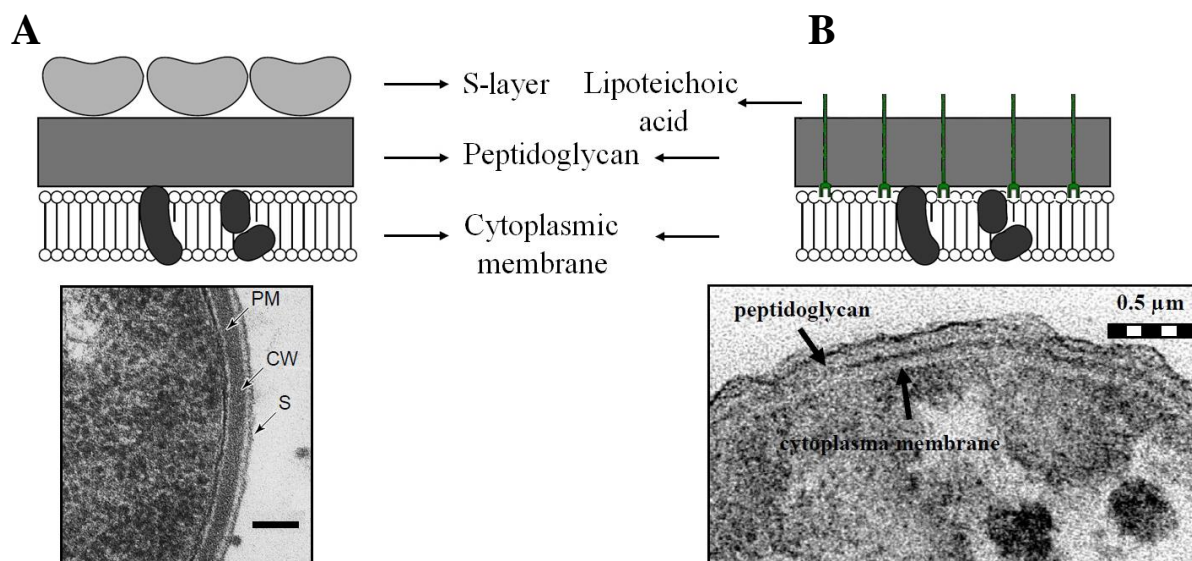


Figure 2-10: Comparison of the cell envelopes of A: *Lysinibacillus sphaericus* strains and B: *Paenibacillus*.

This figure shows the differences in the cellular membrane structure between: A) *Lysinibacillus sphaericus* strains and B) *Paenibacillus*. The figures were adapted from: A: (Sleytr and Beveridge, 1999) and B: (Reitz, 2011).

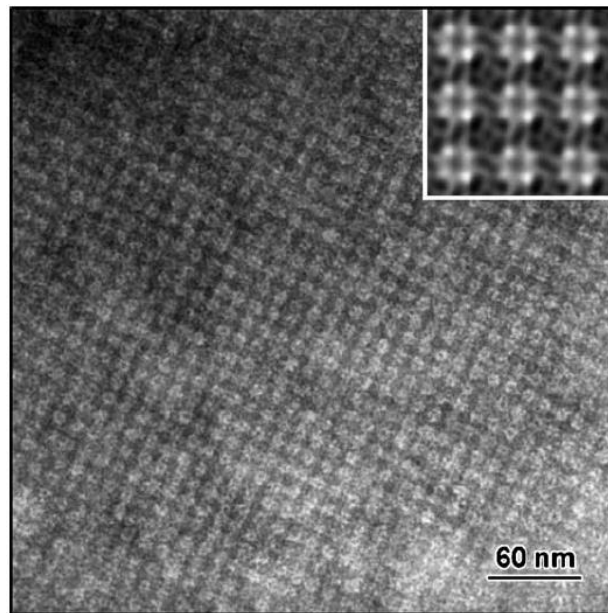


Figure 2-11: TEM micrograph of isolated S-layer of *Lysinibacillus sphaericus* JG-A12.

This figure shows the porous lattice covering the cell surface of JG-A12 that is formed by the self-assembled S-layer protein. This figure was adapted from (Pollmann et al., 2006).

When the S-layer becomes saturated with uranium this causes denaturation of the S-layer, leading to the production of new S-layer proteins to replace the older layer (Fig. 2-12). Thus, S-layer could protect the cell from uranium and other heavy metals (Merroun et al., 2005). Furthermore, because these three strains are related to the same species, their S-layer proteins are very similar to each other. The S-layer protein *slfB* of JG-A12 shows high similarity to the S-layer of the reference NCTC 9602 *slfA*, but the first one contains about six times more phosphorus than the latter (Merroun et al., 2005; Pollmann et al., 2005). On the other hand, the genome of JG-B53 encodes at least eight S-layer proteins with distinct differences. The S-layer gene *slp1* encodes B53 *slp1* the most abundant S-layer protein in JG-B53. This gene is 67 % identical to *slfB* (the gene of S-layer protein of JG-A12) and 65 % identical to *slfA* (the gene of S-layer protein of NCTC 9602) (Lederer et al., 2013). In the most recent study it was found that JG-B53 possesses 13 different S-layer genes, JG-A12 possesses 3 different S-layer genes and NCTC 9602 possesses 8 different S-layer genes (unpublished data of Dr. Franziska Lederer). The expression of these different genes may occur under stressful conditions (Kuen et al., 1997). The binding capacities of S-layer of the *Lysinibacillus sphaericus* strains are: JG-A12: 35.29 mg/g, JG-B53: 42.5 mg/g and NCTC 9602: 5.04 mg/g (Raff et al., 2005; Raff et al., 2006). Considering these values explains the results of having JG-B53 the most sensitive strain among the *L. sphaericus* strains and NCTC 9602 the least sensitive one. Nevertheless, it is not clear the reason behind that NCTC 9602

has the lowest binding capacity per S-layer but the highest binding capacity per cell, but the results obtained by the IMC are better explained by the binding capacities of the S-layer. In contrast, *Paenibacillus* JG-TB8 has a different cell membrane structure that does not include S-layer (Fig. 2-10 B), but it contains a thick layer of peptidoglycan that is rich with carboxylic and phosphate groups, which in turn serve as the dominant binding sites of heavy metals in the cell membrane (Reitz et al., 2008). These differences might be responsible to different response toward the toxicity of heavy metals (Lederer et al., 2013; Merroun et al., 2005).

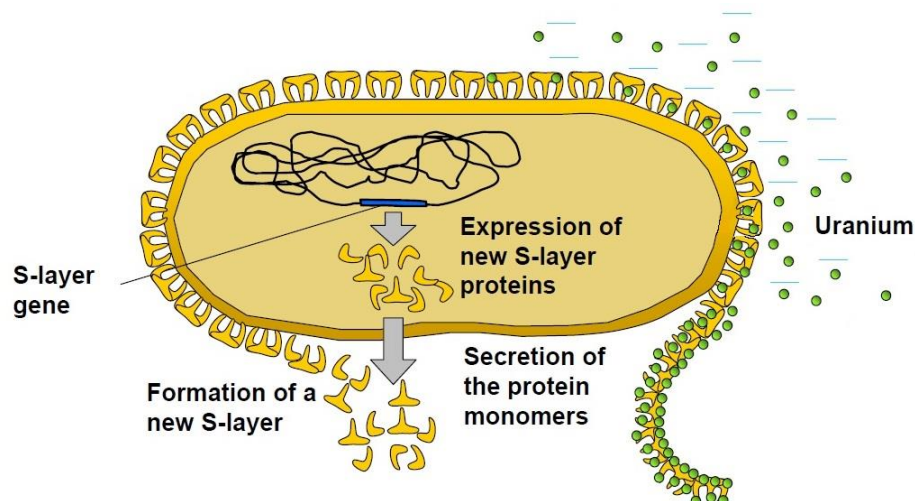


Figure 2-12: Release of the uranium saturated S-layers and synthesis of fresh protein.

This figure shows protection mechanism provided by the S-layer to the cell. The S-layer functions as molecular sieve against heavy metals. When the S-layer becomes saturated with uranium this causes denaturation of the S-layer, which will be replaced by freshly produced new S-layer proteins. This figure was adapted from (Raff, 2010).

2.6 Conclusions

It could be demonstrated here that microcalorimetry allows quantifying metabolic response of bacterial cultures to environmentally relevant low concentrations of uranium down to the μM range. This possibility was used to reveal subtle differences in uranyl sensitivity in three uranium waste pile isolates in comparison to a reference strain. Although the waste pile isolates did not show a distinctly improved growth resistance to uranium, the data clearly show that they all exhibit better growth parameters in the narrow window of uranium concentrations in the 10 to 50 μM regime. Different adaptational phases could be identified in the 0-5 and 10-50 μM range which lead to growth recovery when uranyl exceeds these concentrations thresholds. The extremely high sensitivity of the method as compared to turbidity measurements and colony counting allowed the detection of these features.

Novel research activities in the field of radioecology are currently emerging and addressing the question of transgenerational effects of radionuclides on species. The underlying concept envisages the comparison of identical naturally present species that have been exposed to radionuclides over long periods with individuals from ecologically equivalent uncontaminated sites. Here the investigation of the isolates provides a microbiological example for the ecological approach. The work shows the strength of metabolic activity measurements by calorimetry, because it can be performed quantitatively and, importantly, without previous knowledge on metabolic pathways. If the latter were required, ecological studies would have to be restricted to small number of well-defined model organisms. The experiments described here show that calorimetry does not face this restriction and will be a powerful tool in modern radioecology with the potential of providing quantitative risk assessments based on on-site test organisms.

Chapter 3

3 Comparison of radiotoxicity and chemitoxicity of uranium

3.1 Abstract

In this study, the radiotoxicity of uranium was quantified and distinguished from its chemitoxicity by microcalorimetric measurement the growth parameters of *Lysinibacillus sphaericus* JG-B53 in the presence of varying concentrations of ^{233}U and U_{nat} . As a reference, equivalent experiments were performed with *Lysinibacillus sphaericus* NCTC 9602, a well-defined strain that is related to JG-B53. As expected, the inhibitory action of ^{233}U was higher than the one of U_{nat} due to the higher specific radioactivity of ^{233}U in comparison to U_{nat} . The addition of ^{233}U showed clear bactericidal effects on JG-B53. The inhibitory action of ^{233}U in the range 0.5 to 1.5 μM was comparable with the inhibitory effect of U_{nat} in the 50 to 150 μM range observed with JG-B53 in chapter 2. Phenomenologically, this observation indicates that radiotoxicity is about 100 times greater than chemical toxicity in JG-B53 when the metabolic activity of the bacterial population as a whole is concerned. The reference strain NCTC 9602 showed less sensitivity toward both uranium isotopes in comparison to JG-B53.

3.2 Introduction

Due to the increased usage of uranium in different applications, many investigations have been performed in the recent decades to study the toxicity of uranium in animals (Bentley et al., 1985; Domingo et al., 1987; Domingo et al., 1989; Harvey et al., 1986; Llobet et al., 1991; Paternain et al., 1989), and fewer studies were performed in humans to take statistics from either the occupationally exposed workers, or from soldiers who were exposed to uranium in military conflicts (Clarkson and Kench, 1956; McClain et al., 2001; McDiarmid et al., 2000; Thun et al., 1985). However, these studies did not take into account the differentiation between radiotoxicity and chemitoxicity. Some research groups have used depleted uranium, which is less radioactive than natural uranium by about 40 %, in an attempt to study the chemical toxicity of uranium, but could not exclude that, even at this very low radioactivity, alpha particles might nevertheless have influenced their results (Domingo, 2001; Handley-Sidhu et al., 2010). There is still a lack of knowledge on the difference

between radio- and chemitoxicity of uranium. This distinction is particularly challenging at low doses, where lethality-based assays cannot be used with high accuracy. It is a major task of the present work to demonstrate that sensitive measurements of the metabolism of living organisms can provide a reliable and quantitative assessment of the different toxicities.

In order to identify the effect of radiotoxicity of uranium and to distinguish it from its chemical toxicity, the comparison between metabolic responses to the inhibitory actions of uranium isotopes that differ only in their specific activity is the most direct strategy. In this study, *Lysinibacillus sphaericus* JG-B53 (Lederer et al., 2013), and the related reference strain *Lysinibacillus sphaericus* NCTC 9602 (Pollmann et al., 2005), were exposed to different concentrations of uranium-233, which is an alpha emitter with energy ~ 5.4 MeV and a specific activity $A_0=3.566 \times 10^8$ Bq/g, and to natural uranium in the form of $\text{UO}_2(\text{NO}_3)_2$ in order to investigate and distinguish radiotoxicity from chemitoxicity of uranium. It was possible by microcalorimetry to monitor the metabolic activity of the bacterial culture in real time under the stress of the two uranium isotopes. The analysis of the thermograms was performed as in chapter 2. The growth parameters were extracted from the thermograms, and their inhibitory ratios (I) were calculated in order to express in percent to which degree each of the three determined growth parameters was affected by the respective isotope.

3.3 Material and methods

3.3.1 Bacterial culture and isothermal calorimetry

The bacterial strains *Lysinibacillus sphaericus* JG-B53 and *Lysinibacillus sphaericus* NCTC 9602 were exposed to different concentrations of uranium-233 and natural uranium in form of $\text{UO}_2(\text{NO}_3)_2$. Bacterial cultures were grown in 50% R2A medium containing, per liter, 0.25 g yeast extract, 0.25 g peptone, 0.25 g casamino acids, 0.25 g glucose, 0.25 g soluble starch, 0.15 g sodium pyruvate, 0.15 g K_2HPO_4 , and 0.025 g $\text{MgSO}_4 \times 7\text{H}_2\text{O}$. The mixture was autoclaved at 120 °C for 20 min. The Bacterial strains were freshly prepared before each experiment by growing them overnight in 50% R2A at 30 °C. For microcalorimetry experiments, autoclaved glass ampoules were filled with 1990 μL medium supplemented, as required, with $\text{UO}_2(\text{NO}_3)_2$ ($\text{U}_{\text{nat}} / {}^{233}\text{U}$) to final concentrations of 0 – 1.5 μM . The samples were inoculated with 10 μL of the appropriate bacterial culture, pre-adjusted to an OD_{600} of 0.1, resulting in final initial OD_{600} of 0.0005 at the start of microcalorimetric measurements in 2 ml final volume. In each experiment the samples were prepared in duplicates, two blank

samples that contained only medium were run in order to check the sterility of the medium for each experiment, and two samples that contained only medium with bacteria without any uranium were run as controls. Finally, the ampoules were sealed tightly and introduced into the calorimeter in two steps: at first the samples were lowered to the equilibration position, where they were kept for 15 min, after that they were further lowered to the measuring position, at that point the instrument took 45 min to be thermally stable, and then started acquiring real time data. There was no need to investigate the effect of the included nitrate on the growth of the strains, because the addition of nitrate (as $\text{Mg}(\text{NO}_3)_2$) did not affect the growth even at concentrations about 10 times higher than those used here (see chapter 2). Dose estimation (see table 3-1) and data analysis were performed as described in chapter 2.

Table 3-1. The radioactivities of U_{nat} and ^{233}U that were introduced to the samples, and the related roughly estimated self-absorbed dose for JG-B53 and NCTC 9602.

[U] per sample (μM)	U_{nat}			^{233}U		
	Activity (Bq/sample)	self-absorbed dose D (mGy/cell)		Activity (Bq/sample)	self-absorbed dose D (Gy/cell)	
		JG-B53	NCTC 9602		JG-B53	NCTC 9602
0.1	0.001	0.004	0.007	17	0.075	0.114
0.5	0.006	0.026	0.04	83	0.365	0.555
1	0.012	0.053	0.08	166	0.729	1.11
1.5	0.018	0.079	0.12	249	1.094	1.665
2.22	0.027	0.119	0.181	369	1.621	2.467
4.45	0.054	0.237	0.361	739	3.247	4.941
8.9	0.108	0.475	0.722	1479	6.499	9.889
13.35	0.161	0.707	1.076	2218	9.747	14.83

3.4 Results

3.4.1 Effect of the isotope ^{233}U on the metabolic activity of the strain JG-B53 and the reference strain NCTC 9602

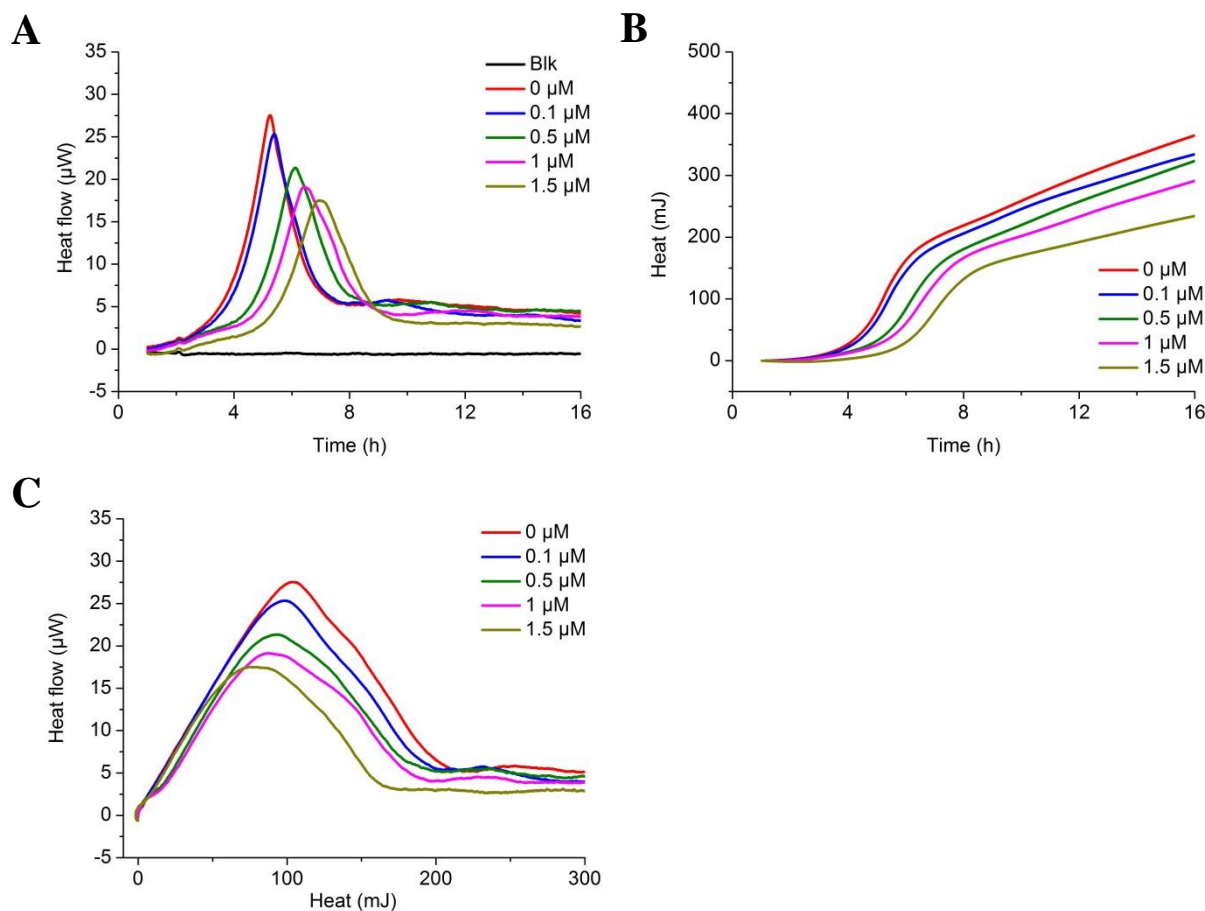


Figure 3-1: Effect of ^{233}U on the metabolic heat flow of *Lysinibacillus sphaericus* JG-B53.

A: Heat flow is plotted vs. time. Bacteria were cultured at 30 °C in 2 ml 50% R2A medium. ^{233}U was added as $\text{UO}_2(\text{NO}_3)_2$ at the indicated final concentrations. B: Heat vs. time. It approximates growth of the population in cell number. C: Heat flow vs. heat. It approximates the metabolic activity as a function of cell number. Regression lines were calculated for the linear segments of the plot. Growth rate constants for the phase of exponential growth were derived from the slopes (Table 3-2). The curves correspond to the averages of duplicates.

Figure 3-1 (A) shows thermograms for the growth of JG-B53 at various ^{233}U concentrations ranging from 0 to 1.5 μM . These curves are the average of duplicate experiments. After a short lag phase, the metabolic heat flow increased exponentially and reached its maximum after 5 to 7 h, then the signal declined and reached a stable level around 5 μM after 9 h. This indicates that after this time the culture is still alive but the nutrients are not sufficient for proliferation. The addition of ^{233}U caused the successive reduction and retardation of the thermogram peaks. The estimated activity and absorbed dose are included in

table 3-1. Already the addition of 1.5 μM ^{233}U reduced and delayed the maximal heat flow by $\sim 33.5\%$ and $\sim 33.3\%$ respectively. Integration of the heat flow leads to heat vs. time diagrams (Fig. 3-1 B). Assuming that the amount of heat produced during the formation of an individual bacterial cell stayed constant during the entire growth phase, the total heat scales with cell number during growth phase. Thus, the heat vs. time diagram approximates the increase in cell number during growth phase (Braissant et al., 2013; Bricheux et al., 2013). These curves showed that the addition of ^{233}U gradually decreased the total heat released by the cells. The quantitative analysis of the thermograms was restricted to the exponential growth phases. These phases appear as linear segments in the heat flow vs. heat shown in Fig. 3-1 C. Their slopes determine the underlying growth rates because both heat and heat flow are proportional to the cell number in the growth phases (Table 3-2). Surprisingly, the growth rate was little affected by ^{233}U in this low concentration range, despite the very distinct delay of the heat flow peaks with increasing isotope concentration. The latter is best appreciated by the inhibitory ratio I_t , which changes distinctly in dependence on uranyl concentration. The data indicate that radiotoxicity may predominantly affect the retardation and final cell density but not the duplication rate as will be discussed below.

Table 3-2. ^{233}U -dependent growth parameters $T_{\text{max}}(\text{h})$, $P_{\text{max}}(\mu\text{W})$ and $k(\text{h}^{-1})$ together with percentage errors and the percentage inhibitory ratio of each of the three parameters. Additionally, N_{0i}/N_{0c} ratio was calculated according to equations 2-11 and 2-12 for JG-B53 and NCTC 9602, respectively.

Strain	$[^{233}\text{U}]$ (μM)	T_{max} (h)	% Error of T_{max}	P_{max} (μW)	% Error of P_{max}	k (h^{-1})	R	$(I)_t$ %	$(I)_p$ %	$(I)_k$ %	N_{0i}/N_{0c}
JG-B53	0	5.24	0.14	27.54	2.27	1.047	0.999	0	0	0	1
	0.1	5.39	0.3	25.35	0.92	1.043	0.999	2.81	-7.95	-0.4	0.86
	0.5	6.11	0.31	21.35	0.16	1.037	0.999	16.56	-22.47	-1.04	0.43
	1	6.48	2.34	20.05	2.68	0.988	0.999	23.6	-27.2	-5.65	0.3
	1.5	6.99	2.62	18.32	1.78	1.029	0.999	33.29	-33.47	-1.73	0.18
NCTC 9602	0	3.65	1.35	34.88	0.08	1.36	0.998	0	0	0	1
	0.1	3.59	0.17	34.05	0.27	1.38	0.998	-1.64	-2.39	1.23	1.09
	0.5	3.71	2.35	32.61	5.26	1.42	0.998	1.71	-6.52	4.37	0.92
	1	3.92	1.8	33.09	0.82	1.39	0.998	7.36	-5.14	1.96	0.67
	1.5	3.81	1.43	30.09	3.86	1.38	0.998	4.27	-13.74	1.38	0.79

Experiments with higher concentrations (0, 2.22, 4.45, 8.9 and 13.35 μM) of ^{233}U were performed with strain JG-B53 (Fig. 3-2). The results were different from those with lower concentrations.

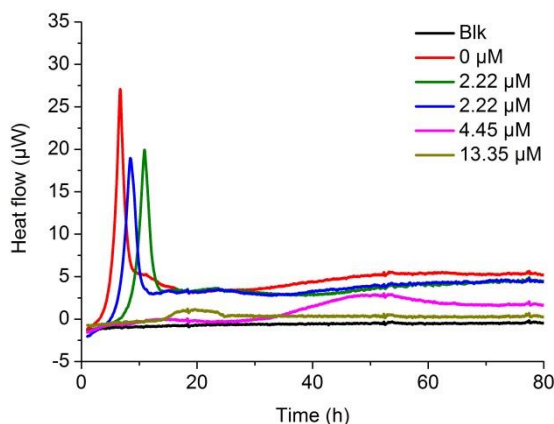


Figure 3-2: Effect of ^{233}U on the metabolic heat flow of *Lysinibacillus sphaericus* JG-B53. Heat flow is plotted vs. time. Bacteria were cultured at 30 °C in 2 ml 50% R2A medium. ^{233}U was added as $\text{UO}_2(\text{NO}_3)_2$ at the indicated final concentrations.

Remarkably, duplicate samples did not lead to identical results, except for the control (0 μM uranium). Figure 3-2 shows that the general shape of the thermograms was the same for both samples at 2.22 μM , but the growth in one of the samples was delayed with respect to the other one by ~ 2.5 h. At 4.45 μM one of the inoculates did not grow at all during the 80 h of measurements, while the other one grew very slowly and reached the maximal metabolic activity only after ~ 50 h. The samples of 8.9 μM did not grow at all during 80 h of measurements, and only one of the two samples containing 13.35 μM ^{233}U grew and exhibited a peak after ~ 18 h. The fluctuation in the data shows that at these concentrations, statistical survival effects have already become predominant. This can be expected for close to lethal doses for the culture as a whole, where the culture growth is initiated by only very few “survivors”, whereas the majority of the inoculated cells does not survive the exposure to the strong α -particle radiation or stays in a metabolically arrested state. Since the aim of this study was to investigate the effect of low doses of radiotoxicity at which cells are still alive, the effect of this set of high concentrations of ^{233}U was not further tested with NCTC 9602. Instead, only the low concentration range of ^{233}U was studied for this reference strain.

When NCTC 9602 was cultured in the 0 to 1.5 μM concentration range of ^{233}U , the heat flow vs. time curves showed that it is less sensitive to the uranium isotope-233 than JG-

B53 (Fig. 3-3 A). The thermograms of NCTC 9602 at varying concentrations of ^{233}U are almost synchronous, and less extended than those of JG-B53. Additionally, the maximal heat flow at $1\ \mu\text{M}$ ^{233}U was higher than the one at $0.5\ \mu\text{M}$. The heat vs. time plots show that the total heat released by the cells was approximately the same (Fig. 3-3 B). Figure 3-3 (C) shows the heat flow vs. heat plots of NCTC 9602 in the presence of ^{233}U . The virtually unaffected slopes of the linear segments show again that ^{233}U did not affect the growth rate k of NCTC 9602 in this concentration range, as k stayed almost constant $\sim 1.36\ \text{h}^{-1}$ (Table 3-2).

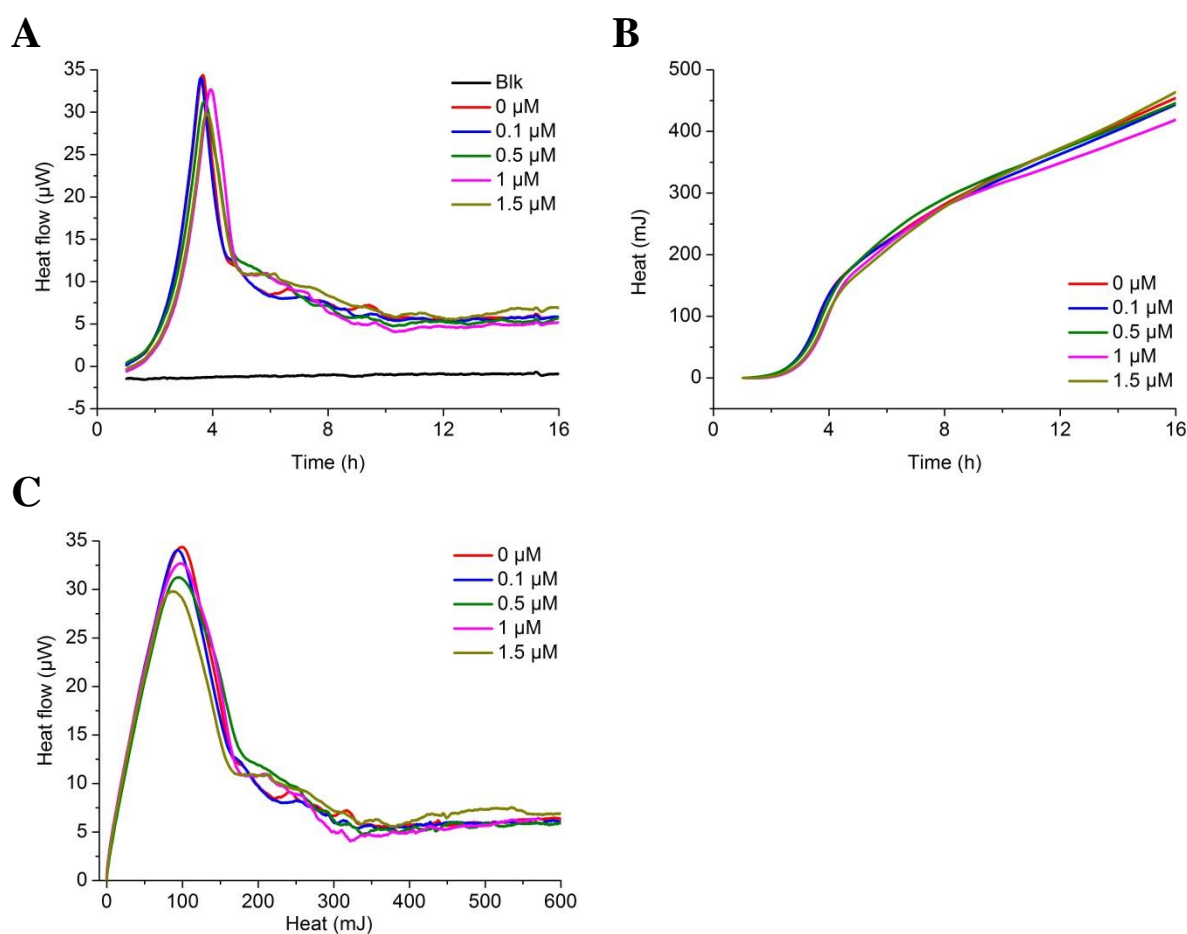


Figure 3-3: Effect of ^{233}U on the metabolic heat flow of *Lysinibacillus sphaericus* NCTC 9602.

A: Heat flow is plotted vs. time. Bacteria were cultured at $30\ ^\circ\text{C}$ in 2 ml 50% R2A medium. ^{233}U was added as $\text{UO}_2(\text{NO}_3)_2$ at the indicated final concentrations. B: Heat vs. time. It approximates growth of the population in cell number. C: Heat flow vs. heat. It approximates the metabolic activity as a function of cell number. Regression lines were calculated for the linear segments of the plot. Growth rate constants for the phase of exponential growth were derived from the slopes (Table 3-2). The curves correspond to the averages of duplicates.

In summary, ^{233}U concentrations above $2\ \mu\text{M}$ lead to dramatic reduction of cell survival and, consequently, to large fluctuations in the growth parameters. At lower doses, a reproducible growth behavior was observed and showed that the waste pile isolate JG-B53 is more sensitive to radiotoxicity than the reference strain. This sensitivity is best reflected in a prolonged retardation and reduced maximal metabolic activity, whereas cell division rates are not affected. The unexpected higher sensitivity of the waste pile isolate, which presumably had the chance to adapt to uranium stress, as compared to the reference strain may originate in the higher uranyl affinity of its S-layer. This could be advantageous in tolerating U_{nat} , where chemitoxicity is mostly concerned, but would be a disadvantage when high doses of α -particles become accumulated at the cell membrane.

3.4.2 Effect of the isotope U_{nat} on the isolated strain JG-B53 and the reference strain NCTC 9602:

To distinguish the effect of radiotoxicity from the effect of chemitoxicity of uranium, similar experiments to those described above for ^{233}U were performed with natural uranium at concentrations between 0 and $1.5\ \mu\text{M}$. These experiments extended the previously studied concentration range of U_{nat} (chapter 2) to the lower dose regime. Here, detoxifying chemical mechanisms are not present because the concentrations are still below the threshold for gene activation.

Figure 3-4 (A) shows the U_{nat} dependence of the thermograms of JG-B53. In comparison to ^{233}U (Fig. 3-1 A), U_{nat} has lower inhibitory effect than ^{233}U . In comparison to the control, the addition of $1.5\ \mu\text{M}$ U_{nat} reduced and delayed the maximal heat flow by $\sim 19\%$ and $\sim 16.5\%$ respectively. Figures 3-4 (B) and (C) show the heat vs. time and the heat flow vs. heat diagrams, respectively. The growth parameters and the inhibitory ratios are shown in Table 3-3.

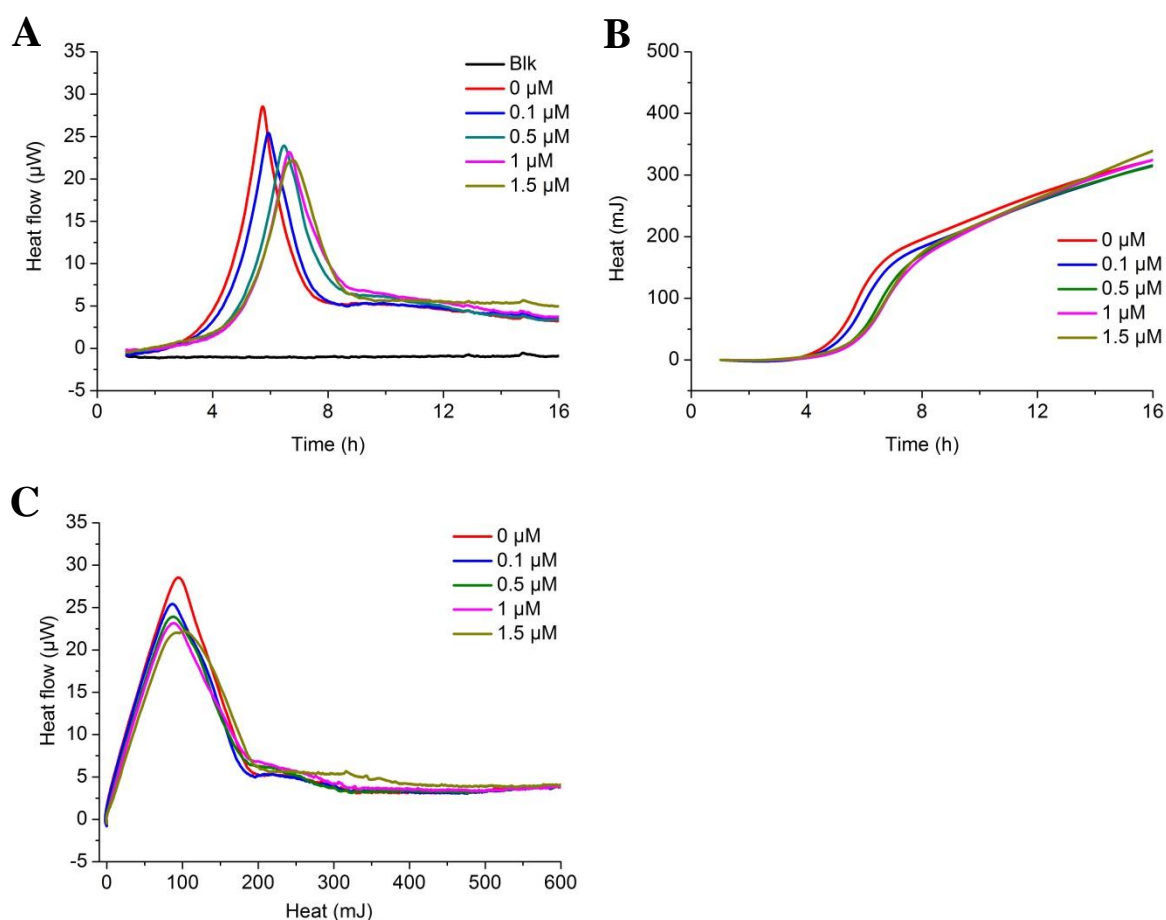


Figure 3-4: Effect of natural uranium on the metabolic heat flow of *Lysinibacillus sphaericus* JG-B53.

A: Heat flow is plotted vs. time. Bacteria were cultured at 30 °C in 2 ml 50% R2A medium. Natural uranium was added as $\text{UO}_2(\text{NO}_3)_2$ at the indicated final concentrations. B: Heat vs. time. It approximates growth of the population in cell number. C: Heat flow vs. heat. It approximates the metabolic activity as a function of cell number. Regression lines were calculated for the linear segments of the plot. Growth rate constants for the phase of exponential growth were derived from the slopes (Table 3-3). The curves correspond to the averages of duplicates.

The thermograms of NCTC 9602 under the same conditions are presented in Fig. 3-5 (A) and they are almost indistinguishable. They show again that NCTC 9602 is less sensitive toward U_{nat} than JG-B53 even at these low uranium concentrations. In general, however, the inhibitory effect of U_{nat} is less than that of ^{233}U . Figures 3-5 (B) and (C) show the heat vs. time and the heat flow vs. heat diagrams respectively, and the values of the growth parameters and the inhibitory ratios are summarized in Table 3-3.

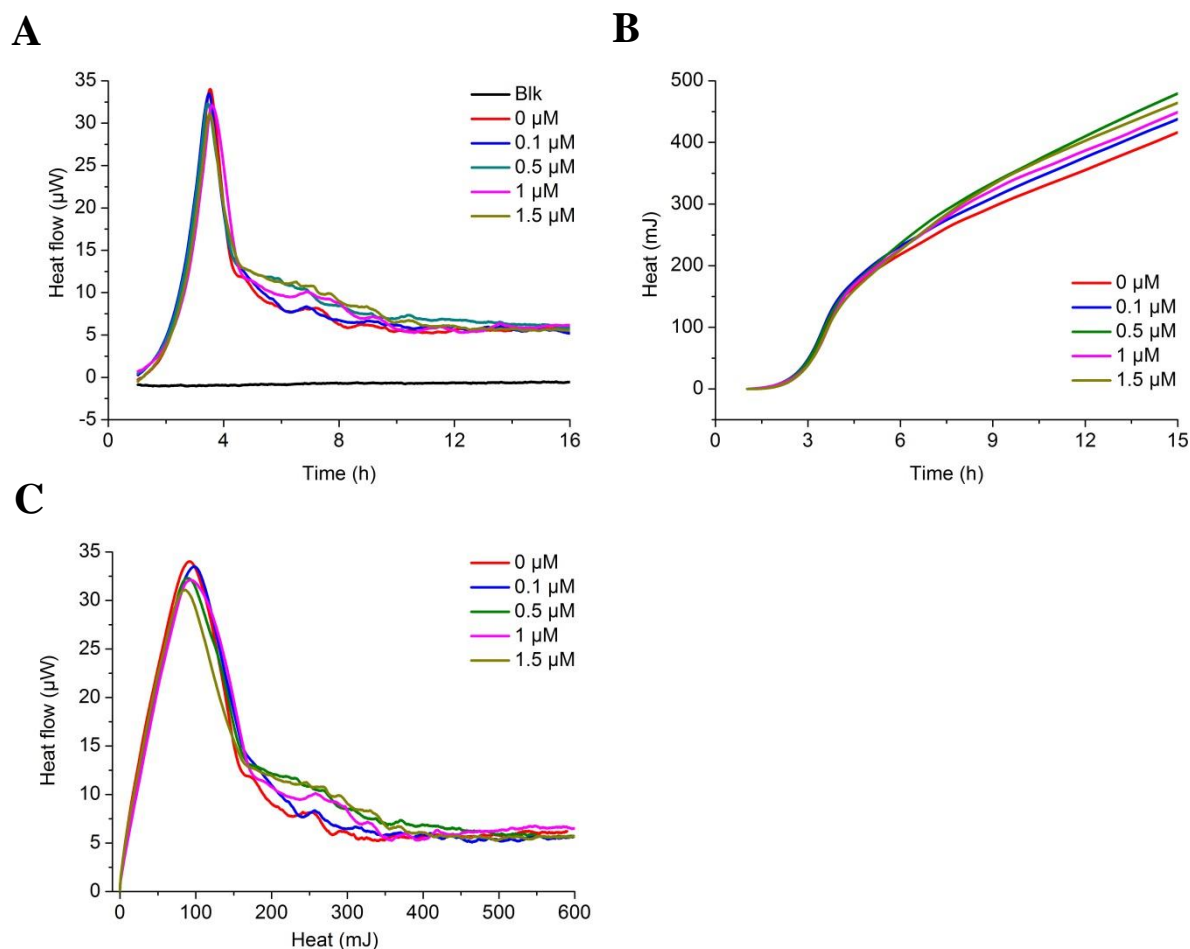


Figure 3-5: Effect of natural uranium on the metabolic heat flow of *Lysinibacillus sphaericus* NCTC 9602.

A: Heat flow is plotted vs. time. Bacteria were cultured at 30 °C in 2 ml 50% R2A medium. Natural uranium was added as $\text{UO}_2(\text{NO}_3)_2$ at the indicated final concentrations. B: Heat vs. time. It approximates growth of the population in cell number. C: Heat flow vs. heat. It approximates the metabolic activity as a function of cell number. Regression lines were calculated for the linear segments of the plot. Growth rate constants for the phase of exponential growth were derived from the slopes (Table 3-3). The curves correspond to the averages of duplicates.

In summary, radiotoxicity at very low doses is best quantified by growth delay (expressed by the inhibitory ratio I_t) and reduced maximal metabolic activity (expressed by the inhibitory ratio I_p), whereas growth rates are little affected. Using these parameters, the data show that, against expectation, the waste pile isolate JG-B53 is more sensitive to radiotoxic effects of ^{233}U than the reference strain NCTC 9602.

Table 3-3. U_{nat} -dependent growth parameters $T_{max}(h)$, $P_{max}(\mu W)$ and $k(h^{-1})$ together with percentage errors and the percentage inhibitory ratio of each of the three parameters. Additionally, N_{0i}/N_{0c} ratio was calculated according to equations 2-11 and 2-12 for JG-B53 and NCTC 9602, respectively.

Strain	$[U_{nat}]$ (μM)	T_{max} (h)	% Error of T_{max}	P_{max} (μW)	% Error of P_{max}	k (h^{-1})	R	$(I)_t$ (%)	$(I)_p$ (%)	$(I)_k$ (%)	N_{0i}/N_{0c}
JG-B53	0	5.74	0.83	29	1.45	1.123	0.998	0	0	0	1
	0.1	5.93	0.4	25.48	3.12	1.117	0.998	3.21	-12.12	-0.57	0.83
	0.5	6.47	0.85	24.11	2.74	1.128	0.999	12.68	-16.87	0.44	0.49
	1	6.64	1.13	23.54	2.74	1.077	0.999	15.65	-18.83	-4.08	0.41
	1.5	6.69	2.45	23.4	1.01	0.98	0.999	16.49	-19.29	-12.73	0.39
NCTC 9602	0	3.53	1.08	34.28	1.92	1.39	0.998	0	0	0	1
	0.1	3.47	1.34	33.81	3.07	1.34	0.998	-1.66	-1.36	-4.02	1.09
	0.5	3.45	1.02	32.5	0.01	1.36	0.998	-2.28	-5.21	-2.21	1.12
	1	3.6	1.98	32.94	1.5	1.39	0.999	2.23	-3.92	0.01	0.9
	1.5	3.52	0.44	31.09	0.14	1.36	0.998	-0.27	-9.3	-2.05	1.01

3.5 Discussion

In this study, the radiotoxicity of uranium was identified and distinguished from its chemical toxicity by measuring the growth parameters of JG-B53 under the stress of different concentrations of ^{233}U and U_{nat} . As a reference, similar experiments were performed with the well-characterized reference strain NCTC 9602. As expected, the inhibitory action of ^{233}U was higher than that of U_{nat} due to the higher radioactivity accompanied with ^{233}U in comparison to U_{nat} (Table 3-1). This distinction is mainly based on the inhibitory ratios I_t and I_p . Rationally, to identify the inhibitory action of radiotoxicity of uranium, the inhibitory action caused by U_{nat} should be subtracted from the inhibitory action caused by ^{233}U under the same concentrations. The difference between these two radioactive sources is related only to their radioactivity, which is in turn the origin of radiotoxicity.

However, before the radiotoxic and chemitoxic effects can be discussed, a potential source of error needs to be considered, i.e., the capability of many bacteria to activate defense mechanisms against toxic metals. The underlying proteins (e.g., heavy metal-exporting pumps) are usually expressed only above a concentration threshold of the respective metal (Dameron and Harrison, 1998). The induction of such detoxification mechanisms can be seen

in the thermograms as an increase of metabolic activity beyond a certain threshold concentration C_t of the metal. This leads to a situation that metabolic activities always decline with the addition of trace amounts of the toxic metal but recover again above C_t before declining monotonously when detoxification metabolisms are exhausted. Only this second phase of monotonous dependence of metabolic activity on metal concentration should be investigated to distinguish radio- and chemitoxicity, in order to avoid misinterpretations that are caused by different C_t among different bacterial strains. The following analyses have taken this into account. In chapter 2 it was found that C_t of $U_{nat} \sim 5 \mu\text{M}$ for both strains.

The addition of ^{233}U to JG-B53 has reduced the maximal heat flow successively down to $\sim 66.5\%$ at $1.5 \mu\text{M}$. This decrement in the maximal heat flow in comparison to the control means that (as discussed in chapter 2, section 2.3.5) either the metabolic heat flow per cell m has decreased by the addition of ^{233}U , which would be related to a bacteriostatic effect of ^{233}U , or the effective volume V_{eff} has changed due to the addition of ^{233}U . Although not intuitively clear, the effective volume defined in Eq. 2-7 (see section 2.3.5) is very crucial parameter in the mathematical analysis of thermograms under the condition of cell sedimentation in the ampoule. Remarkably, the growth rates were almost unaffected by ^{233}U . Therefore, it is unlikely that the reduced P_{max} originated in a change of m . Consequently, V_{eff} is the critical parameter that has changed as will be discussed below. Additionally, the retardation of the maximal heat flow (i.e., the onset of the exponential phase) was clearly prolonged with increasing radionuclide concentration (Table 3-2). This evidences bactericidal effect of ^{233}U by the reduction of the initial number of cells N_0 by increasing the addition of ^{233}U . The survival ratio N_{0i}/N_{0c} was calculated according to equations 2-11 and 2-12 for JG-B53 and NCTC 9602, respectively, and is included in tables 3-2 and 3-3 for both isotopes.

In summary, the bactericidal effect of ^{233}U is unambiguously demonstrated by delayed the onset of culture growth, due to the reduction of initial multipliable cells already at the beginning of the experiment. Unexpectedly, the remaining life cells then entered exponential growth at the same rate as the control, independently of the ^{233}U concentration and the preceding delay. Remarkably, the ^{233}U concentration affected the maximal metabolic activity of the cultures despite otherwise normal growth. A reduced metabolic activity is usually termed a bacteriostatic effect. However, a true bacteriostatic effect requires reduction of cell division rate and this was clearly not the case. All samples exhibited the same growth rate, only the length of the exponential phase shortened with increasing uranium concentration, thereby producing lower peak heat flow values. This discrepancy between an unaffected

growth rate and a reduced duration of exponential growth can be reconciled by the change in the effective volume V_{eff} , and the data are best described by the following model.

It is known that the S-layer of JG-B53 binds uranium. Thus, ^{233}U adsorbs to the cells of the inoculate. This will kill a certain number of cells in proportion to the amount of ^{233}U , and thereby explains the growth delay, because a smaller number of cells than the initial inoculate has to build up the total population. These survivors do not sense the uranium bound to the dead cells and, therefore, grow at a normal rate k as observed in the absence of uranium. However, ^{233}U stays bound to the dead organic material of the dead cells, and as ^{233}U decays the emitted alpha particles will be effective in a range about $50\ \mu\text{m}$ (the range of an alpha particle with energy $\sim 5.4\ \text{MeV}$ in water) (Contingencies, 2009). Therefore, the emitted alpha particles will form what can be called as “excluded volume” (V_{exc}) around non replicating cells with a radius of $50\ \mu\text{m}$ (Fig. 3-6). The remaining cells that have not interacted with the radionuclide grow normally in the virtual absence of the radionuclide. The uranium isotope stays of course part of the bacterial sediment in the calorimetric ampoules. Therefore, the radiotoxicity of this material will affect growth of the remaining cells only when they attain a density that brings them in close to physical contact to the excluded volume of the dead ^{233}U -bound cells. The more ^{233}U is present the higher the total excluded volume and the lower the required cell density.

This relation explains the decrease of P_{max} at constant k and m . It should be taken into consideration that the apparent size of the excluded volume is proportional to the radiated activity in the volume and to the exposure time of the cells when they temporarily reside in this volume. Additionally, the higher is the activity, the shorter the residence that is required to kill a cell in the volume. Therefore, it is difficult to calculate both although knowing one of them would make it possible to calculate the other one by using the results found by the thermograms.

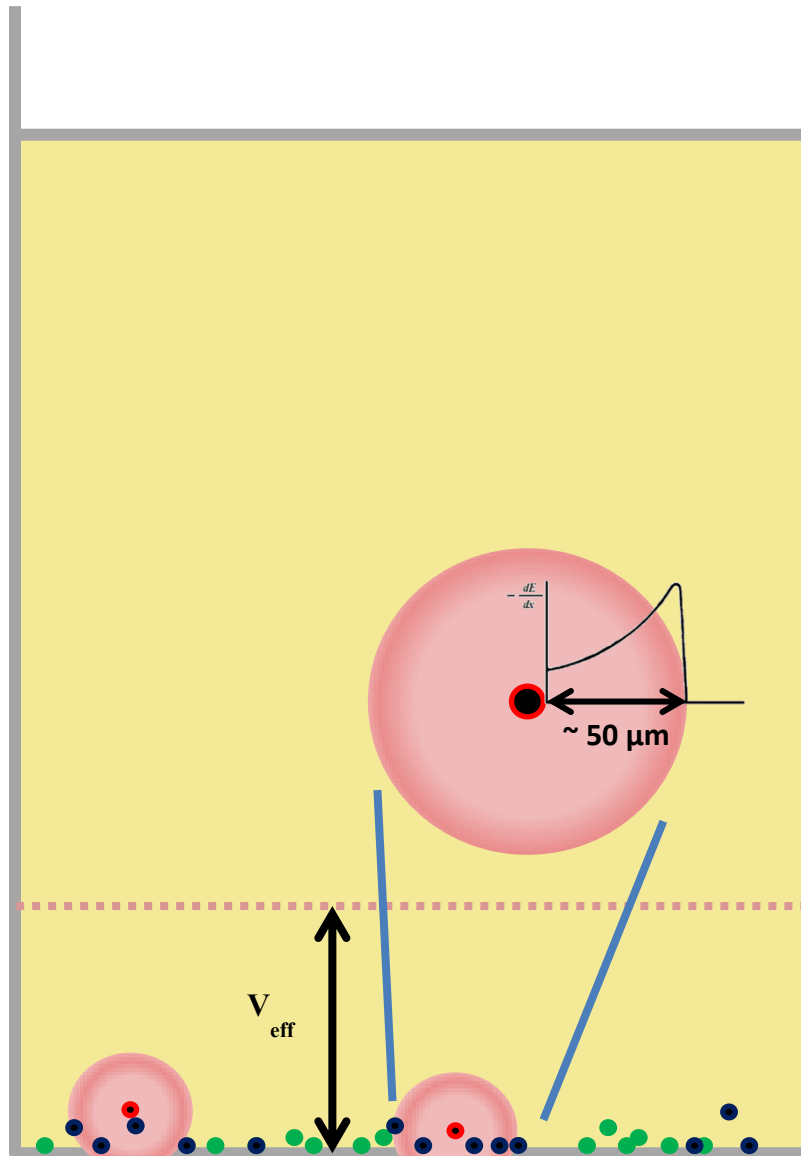


Figure 3-6: Radiation-induced excluded volume model.

This figure shows the formation of the excluded volume (the pink circles) around uranium-bound cells (black circles with red shells) by the emitted alpha particles, and how this excluded volume causes death to the cells that get inside it (black circles), while the cells that stay outside this volume stay alive and proliferate (green circles). This causes to decrease the effective volume, and consequently to a decrease in P_{\max} .

This model can explain both the successive reduction of the maximal heat flow (V_{eff} was reduced by V_{exc}) and the constant growth rate (survivor cells are not in reach of the α -particle path length in the bacterial sediment). Thus the predominant and probably the only effect of ^{233}U radiotoxicity is a bactericidal effect. This implies that a further increase of the ^{233}U concentration would also not cause a reduction of growth rate (bacteriostatic) but rather

decrease the number of survivor cells (bactericidal). This was indeed observed. Increasing the concentration of ^{233}U to higher values (2.22 – 13.35 μM) was lethal for the cells (Fig. 3-2). At 2.22 μM the delay between two identical samples can only be explained by the initial number of cells (N_0 (2.22 μM)) in the delayed sample (green color) being less than N_0 (2.22 μM) in the earlier sample (blue color). This means that ^{233}U was lethal for more cells in the delayed sample than in the other already at the beginning of the experiment, in agreement with the bactericidal effect of. Expectedly, the higher the concentration of ^{233}U , the more lethal it was to the cells. However, identical samples were differently affected, as at 4.45 μM or at 13.35 μM . Additionally, the number of survivals was irrelevant to the dose, as when the sample with 13.35 μM ^{233}U peaked ~ 30 h earlier than the sample with 4.45 μM , although its maximal heat flow was more inhibited. This random influence of ^{233}U at this range of concentrations can only be explained by the stochastic effect of radiation.

To estimate the radiotoxicity separately from the chemitoxicity the experiments that were conducted with ^{233}U were compared to equivalent experiments that were carried out with U_{nat} under the same concentrations. Figure 2-7 showed that the normalized maximal heat flow of JG-B53 was consecutively reduced by U_{nat} up to 4.5 μM U_{nat} . However, this reduction does not reflect the general chemitoxicity, because at this low chemical metal stress, the natural defense mechanisms are not yet induced. The latter reduce the metal sensitivity when they are activated above ~10 μM U_{nat} , as is evident from the higher metabolic heat values reached at 13.35 μM U_{nat} . From there on, chemitoxicity depends monotonously on U_{nat} as expected. Therefore, in order to distinguish and quantify radiotoxicity of uranium, the inhibitory effect of ^{233}U in the range 0.5 to 1.5 μM should be better compared to the inhibitory effect of U_{nat} at the highest concentrations of U_{nat} (i.e., range 50 to 150 μM) that would decrease the metabolic activity of the culture to the same extent as ^{233}U . The chemical toxicity of 50 – 150 μM U_{nat} is ~ 100 times greater than at 0.5 to 1.5 μM ^{233}U (Table 3-4). Again it must be emphasized that this statement refers to the bacterial population as a whole, not to an individual cell. Since comparable maximal heat flow values are observed under these two concentration regimes, one can conclude that the radiotoxicity of ^{233}U is about 100 times greater than the chemitoxicity of uranium in this situation. (The α -particle load at 0.5 to 1.5 μM ^{233}U is ~138 times higher than that at 50-150 μM U_{nat}).

Table 3-4. A comparison between the inhibitory ratios related to JG-B53 under the stress of 0.5 – 1.5 μM ^{233}U and 50 – 150 μM U_{nat} .

	(μM)	(I_t / %)	(I_p / %)	(I_k / %)
[^{233}U]	0.5	16.56	-22.47	-1.04
	1	23.6	-27.2	-5.65
	1.5	33.29	-33.47	-1.73
[U_{nat}]	50	18.16	-7.01	-12.79
	100	28.51	-18.41	-18.03
	150	44.69	-51.27	-46.81

The results from the waste pile isolate were compared with those of the reference strain NCTC 9602, which showed less sensitivity to both uranium isotopes in comparison to JG-B53. The thermograms in the very low regime of ^{233}U (0.5 to 1.5 μM) were almost indistinguishable from the control. Additionally, the maximal heat flow at 1 μM ^{233}U was higher than the one at 0.5 μM ^{233}U , which might indicate that, in this range of concentrations of ^{233}U , NCTC 9602 showed a defensive mechanism like the one that was observed in chapter 2 section. However, it should be noted that when ^{233}U was used, the defensive mechanisms were induced already at a concentration of 0.5 μM ^{233}U , i.e., at ~ 10 times lower concentration than the one needed for U_{nat} (4.45 μM). This indicates, that ^{233}U is not only more toxic than U_{nat} , but also appears to activate defensive mechanisms, probably through DNA repair mechanisms, because of its higher radioactivity (activity of 0.5 μM ^{233}U is 1844 times greater than the one of 4.45 μM U_{nat}). This observation leads to the conclusion that for NCTC 9602 the toxicity of ^{233}U is only ~ 10 times greater than the toxicity of U_{nat} at this low dose regime of concentrations. This surprising result can again be related to the properties of the bacterial S-layer as shown below.

3.6 Conclusions

As expected, the inhibitory action of ^{233}U was higher than the one of U_{nat} due to the higher radioactivity of ^{233}U in comparison to U_{nat} . The addition of ^{233}U showed a clear bactericidal effect on JG-B53 leading to a reduction of the initial number of reproducing cells. The inhibitory action of ^{233}U in the range 0.5 to 1.5 μM was compared to the inhibitory effect of U_{nat} in the range 50 to 150 μM to allow induction of protective mechanism observed with

JG-B53 (and other strains. See chapter 2). The radiotoxicity toward the bacterial population as a whole was about 100 times greater than chemical toxicity in JG-B53. Surprisingly, NCTC 9602 showed less sensitivity to both radioactive sources of uranium with radiotoxicity in the low dose regime being only 10 times higher than chemotoxicity.

A plausible conclusion for this observation could be the enhanced affinity of the S-layers of JG B53 for uranium in comparison to those for S-layer of NCTC 9602. It has been reported that the binding capacity of the S-layer of JG-B53 is 8 fold higher than for NCTC 9602 (Raff et al., 2005; Raff et al., 2006). This higher binding capacity may be a defensive mechanism of the waste pile isolate such that growth at 50 μM U_{nat} can be enhanced vs. 10 μM U_{nat} (Fig. 2-4), presumably by production and peeling off of U_{nat} -enriched S-layers (Merroun et al., 2005). However, with ^{233}U , the same mechanism may become disadvantageous, due to the accumulated α -particle density in the S-layer. Here, a low U-affinity would be advantageous which can explain the better growth of the reference strain, whose S-layer has been shown to exhibit lower U-affinity. If the waste pile isolate has evolved specific defense mechanisms against uranium, the data show that the selection was exclusively for chemotoxicity, but not for radiotoxicity.

Chapter 4

4 Copper and uranyl toxicity in *Lactococcus lactis* regulated by intracellular glutathione

4.1 Abstract

In this study, the role of intracellular glutathione (GSH), which plays an important protective role against the damage caused by reactive oxygen species (ROS), was investigated in order to show whether or not it is also involved in the detoxification of uranium. For this purpose, *Lactococcus lactis*, which exhibits a fermenting metabolism in the absence of heme even during aerated growth, was used as a model organism. This physiological trait allows study of detoxification mechanisms in the absence of ROS, which is important for coping with redox-active actinides. By microcalorimetric measurements of the metabolic heat of bacterial cultures it was shown that intracellular GSH, produced by nisin-induction in the *L. lactis* strain, attenuates the toxicity of uranium at a concentration in the range of 10-150 μM . In order to provide mechanistic information on uranyl toxicity, similar experiments were performed with copper, for which the intracellular toxicity has been extensively characterized, and were compared with those of uranyl. In contrast to uranyl, no effect on bacterial growth was observed with copper up to 100 μM concentration. Furthermore, copper toxicity was enhanced by GSH at elevated metal concentration which agrees with GSH-mediated metal-Cu-exchange in enzymes *via* sulfhydryl-bound copper. The data indicate that uranyl inhibits enzymes that are specifically expressed during late logarithmic growth. Isothermal titration calorimetry reveals the endothermic binding of U(VI) to the carboxyl group(s) of GSH, rather than to the reducing thiol group. The data indicate that the primary detoxifying mechanism is the intracellular sequestration of carboxyl-coordinated U(VI) into an insoluble complex with GSH. The adverse effect of GSH on uranyl toxicity in comparison to its effect on copper toxicity can be related to the difference in coordination chemistry of the respective metal-GSH complexes, which cause distinct effects on enzyme metal interactions.

4.2 Introduction

The natural abundance of uranium and the increasing health risks that originate from its anthropogenic release to the environment have generated a high demand for understanding the molecular mechanisms of uranium toxicity. Uranium can exhibit both, radiotoxic and chemitoxic effects on organisms. However, chemitoxicity of uranium is environmentally much more relevant (Miller et al., 2002). It is mostly caused by the displacement of Ca^{2+} and Mg^{2+} from their functionally important binding sites in enzymes (Nieboer and Richardson, 1980) and may exhibit high affinities to certain serum proteins in humans (Basset et al., 2013; Vidaud et al., 2005). Additionally, a Fenton-like uranyl-catalyzed reactions, leading to hydroxyl radical formation and consequently to cell damage by the formation of other reactive ROS, has been reported (Miller et al., 2002). However, uranium speciation plays a key role in the bioavailability of uranium (Ebbs et al., 1998; Markich, 2002), and consequently alters its toxicity. The water-soluble uranyl cation UO_2^{2+} is the most commonly found contaminant, which contains uranium in its highest oxidation state U(VI) (Cothorn and Lappenbusch, 1983; Duff et al., 1997; Valsami-Jones and Ragnarsdottir, 1997). Bacteria in the environment can actively participate in uranium speciation as exemplified by species of *Clostridia* and *Desulfovibrio*, which were shown to convert U(VI) to insoluble U(IV) species (Gao and Francis, 2008; Robinson et al., 1998). On the other hand, the impact of other redox-active heavy metals, such as copper or iron, on cell physiology has often been related to their ability to catalyze Fenton-type reactions. Considering that the current level of understanding of copper toxicity in bacteria appears to be more detailed than for any other heavy metal, this renders copper toxicity a suitable reference system for the study of other mechanisms of heavy metal toxicity. Therefore, it can be speculated that uranyl toxicity may have similar causes and, consequently, can be coped with by the detoxification processes described for other redox-active heavy metals.

It has been shown that the majority of copper-mediated oxidative stress in *E. coli* is located in the periplasm away from the DNA oxidative damage (Macomber et al., 2007), and that copper excess leads to the displacement iron from important Fe-enzymes (Chillappagari et al., 2010; Macomber and Imlay, 2009). This raises questions about the applicability of the well-established *in vitro* Fenton redox-processes of aqueous copper to the physiological regime. Additionally, intracellular copper, which appears to always be in the Cu(I) form, can bind to sulfhydryl-bearing proteins, amino acids, and small molecules like glutathione (GSH)(Chillappagari et al., 2010; Macomber and Imlay, 2009; Macomber et al., 2007).

Indeed, the toxicity of Cd^{2+} , which is not redox-active and can thus not catalyze Fenton-type reactions, appears to proceed by the same route of binding to important sulfhydryl groups and displacing metal cofactors, as exemplified by the up-regulation of cysteine and iron-sulfur cluster biosynthesis upon cadmium exposure (Helbig et al., 2008). On the other hand, the copper-homeostatic machinery, which pumps excess copper out of the cell, as well as chelation by GSH have been shown to protect against oxidative and acid stress, and against toxicity of arsenite and other heavy metal ions (Fu et al., 2006; Latinwo et al., 1998; Li et al., 2003; Zhang et al., 2007), besides copper (Macomber et al., 2007). With the copper homeostatic systems, the intracellular concentration of purely water-coordinated copper remains vanishingly small. For *Escherichia coli* it has been estimated to be in the zeptomolar (10^{-21} M) range (Changela et al., 2003).

GSH is an abundant non-protein thiol-bearing molecule in many organisms (Penninckx and Elskens, 1993). It is found in a restricted number of bacteria (Fahey et al., 1978) in which it can either be synthesized or taken up from the medium. *E. coli* cells, in which the GSH biosynthetic pathway was inactivated, were considerably more sensitive to killing by copper (Grosse et al., 2014). Similarly, when *Streptococcus pneumoniae* was allowed to take up GSH from the environment, it became more resistant not only to copper, but also to the non-redox-active heavy metals cadmium, and zinc (Potter et al., 2012). The latter observations hint at additional GSH-dependent detoxification processes that are not linked to oxidative stress.

In the context of the involvement of GSH in the detoxification mechanisms of both redox-active and redox-inactive heavy metals it is particularly challenging also for uranium to separate a potential oxidative stress response from other pathways of toxicity and corresponding defense mechanisms. Like copper, uranyl may interfere with natural metal-binding sites of enzymes, but the molecular mechanism of uranyl toxicity is expected to be more complex because uranium possesses four oxidation states, U(III), U(IV), U(V), and U(VI), and multiple coordination structures that lead to a variety of pH and ion-dependent speciations. GSH-dependent detoxification mechanisms that are effective against other heavy metals may also function for uranium. Toxicity of uranium has been linked to the induction of redox-imbances and oxidative stress as deduced from effects on intracellular GSH levels and lipid peroxidation in the tissues of different model plants, such as *Phaseolus vulgaris* and *Arabidopsis thaliana* (Vandenhove et al., 2006; Vanhoudt et al., 2008). It has been shown that uranyl affects the level of both GSH and its oxidized form, GSSG, in cultured cells from plants (Viehweger et al., 2011) and animals (Pourahmad et al., 2006). In the plant cells, U(VI)

shifted the redox potential to more oxidative or more reductive conditions at low (10 μM) and high (50 μM) uranyl concentrations, respectively (Viehweger et al., 2011). The rise of the total glutathione pool in the presence of low uranyl concentrations would agree with the generation of oxidative stress. GSH may catalyze the reduction of intracellular uranyl to insoluble species (U(V) or U(IV)) and thereby detoxify it (Viehweger et al., 2011). However, neither the effect of uranyl on GSH levels is uniform among the tested model organisms and cell cultures nor does the GSH level varies uniformly with the uranyl concentration within a given system. The complexity of these results hints at a protective role of GSH against uranyl toxicity that is not related to oxidative stress. To specifically address detoxification mechanisms that are independent of ROS formation, a system in which (1) oxidative stress can be excluded even in the presence of oxygen and (2) intracellular GSH can be controlled is needed. In such a system, a putative function of GSH in uranium detoxification can be studied without interference with oxidative stress responses.

For this purpose, the impact of varying intracellular GSH levels was investigated by using a genetically engineered strain of the gram-positive bacterium *Lactococcus lactis* subsp. *cremoris* NZ9000(pNZ3203). In this strain, the two GSH synthetic enzymes, γ -glutamylcysteine synthase and GSH synthase, are under the control of a nisin-inducible promoter (Fu et al., 2006; Li et al., 2005). Furthermore, ROS are not produced in this bacterium, which performs fermentation even in the presence of oxygen if heme is not present during aerated growth (Duwat et al., 2001). A low-dose regime of uranyl was considered the most relevant for the present studies with respect to radioecology, but it is also the most difficult to assess. Under such conditions, cell viability is typically little affected and cannot be used as an indicator. Therefore, isothermal microcalorimeter (IMC) was used as an extremely sensitive tool to study the metabolic activity and growth of bacteria (Braissant et al., 2010b). IMC allows measuring in real-time the metabolic heat released by *L. lactis* cultures in the presence of uranyl nitrate $\text{UO}_2(\text{NO}_3)_2$ in a concentration range of 10-150 μM . The metabolic signatures exhibited by the uranyl-exposed cells differed from those of copper-exposed cells, which suggest that copper and uranyl have different cellular targets. The toxicity of the two metals was also differently affected by GSH. Copper toxicity was enhanced by GSH which agrees with that copper interferes with iron-binding sulfhydryl-containing enzymes. In contrast to copper, the chemitoxicity of U(VI) was lowered by the intracellular production of GSH, which is probably the result of sequestration of uranyl in an

insoluble complex. Thus, GSH can enhance uranyl tolerance even under conditions that do not permit ROS formation.

4.3 Materials and methods

4.3.1 Bacterial culture and isothermal microcalorimetry

The strain NZ9000-pNZ3203 of *Lactococcus lactis* subsp. *cremoris* was obtained from NIZO food research B.V., The Netherlands. The strain NZ9000(pNZ3203) carries a plasmid with the *gshA* and *gshB* genes under the control of the *nisA* promoter, rendering the expression of the two genes inducible by nisin. Bacteria were grown at pH 7.2 in M17-G medium containing, per liter, 5 g Neopeptone, 5 g Bacto Soyton, 5 g beef extract, 2.5 g yeast extract, 0.5 g ascorbic acid, 1 g Na₂-β-glycerolphosphate x 5 H₂O. The mixture was autoclaved and supplemented with the following sterile solutions: 1 ml of 1 M MgSO₄ and 20 ml of 50% glucose. For microcalorimetry experiments, 52 ml of M17 medium were supplemented with 520 μl of 1 M Na-ascorbate and 130 μl of 200 mM cysteine in 100 mM HCl. For induction of GSH synthesis, 195 μl of 0.15 mM nisin were also added. Microcalorimetric ampoules were filled with 4 ml of medium and then supplemented, as required, with CuSO₄ or UO₂(NO₃)₂ to final concentrations of 100-800 μM and 10-150 μM, respectively. Finally, the samples were inoculated with 20 μL of the appropriate bacterial culture, adjusted to an OD₆₀₀ of 0.1, resulting in an initial OD₆₀₀ of 0.0005 at the start of microcalorimetric measurements. Isothermal microcalorimetry was performed with a TAMIII instrument (Waters GmbH, Eschborn, Germany) equipped with 12 channels to monitor continuously the metabolic heat flow produced by the bacterial cultures at 30 °C for up to 80 h.

4.3.2 Isothermal titration calorimetry of GSH uranyl complex formation

Isothermal titration calorimetry experiment (ITC) was performed to gain information about GSH-uranium binding interaction. Firstly, stock solutions of (A) 10 ml of 5 mM UO₂(NO₃)₂ in 0.1 M KNO₃ with pH=3.5, and (B) 5 ml of 200 mM GSH in 0.1 M KNO₃ with pH=3.5. In a 1 ml ITC-ampoule 0.8 ml of (A) were inserted, while water was used for the reference ampoule. 0.25 ml of (B) was filled in the syringe. The rest of both solution (A) and (B) were kept in the refrigerator at 4 °C to be used later for the reference experiment. The sample and the reference ampoule were introduced into the system in a 4 steps; at the first two

steps they were kept 10 min at each, 30 min at the third step before they were finally completely inserted at step 4. Then the stirrer was switched on at 70 rpm, and after thermal stabilization was achieved the first injection was executed by injecting 5 μ l of GSH solution in the ampoule. Thereafter, another 19 injections were reformed, each of them 10 μ l with a duration of 10 sec and intervals of 30 min. The reference experiment was performed exactly the same except that GSH was injected in 0.8 ml of 0.111 M KNO_3 with pH 3.5 instead of the uranium solution. The ITC experiment was performed with the same microcalorimetry instrument using the specified ITC-slot.

4.3.3 Continuous turbidity measurements

A real-time continuous OD₆₀₀ measurement for the turbidity of the *L. lactis* NZ9000(pNZ3203) was performed while being cultured in M17-G medium at 30 °C using the Circular Dichroism instrument JASCO J-815 CD spectrometer (JASCO, Germany). For the OD measurement, the cuvette of the CD was autoclaved with 70% ethanol and then filled with 3.5 ml of the medium as described in section 4.3.1, and inoculated with a volume of a pre-prepared culture so that the initial OD₆₀₀ equals 0.005. The culture was incubated in the CD instrument at 30 °C with stirring and the measurement of the OD₆₀₀ was taken each minute for 15 hours. This experiment was performed three times; one as a control that does not contain uranium, one with 100 μ M uranyl nitrate with nisin to induce GSH and one with 100 μ M uranyl nitrate without nisin.

4.4 Results

4.4.1 Metabolic activity of *L. lactis* in the presence of copper

Lactococcus lactis subsp. *cremoris* NZ9000 is a model organism that can neither synthesize GSH nor take it up from the medium. Its sensitivity towards oxidative stress, imposed by exogenous H_2O_2 , could be reduced by expressing a biosynthetic pathway for GSH (Fu et al., 2006). This was accomplished by expressing *Escherichia coli* *gshA* and *gshB*, encoding γ -glutamylcystein synthetase and GSH synthetase, respectively, from plasmid pNZ3202 under the control of a nisin-inducible promoter (Li et al., 2005). In this study, the effect of uranyl on the metabolic activity of this strain was measured in the absence and presence of nisin-induced intracellular GSH production. The intracellular GSH synthesis avoids the complications of extracellular addition of GSH, represented by metal complexation

by intracellular GSH and cellular uptake of GSH. GSH and uranyl are redox-active such that their intracellular fate will also be strongly affected by oxidative stress. To exclude this source of cellular damage, *L. lactis* NZ9000(pNZ3203), in which the role of GSH on uranyl toxicity can be studied in the absence of oxidative stress, was used. The effect of copper, for which the intracellular toxicity has been extensively characterized, was compared with that of uranyl in terms of heat flow in *L. lactis*. The calorimetric measurement of the effect of copper provides the thermal signature for metal-toxicity that is primarily related to the inhibition of sulfhydryl-carrying enzymes that require iron as a cofactor (Chillappagari et al., 2010; Macomber and Imlay, 2009; Macomber et al., 2007). In principle, uranyl toxicity could be the consequence of a similar cofactor displacement. The comparison with the thermal signature of copper toxicity can thus provide mechanistic information on uranyl toxicity.

The growth of *L. lactis* NZ9000(pNZ3203) was monitored by microcalorimetry in the presence of various concentrations of copper in the absence and presence of intracellular GSH. Figure 4-1 (A) shows thermograms for the growth of *L. lactis* at various copper concentrations in the absence of intracellular GSH (data are shown in Table 4-1) as a reference for later comparison with uranyl-toxicity. After a short lag phase, the metabolic heat production increases sharply and peaks after 8 to 10 h. The initial growth is followed by a short delay (shoulder at 8.5 h in the absence of copper), before rapid heat production is resumed. After that, the metabolic activity decreases by 90 % in the ensuing ~10 h. The two phases of logarithmic growth (or the diauxic growth) mark the sequentially consumption of different carbon sources, which causes a metabolic re-orientation of the cells when the carbon sources are beginning to get sparse during culture growth (29). The thermogram at 100 μM copper was unaffected in comparison to the control. At higher copper concentrations, the logarithmic growth and the maximal heat flow are reduced, causing to increasingly blurred distinction between the two exponential phases. Finally, at 400 μM and 800 μM copper, the peak heat flow is reduced to about 80% and 40 %, respectively, and the lag phase prolonged to about 20 h at the highest copper concentration.

Integration of the measured heat flow over time produces heat vs. time diagrams (Fig. 4-1 B). Assuming that the amount of heat produced during the formation of an individual bacterial cell stays constant during the entire growth phase, the total heat scales with the number of cells that produce this heat. Thus, this diagram approximates the increase in cell number during growth phase, as well as in the thermogram (Braissant et al., 2013).

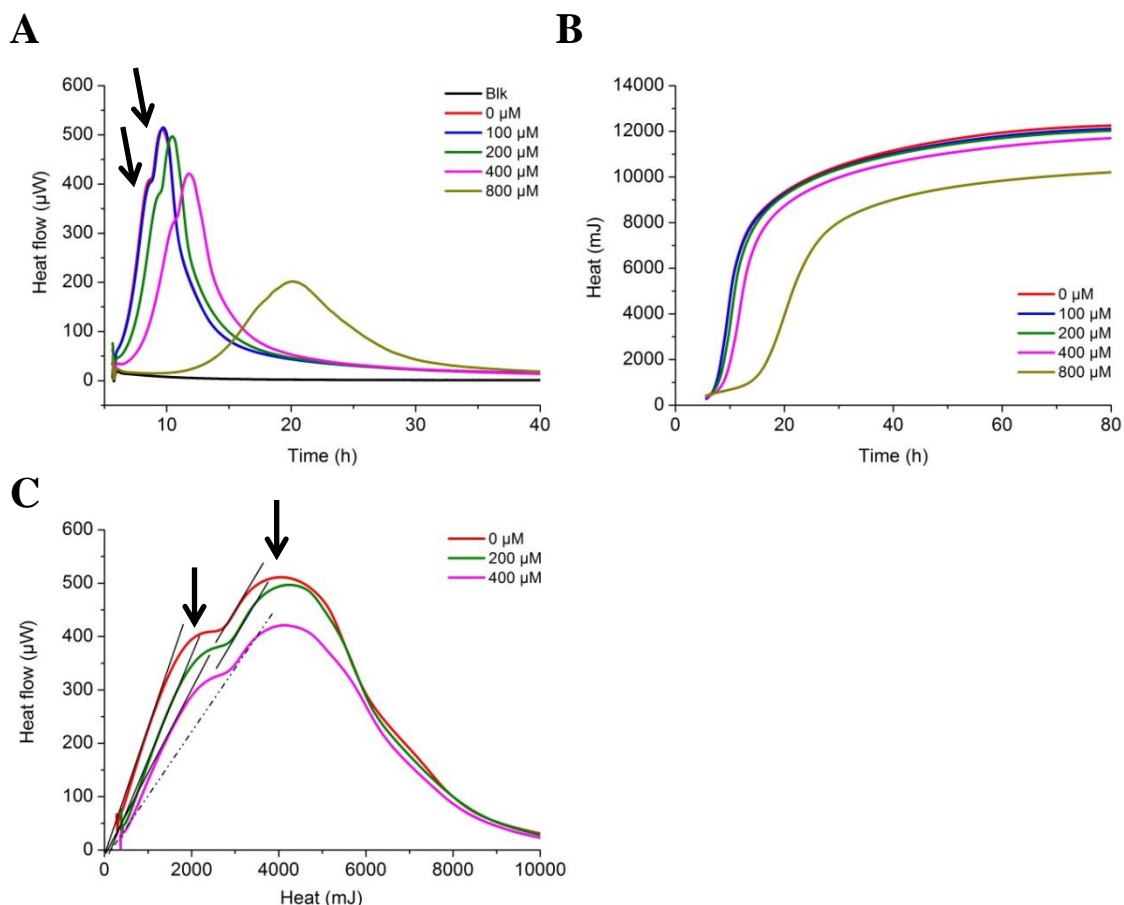


Figure 4-1: Copper dependence of the metabolic heat flow of *L. lactis* in the absence of nisin.

A: Heat flow is plotted vs. time. The strain NZ9000(pNZ3203) was cultured at 30 °C in 4 ml M17-G medium supplemented with 40 μl of 1 M Na-ascorbate, 10 μl of 200 mM cysteine. Copper was added as CuSO_4 at the indicated final concentrations (at 0 μM and 100 μM CuSO_4 , the traces are almost indistinguishable, bottom line: medium alone). Arrows indicate the end of the first and second phase of logarithmic growth. B: Total heat vs. time approximates the change in cell number. C: Heat flow vs. total heat is plotted for a subset of copper concentrations. Regression lines were calculated for the linear segments of the plot which correspond to the first and second phase of logarithmic growth. Rate constants for the two phases were derived from the slopes (Fig. 4-5).

The microcalorimetric measurements enable a much more accurate quantitative representation of bacterial growth than the traditional turbidity-based measurements do because the latter have a much lower signal-to-noise ratio. However, real-time turbidity measurements, when performed under equivalent conditions, can nevertheless provide important information on cell numbers in order to supplement calorimetric data as will be shown in section 4.4.4. Figure 4-1 C shows the heat flow vs. heat plot and the linear stretches that approximate the corresponding growth phases of the thermograms. The slopes of these stretches determine the underlying growth rates. The rate of the initial logarithmic growth decreases gradually from 0.89 h^{-1} in the absence of copper to 0.36 h^{-1} at the highest copper

concentration. In contrast, the second phase of logarithmic growth exhibits a slower rate of 0.44 h^{-1} which is little affected by copper up to $400 \mu\text{M}$ but strongly reduced at $800 \mu\text{M}$ (Table 4-1).

Table 4-1. CuSO_4 -dependent growth parameters of *L. lactis* 3203 in the absence of nisin; $T_{\text{max}}(\text{h})$, $P_{\text{max}}(\mu\text{W})$ and $k (\text{h}^{-1})$ together with percentage errors and inhibitory ratio related to each of them.

	$[\text{U}_{\text{nat}}]$ (μM)	T_{max} (h)	% Error of T_{max}	P_{max} (μW)	% Error of P_{max}	$K (\text{h}^{-1})$	R
Growth phase 1	0	-	-	-	-	0.892	0.999
	100	-	-	-	-	0.872	0.999
	200	-	-	-	-	0.789	0.999
	400	-	-	-	-	0.663	0.999
	800	-	-	-	-	0.357	0.999
Growth phase 2	0	9.633	0.093	511.057	0.443	0.443	0.998
	100	9.72	0.746	515.74	0.462	0.448	0.999
	200	10.44	0.019	496.785	0.297	0.483	0.999
	400	11.797	0.229	421.313	0.074	0.398	0.999
	800	20.012	3.043	205.57	4.423	0.146	0.997

Table 4-2. CuSO_4 -dependent growth parameters of *L. lactis* 3203 the presence of nisin; $T_{\text{max}}(\text{h})$, $P_{\text{max}}(\mu\text{W})$ and $k (\text{h}^{-1})$ together with percentage errors and inhibitory ratio related to each of them.

	$[\text{U}_{\text{nat}}]$ (μM)	T_{max} (h)	% Error of T_{max}	P_{max} (μW)	% Error of P_{max}	$K (\text{h}^{-1})$	R
Growth phase 1	0	-	-	-	-	0.828	0.999
	100	-	-	-	-	0.712	0.999
	200	-	-	-	-	0.561	0.998
	400	-	-	-	-	0.31	0.999
	800	-	-	-	-	0.276	0.999
Growth phase 2	0	8.796	0.284	523.346	0.667	0.519	0.998
	100	9.427	1.74	498.284	1.545	0.384	0.999
	200	10.763	0.455	409.343	0.712	0.46	0.999
	400	15.337	0	216.752	0.34	0.226	0.998
	800	52.557	6.004	137.113	18.351	0.107	0.998

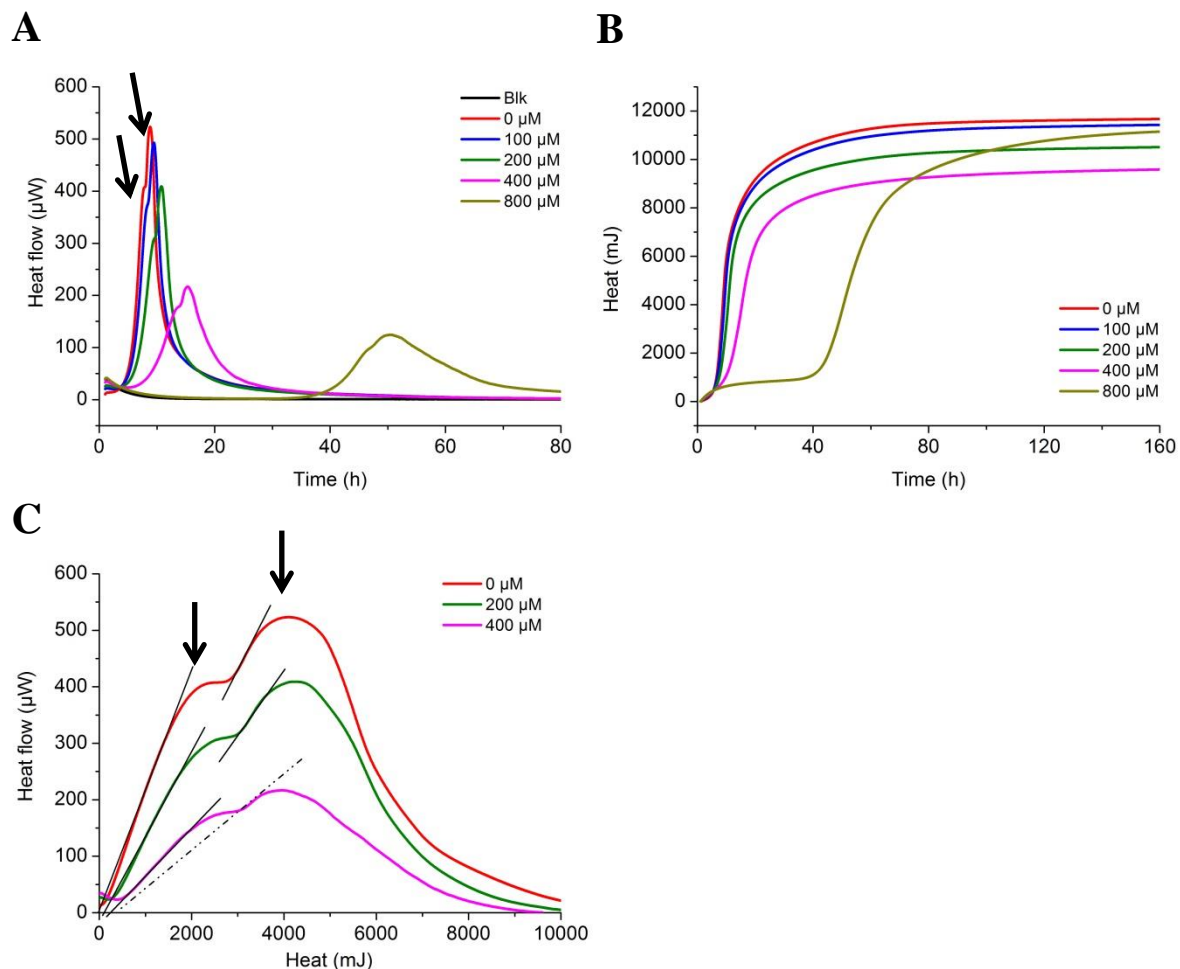


Figure 4-2: Copper dependence of the metabolic heat flow of *L. lactis* in the presence of nisin.

A: Heat flow is plotted vs. time. Bacterial strain and experimental conditions as in legend to Fig. 1 except for the presence of $0.55 \mu\text{M}$ nisin to induce GSH production. Copper was added as CuSO_4 at the indicated final concentrations (bottom line: medium alone). Arrows indicate the end of the first and second phase of logarithmic growth. B: Total heat vs. time plot approximating the change in cell number. C: Heat flow vs. total heat is plotted for a subset of copper concentrations. Regression lines were calculated for the linear segments of the plot which correspond to the first and second phase of logarithmic growth. Rate constants for the two phases were derived from the slopes (Fig. 4-5).

When GSH synthesis was induced by nisin, copper exhibited a more severe influence on the growth of *L. lactis*. While $100 \mu\text{M}$ copper did not affect the thermogram in the absence of GSH, $100 \mu\text{M}$ copper reduced and delayed the maximal heat flow in the presence of GSH (Fig. 4-2 A). These effects got more acute at higher copper concentrations. At $400 \mu\text{M}$ copper, the maximal heat flow was reduced and delayed to almost the same extent as by $800 \mu\text{M}$ copper in the absence of GSH. The increased sensitivity of metabolic heat production to copper in the presence of GSH is also reflected by the total heat production over time (Fig. 4-2 B). For example, the half-maximal heat production in the presence of $400 \mu\text{M}$ copper is

delayed by approximately 7 h and the final heat diminished by around 20%, compared to growth in the absence of GSH. Figure 4-2 (C) shows the plots of the heat flow vs. heat in the presence of GSH. The smaller slopes of the regression lines compared to their counterparts in Fig. 4-1 (C) demonstrate a stronger copper-dependent reduction of logarithmic growth in the presence of GSH (See Table 4-2).

4.4.2 Metabolic activity of *L. lactis* in the presence of uranyl.

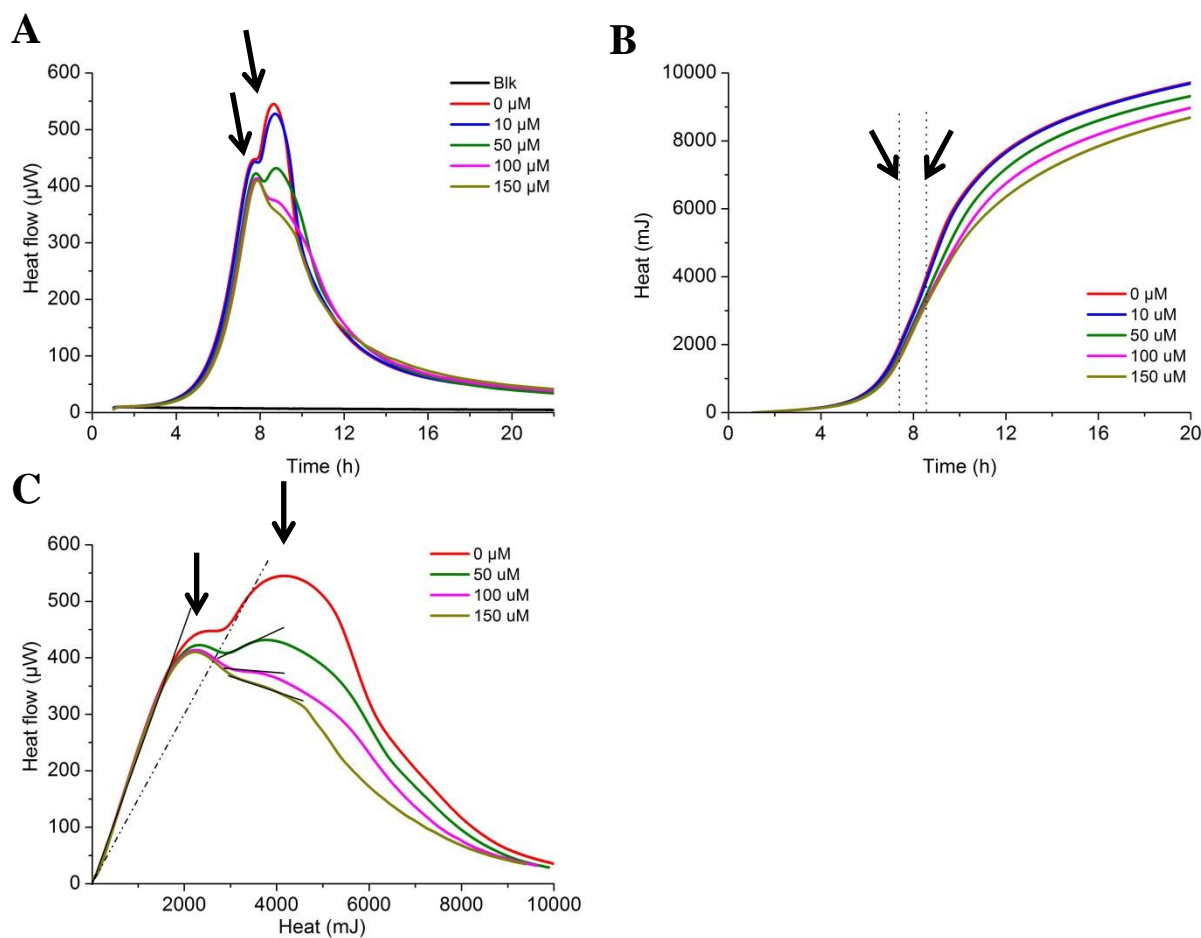


Figure 4-3: Uranyl dependence of the metabolic heat flow of *L. lactis* in the absence of nisin.

A: Heat flow is plotted vs. time. Bacteria were cultured under the conditions given in Fig. 1 except for the addition of $\text{UO}_2(\text{NO}_3)_2$ instead of CuSO_4 at the indicated final concentrations. Arrows indicate the end of the first and second phase of logarithmic growth. B: Total heat vs. time approximates the change in cell number. C: Heat flow vs. total heat is plotted for a subset of copper concentrations. Regression lines were calculated for the linear segments of the plot which correspond to the first and second phase of logarithmic growth. Rate constants for the two phases were derived from the slopes (Fig. 4-5).

To investigate the role of intracellular GSH on uranyl toxicity, experiments with uranyl nitrate similar to those described above for copper sulfate were performed. The experiments addressed the environmentally relevant low dose regime, i.e., uranyl concentrations in the 0-150 μM range. Figure 4-3 (A) shows the uranyl dependence of the thermograms of *L. lactis* in the absence of GSH. In contrast to copper, uranyl did not affect the initial logarithmic growth. However, it specifically reduced the maximal heat flow of the second exponential phase. The levels of total heat production in relation to the control without added metal (Fig. 4-3 B) show a successive reduction of the total heat with the increment of uranyl concentration. The specificity of uranyl toxicity for the second phase of logarithmic growth becomes obvious from the rate analysis in Fig. 3 (C). The regression lines for the first exponential heat production are indistinguishable, whereas the slopes of the regression lines for the later logarithmic growth are successively decreased by the addition of uranyl, as seen also in Table 4-3.

Table 4-3. $\text{UO}_2(\text{NO}_3)_2$ -dependent growth parameters of *L. lactis* 3203 in the absence of nisin; T_{max} (h), P_{max} (μW) and k (h^{-1}) together with percentage errors and inhibitory ratio related to each of them.

	[U_{nat}] (μM)	T_{max} (h)	% Error of T_{max}	P_{max} (μW)	% Error of P_{max}	K (h^{-1})	R
Growth phase 1	0	7.764	0.045	447.499	0.032	0.861	0.998
	10	7.751	0.039	442.941	0.068	0.864	0.998
	50	7.798	0.064	422.456	0.064	0.85	0.998
	100	7.827	0.198	413.782	0.427	0.876	0.998
	150	7.865	0.229	410.329	2.078	0.873	0.998
Growth phase 2	0	8.638	0.023	545.37	0.067	0.417	0.998
	10	8.706	0.006	527.69	0.167	0.376	0.998
	50	8.76	0.051	431.655	0.12	0.15	0.999
	100	-	-	-	-	-	-
	150	-	-	-	-	-	-

The thermal signatures that were obtained with the growth of *L. lactis* in the presence of either copper or uranium indicate fundamentally different toxicity mechanisms for the two heavy metals. This was also apparent when the cells synthesized GSH. Whereas GSH enhanced the sensitivity to copper, it reduced the sensitivity to uranyl. Figure 4-4 (A) shows

again that the initial logarithmic growth was barely affected by uranyl. However, the uranyl sensitivity of the second growth phase was clearly reduced by the induced GSH synthesis and the total heat production at 50 μM uranyl was almost indistinguishable from that without uranyl (Fig. 4-4 B).

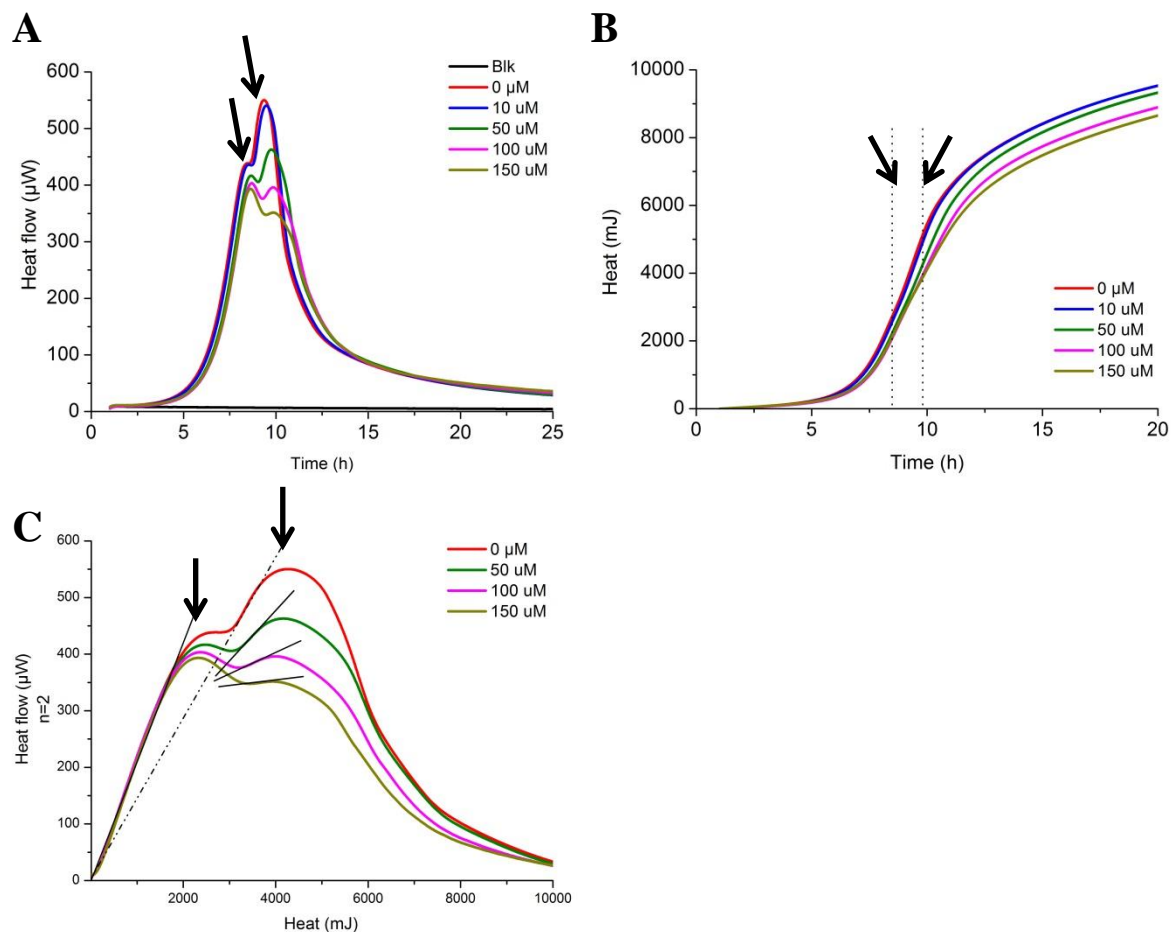


Figure 4-4: Uranyl dependence of the metabolic heat flow of *L. lactis* strain in the presence of nisin.

A: Heat flow is plotted vs. time. Bacteria were cultured under the conditions given in Fig. 3 except for the addition of $0.55 \mu\text{M}$ nisin to induce GSH production. $\text{UO}_2(\text{NO}_3)_2$ was added at the indicated final concentrations. Arrows indicate the end of the first and second phase of logarithmic growth. B: Total heat vs. time approximates the change in cell number in the presence of different uranyl concentrations (same data as in A). C: Heat flow vs. total heat is plotted for different uranyl concentrations (same data as in A). Regression lines were calculated for the linear segments of the plot which correspond to the first and second phase of logarithmic growth. Rate constants for the two phases were derived from the slopes (Fig. 4-5).

Correspondingly, linear stretches in the heat flow vs. heat plot (Fig. 4-4 C) exhibit a steeper slope in comparison to the data without GSH (Tables 4-4 and 4-3 respectively). Figure 4-5 summarizes the growth rates obtained from the regression analyses.

Table 4-4. $\text{UO}_2(\text{NO}_3)_2$ -dependent growth parameters of *L. lactis* 3203 in the presence of nisin; $T_{\max}(\text{h})$, $P_{\max}(\mu\text{W})$ and k (h^{-1}) together with percentage errors and inhibitory ratio related to each of them.

	$[\text{U}_{\text{nat}}]$ (μM)	T_{\max} (h)	% Error of T_{\max}	P_{\max} (μW)	% Error of P_{\max}	K (h^{-1})	R
Growth phase 1	0	8.474	0.23	438.654	0.187	0.814	0.999
	10	8.53	0.059	436.221	0.102	0.823	0.999
	50	8.68	0	416.037	0	0.814	0.999
	100	8.694	0.081	403.501	0.69	0.805	0.998
	150	8.627	0.371	393.688	0.089	0.8	0.998
Growth phase 2	0	9.36	0.224	550.317	0.256	0.492	0.998
	10	9.48	0	540.48	0.036	0.456	0.998
	50	9.748	0.328	462.984	0.315	0.275	0.996
	100	9.847	0.249	396.167	0.875	0.132	0.999
	150	9.854	0.249	351.638	0.54	0.036	0.995

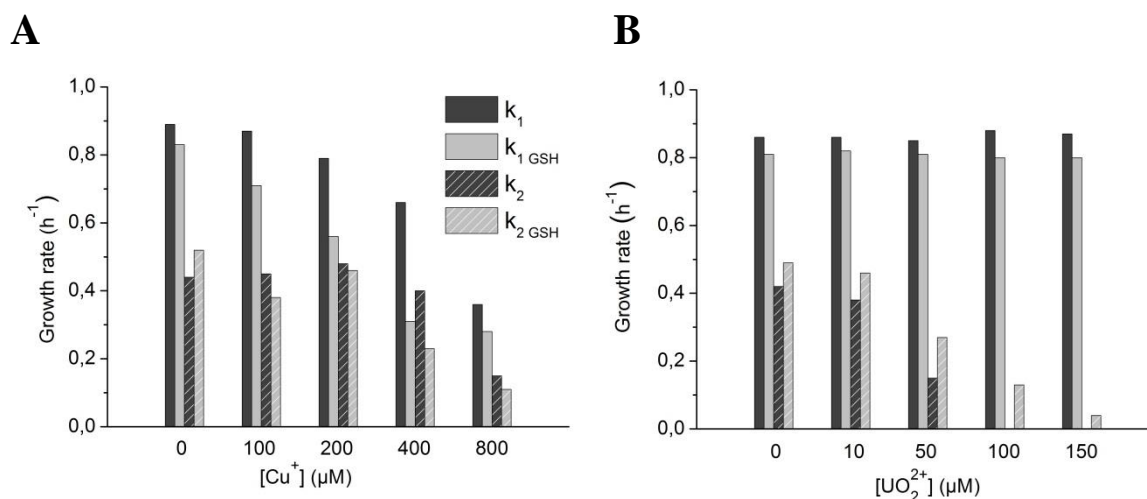


Figure 4-5: Comparison of growth rates during first and second phase of logarithmic growth.

A: Copper sensitivity of growth rates. B: Uranyl sensitivity of growth rates. All rates were determined from the linear stretches of the heat flow vs. heat diagrams in Figs. 1-4 (C). Regression coefficients were larger than 0.995 for all regression lines which covered at least 30 min of the respective growth phase. The difference in rates as determined from duplicate samples amounts to less than 2 % of the mean for all traces.

It is noteworthy that the linear regressions describing the second phase of logarithmic growth in the presence of uranyl did not form lines through the origin in the heat flow *vs.* heat plots. This is in contrast to the growth behavior seen with copper. More specifically, linear stretches in the heat flow *vs.* heat plot that do not intersect at the same point on the abscissa indicate that the dissipated heat per cell replication differs in the two logarithmic growth phases as will be discussed. The data evidences that both metals affect the cell in two different metabolic pathways.

In summary, the thermograms of the purely fermentative metabolism of *L. lactis* 3203 reveal uranyl toxicity already below 100 μM , i.e., at concentrations, at which copper has no effect on culture growth. GSH expression attenuates uranyl toxicity at these environmentally relevant concentrations. However, GSH enhances copper toxicity when the metal exceeds 100 μM . The data indicate that GSH acts in fundamentally different ways on the toxicity of the two metals.

4.4.3 Isothermal titration calorimetry of GSH uranyl complex formation.

The microcalorimetric data showed that GSH attenuates uranyl toxicity, indicating a possible direct interaction. Isothermal titration calorimetry was used to determine whether uranyl binding / reduction by GSH can be observed *in vitro*. Figure 4-6 (A) shows the heat flow changes upon injection of GSH aliquots into a uranyl nitrate solution at pH 3.5 (at which only one of the two carboxyl residues of GSH is ionized (Bismondo and Rizzo, 1992)). Each injection causes an endothermic signal evidencing a positive binding enthalpy. The evaluation of the integrated heat flow is consistent with a stoichiometry of 1:1 for the GSH-uranyl complex with $\Delta H = 18.6 \text{ kJ mol}^{-1}$ and $\Delta S = 87 \text{ J mol}^{-1}\text{K}^{-1}$. The data agree with previous estimates of these parameters obtained by a combination of potentiometry and bulk calorimetry for uranyl perchlorate. The binding entropy supports U(VI) carboxylate interactions (Bismondo and Rizzo, 1992). Binding of uranyl to the carboxyl functions of GSH rather than to the thiol group, which is protonated under the ITC conditions, has been inferred also from spectroscopy at near neutral pH (Frost et al., 2011). At pH 4.5, the formation of a fraction of GSH with two negatively charged carboxylates is expected. In this case, the interaction with uranyl leads to precipitation despite full solubility of uranyl and GSH alone (Fig. 4-6 B, inset). The ITC data indicate that in addition to the endothermic complex formation, uranyl-GSH polymers form in an exothermic reaction leading to precipitation.

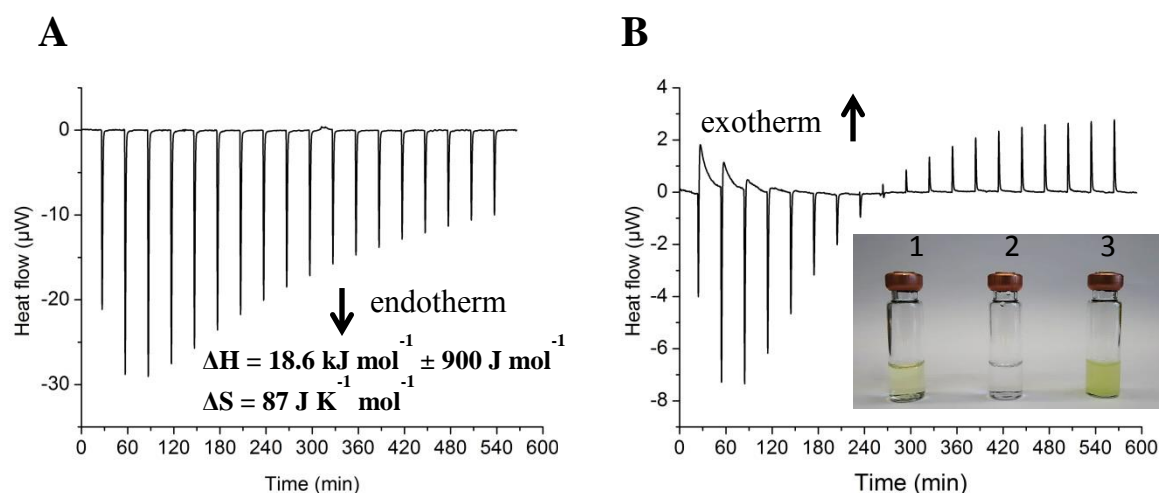


Figure 4-6: Isothermal titration calorimetry of GSH uranyl complex formation.

10 μL Aliquots of a 200 mM solution of GSH were injected into 5 mM uranyl nitrate at pH 3.5 (A) and pH 4.5 (B). The first injection was discarded from the evaluation in panel A. The parameters were obtained with a 1:1 stoichiometry using the instrument software TAM Assistant (Waters GmbH, Eschborn). Due to precipitation of GSH-uranyl complexes at pH 4.5, no evaluation was carried out. However, the data show the appearance of an exothermic (positive) signal, attributable to uranyl-mediated GSH oligomerization / precipitation in addition to the initial endothermic binding enthalpy. The inset shows the calorimetric ampoules containing uranyl nitrate, GSH and the precipitate formed upon injection of GSH into the uranyl solution at pH 4.5. No precipitate is formed at pH 3.5.

4.4.4 Continuous turbidity measurements

In order to relate the changes in the peaks of the thermograms to changes in biomass production, a continuous OD600 measurement was performed. This kind of turbidity measurement is more accurate than those traditionally performed (Braissant et al., 2013) because it was performed continuously during the cultivation time, although, with a lower time resolution than the calorimetry. Figure 4-7 (A) shows the process of biomass production over time (in blue), which resembles the heat curves versus time shown in the previous figures. On the other hand, its derivative (in black) resembles the thermogram as expected for heat flow being proportional to metabolic activity and thus to growth rate. By comparing the thermogram in the absence of uranyl to its counterpart, i.e., of the first derivative of the OD (Fig. 4-7 B), it is clear that the percentage ratio of the second peak to the first peak is almost equal in both cases (Table 4-5) and equals $\sim 130\%$. The addition of 100 μM uranyl lowered the height of the second peak causing to a decrement in this percentage ratio in both experiments (Fig. 4-7 C). However, it is obvious that this lowering was more severe in the turbidity curve than in the calorimetric curve. This provides clear evidence that, in the

presence of 100 μM uranyl, the dissipated heat flow per cell in the second growth phase was $\sim 30\%$ more than the biomass production in that phase, i.e. the biomass produced to the released heat ratio in the second peak is lower than that one of the first peak with $\sim 30\%$. This difference was maintained after the addition of nisin (Fig. 4-7 D), though the increment in the second peak in both curves. This indicates that the addition nisin-induced GSH has enhanced cell production, while the higher dissipated heat flow per cell was maintained.

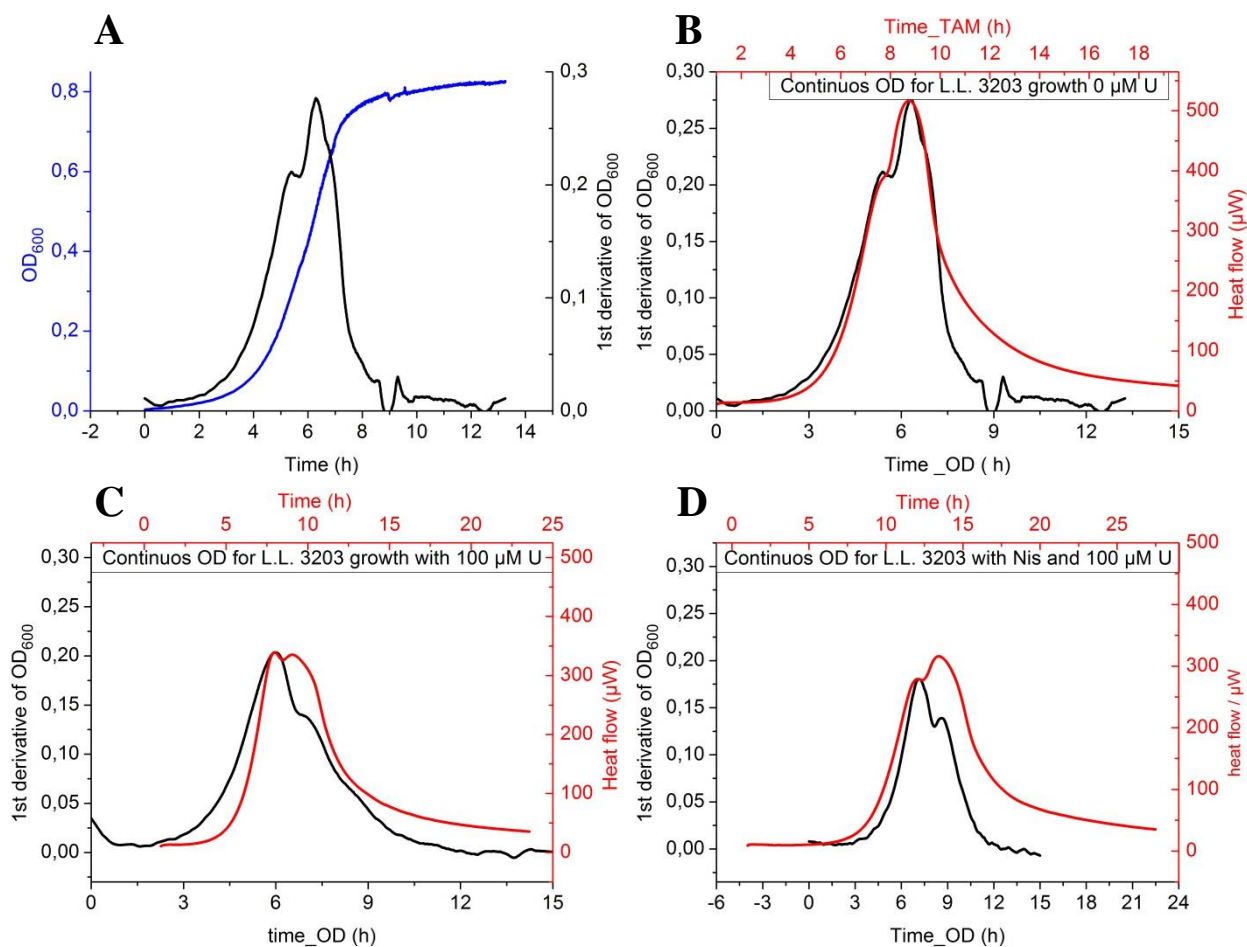


Figure 4-7: Comparison of biomass production and metabolic heat flow production of *L. lactis* 3203 strain under the stress of uranyl, and the role of GSH.

A: OD600 continuous measurement for the strain NZ9000-pNZ3203 cultured at 30 °C in 4 ml M17-G medium in blue, and its first derivative in black. It is clear that OD curve looks like the heat curves, while its derivative looks like thermograms.

First derivative of the continuous OD₆₀₀ measurement is plotted vs. time in black and heat flow is plotted vs. time in red. B: The strain NZ9000-pNZ3203 was cultured at 30 °C in 4 ml M17-G medium. C: additionally to (A) the culture was supplemented with 40 μl of 1 M Na-ascorbate, 10 μl of 200 mM cysteine. 100 μM $\text{UO}_2(\text{NO}_3)_2$ was added. D: in addition to (C) 0.55 μM Nisin was added to induce GSH production.

Table 4-5. $\text{UO}_2(\text{NO}_3)_2$ -dependent growth

[U _{nat}] (μM)		P _{max} (μW)	2nd to 1st P _{max} percent ratio %	OD _{600_max}	2nd to 1st OD _{600_max} percent ratio %
0 μM	1st peak	397.271	130.112	0.211	131,28
	2nd peak	516.898		0.277	
100 μM	1st peak	339.443	98,784	0.203	69,951
	2nd peak	335.314		0.142	
100 μM + nis	1st peak	279.101	113,188	0.18	77,222
	2nd peak	315.909		0.139	

4.5 Discussion

The role of GSH in modulating uranyl toxicity has been addressed by measuring the metabolic activity of a *L. lactis* strain in which GSH could be induced by the bacterial peptide nisin. In order to identify possible metabolic pathways of the modulation of uranium toxicity by GSH, similar experiments were also carried out with copper. Like uranium, copper is redox-active and can thus provide a reference for the toxicity of redox-active metals. However, it was demonstrated that copper toxicity is enhanced by GSH, whereas uranyl toxicity is attenuated under our conditions.

These results differ from those observed under conditions of aerobic respiration, under which GSH has been shown to exert a protective effect against copper toxicity both, in Gram-positive and Gram-negative organisms (Grosse et al., 2014; Potter et al., 2012). However, under the fermentative conditions employed here, GSH renders *L. lactis* 3203 more sensitive to copper at all stages of growth. This finding is not in line with the concept that GSH restrains copper toxicity by binding excess copper. Rather, GSH may bind copper and facilitate its delivery to metal binding sites of enzymes, a mechanism that has been well documented *in vitro* (Ciriolo et al., 1990; Ferreira et al., 1993; Musci et al., 1996). This is also the cause for copper toxicity in *E. coli*, rather than oxidative stress (Chillappagari et al., 2010; Macomber and Imlay, 2009; Macomber et al., 2007). The displacement of iron from enzymes may become particularly dominant in the case of the high (>100 mM) GSH concentrations reached in this *L. lactis* strain (Li et al., 2003) and at copper concentrations that exceed the

capacity of the export system. In contrast, the attenuation of uranyl toxicity by GSH suggests the formation of intracellular GSH-uranyl complexes as a detoxification mechanism. Such a complex formation is supported by the ITC results. The interaction of copper with GSH involves the sulfhydryl group rather than the strong Lewis bases (i.e., phosphates and carboxylates) that are preferred by the uranyl cation. The difference in coordination chemistry appears to be the primary reason for the different metabolic effects of copper and uranyl on culture growth and also for the adverse effects of GSH on the toxicity of the two metals.

The rates of the two logarithmic growth phases are differently affected by the two metals, demonstrating that copper and uranyl toxicity follow different biochemical patterns. Both toxicity mechanisms, however, are independent of ROS production. The lack of oxidative damage under copper stress has been documented for *Lactococcus lactis* (Mancini et al., 2014). Copper reduced the metabolic heat flow at both growth phases of the culture and delayed the attainment of maximal metabolic activity. In contrast, uranyl affected exclusively the second phase of logarithmic growth without delaying culture growth. This observation is attributed to a metabolic re-orientation of *L. lactis* 3203 such that uranyl inhibits an enzyme that is expressed only with the onset of this altered cellular metabolism (probably in response to the continuously changing medium composition during fermentation). Correspondingly, the action of GSH was restricted to that phase. In contrast to copper, the toxicity of uranium thus appears to be more selective and suggests that uranyl displaces non-sulfhydryl-binding metal-cofactors and / or occupies functionally important enzyme sites such as carboxyl residues or phosphates. Furthermore, copper affected growth only at concentrations above 100 μM , whereas uranyl toxicity was apparent already at environmentally relevant concentration of 10 μM . This difference likely reflects the lack of an efficient natural export system for uranyl, whereas a copper-exporting ATPase is present in *L. lactis* (Kelly et al., 2013).

Additionally, this remarkable difference in toxicity of uranium versus copper is qualitatively visible from a comparison of Figs. 4-1 (C) and 4-3 (C). The linear stretches in the heat flow vs. heat (P-Q) plot, which represent the two phases of logarithmic growth, project back to the origin in the presence of copper but not in the presence of uranium, for which the linear stretches of the second growth phase did not intersect at the same point on the abscissa. This indicates that the dissipated heat per cell replication differs in the two logarithmic growth phases. The dissipated heat during the growth phase is related to the cell

number, therefore, the more cells are produced with the same dissipated heat, the more efficient is the metabolism. Hence, the metabolic efficiency can be introduced as:

$$E = \frac{\Delta N}{\Delta Q} \quad (\text{Eq. 4-1})$$

Using equations 1-6: $P = m \cdot N$ and 1-8: $P = k \cdot Q + P_0$ then:

$$N = \frac{P}{m} = \frac{k \cdot Q + P_0}{m} = \frac{k}{m} \cdot Q + N_0 \quad (\text{Eq. 4-2})$$

$$E = \frac{\Delta N}{\Delta Q} = \frac{k}{m} \quad (\text{Eq. 4-3})$$

Thus, the growth rate can be expressed as $k = E \cdot m$. This relation expresses the intuitive notion that the growth rate is proportional to the metabolic activity of a cell. Toxic compounds will not abolish this proportionality, however, they are likely to change the amount of dissipated metabolic heat per cellular replication. Additional detoxifying reactions may occur, and protein expression may have to increase to compensate for enzyme inhibition, which will change the overall metabolic efficiency. This possibility is emphasized when comparing between the continuous turbidity results and the related thermograms, which showed that ~ 30 % more heat flow was dissipated in the presence of 100 μM uranyl regardless of the expression of GSH. Importantly, however, GSH re-enhanced the cell production in the presence of uranyl (evidenced by the turbidity measurements), such that the metabolic efficiency (number of cells produced per heat dissipated) increased again. The calorimetry-based estimate of the "metabolic efficiency" E provides an accurate measure of low dose toxicity because it is a direct measure of the energetic cost of a stressor and the energetic gain of a detoxifying mechanism.

The fact that GSH and GSSG levels are increased in uranyl-supplemented cultures of plant cells (Viehweger et al., 2011) or hepatocytes (Pourahmad et al., 2006) is a strong indication that GSH is involved in uranyl-detoxification also in higher organisms, in which uranyl toxicity has been related to oxidative stress (Miller et al., 2002). However, GSH-dependent detoxification mechanisms other than ROS suppression obviously need to be considered. In this study, it has been demonstrated that GSH participates in a uranyl detoxification mechanism that does not target ROS formation. The data indicate an enzyme-specific toxicity of U(VI), which is attenuated by GSH. Uranyl toxicity is expected to strongly

depend on uranyl solubility and thus on speciation. The sequestration into insoluble organic complexes as well as the reduction to insoluble uranyl species of oxidation states $< VI$ could thus provide efficient detoxification mechanisms for uranium. The ITC results together with other studies (Bismondo and Rizzo, 1992; Frost et al., 2011) provide evidence for complex formation and carboxylate-dependent coordinative polymerization of GSH with uranyl *in vitro*. Therefore, the results support the intracellular sequestration of the actinide in GSH-uranyl complexes as a detoxification pathway. Such complexes are expected to be insoluble at physiological pH because precipitation occurred already at $pH > 4$ *in vitro*. The preference of uranyl for the GSH carboxylates rather than the thiol group (Frost et al., 2011) as well as the presence of two carboxyl functions in GSH (allowing metal-coordinated polymer formation) appears to be crucial for intracellular uranyl sequestration. The different solubility and coordination modes would also explain why, unlike copper, uranyl is not transferred by GSH to sulfhydryl-containing enzymes. The different role of GSH in modulating metal toxicity is thus best described by its sequestering action towards carboxyl coordinated uranyl as adverse to GSH-mediated Fe-Cu-exchange in enzymes *via* sulfhydryl-bound copper. A direct reductive detoxification of uranyl by GSH can be excluded by the ITC data, which agree with carboxyl coordination and have strong pH dependence in a range where the reducing thiol group ($pK \sim 8$) is not affected. In addition, the uranyl-GSH precipitate formed at pH 4.5 maintained the yellow color typical of U(VI). However, this does not exclude the possibility that the initially sequestered GSH-uranyl complexes may be metabolically reduced in later steps.

4.6 Conclusions

A protective role of intracellular GSH against environmentally relevant concentrations of 10-150 μM uranium was demonstrated *via* microcalorimetric monitoring of the metabolic activity of *L. lactis* cultures. The fermentative metabolism studied here, demonstrates a uranyl detoxification mechanism that is not related to an oxidative stress response. Instead, direct sequestration of U(VI) by GSH appears to be the primary mechanism in attenuating uranyl toxicity. In the same concentration range, copper toxicity is negligible but is enhanced by GSH at higher copper load in agreement with GSH-mediated metal cofactor exchange at sulfhydryl-carrying enzymes. Thus, GSH interferes with metal toxicity by fundamentally different mechanisms for copper and uranium. The calorimetry-based evaluation of metabolic activity and efficiency can provide quantitative assessments of uranyl toxicity particularly at low doses.

Chapter 5

5 Measuring uranyl-sensitivity in the nematode *Caenorhabditis elegans*

5.1 Abstract

Recent approaches in radioecology address questions of transgenerational effects of long term low dose exposure of higher organisms in the environment. Here, it was attempted whether the development of a well-established model organism, the nematode *Caenorhabditis elegans*, can be followed by calorimetry and studied as a function of radio nuclide exposure. In this study a minimal food chain model was established, and microcalorimetry was used to monitor the metabolic activity of *C. elegans* from hatching of the eggs up to the larval stage feeding on non-metabolizing bacteria. Since *C. elegans* is genetically fully characterized, such studies will ultimately allow correlating radiotoxicity with genetic traits.

5.2 Introduction

In addition to the significant role that microorganisms play in altering the mobility of radionuclides (Lloyd and Macaskie, 2002b), their role as a part of a food chain leads to the hazards of exposure of other organisms to the radionuclides through direct or indirect feeding on bacteria. This makes the transit of radionuclides from the geosphere to the food chain a key issue in radioecology research. Another key issue is the distinction between the chemical and radiotoxicity of radionuclides incorporated by an organism at low doses. To address both aspects, a minimal food chain model using a bacterial strain of *E. coli* as a food source for the nematode *Caenorhabditis elegans* was established in the presence of varying concentrations of natural uranium and the ^{233}U isotope. *C. elegans* was chosen, because it is a well-known organism that is genetically fully characterized (Consortium, 1998; Sakashita et al., 2010), and thus a good *in vivo* model system. This advantage opened the doors widely for investigating the effects of ionizing radiation in *C. elegans* during the last four decades. These investigations have focused on radiation-induced mutations and DNA damage (Sakashita et al., 2010) using different external ionizing radiation beam sources for irradiation (Hartman,

1985; Herman et al., 1976; Takanami et al., 2003). Other studies were performed to investigate the effect of uranium on *C. elegans* (Goussen et al., 2013; Jiang et al., 2009). In both studies the nematodes were exposed to uranium through the medium not through the bacteria. On the other hand, the assessment of environmentally relevant low dose radiotoxicity is a major challenge in radioecology. In this low-dose regime, classical survival-based methods can hardly be applied because lethality is typically not present under such environmentally realistic conditions. In contrast, metabolic responses to radio- and chemitoxicity may provide an extremely sensitive real-time monitor of detrimental effects of radionuclides. However, except the work of Braeckman *et al.*, in which they used calorimetry to measure the metabolic rate (Braeckman et al., 2002), there is no published work that studied and characterized the metabolic activity in *C. elegans* with calorimetry to show the metabolism-related thermal signature of its life cycle. Nevertheless, this should not be an obstacle because a very basic comparison that highlights the differences between the control and a population of the nematode exposed to either U_{nat} or ^{233}U would be sufficient in this case.

In this work, the heat released by the metabolic activity of the nematode was measured by calorimetry during maturation of eggs and growth of the larval stage feeding on bacteria. These experiments were performed in the presence of varying concentrations of natural uranium and the ^{233}U isotope.

5.3 Materials and Methods

The *C. elegans* strain N2 was obtained from the Caenorhabditis Genetics Center (Minneapolis, MN) and grown in nematode growth medium (NGM). Worms were bleached and 2000 eggs collected in microcalorimeter ampoules that included 140 μl M9, nonmetabolizing medium, and 60 μl of *E. coli* strain NA22 culture with $\text{OD}_{600} = 20$, resulting in final volume 200 μl . For each experiment the samples were prepared in duplicates. One blank sample that contained only 200 μl M9 medium were run in order to check its sterility and three samples, one with medium and bacteria only, and two with *C. elegans* without any uranium were run as controls. Natural uranium or ^{233}U was added from 0.1 mM uranyl nitrate stock solutions at final concentrations of 1–13 μM resulting in less than 0.01 Bq and 17–261 Bq per sample, respectively. Ampoules were inserted in a TAM-III microcalorimeter (TA-Instruments, Eschborn, Germany) as described in chapter 2. The culture was incubated at 25 $^{\circ}\text{C}$ and heat flow measured over five to six days.

5.4 Results and Discussion

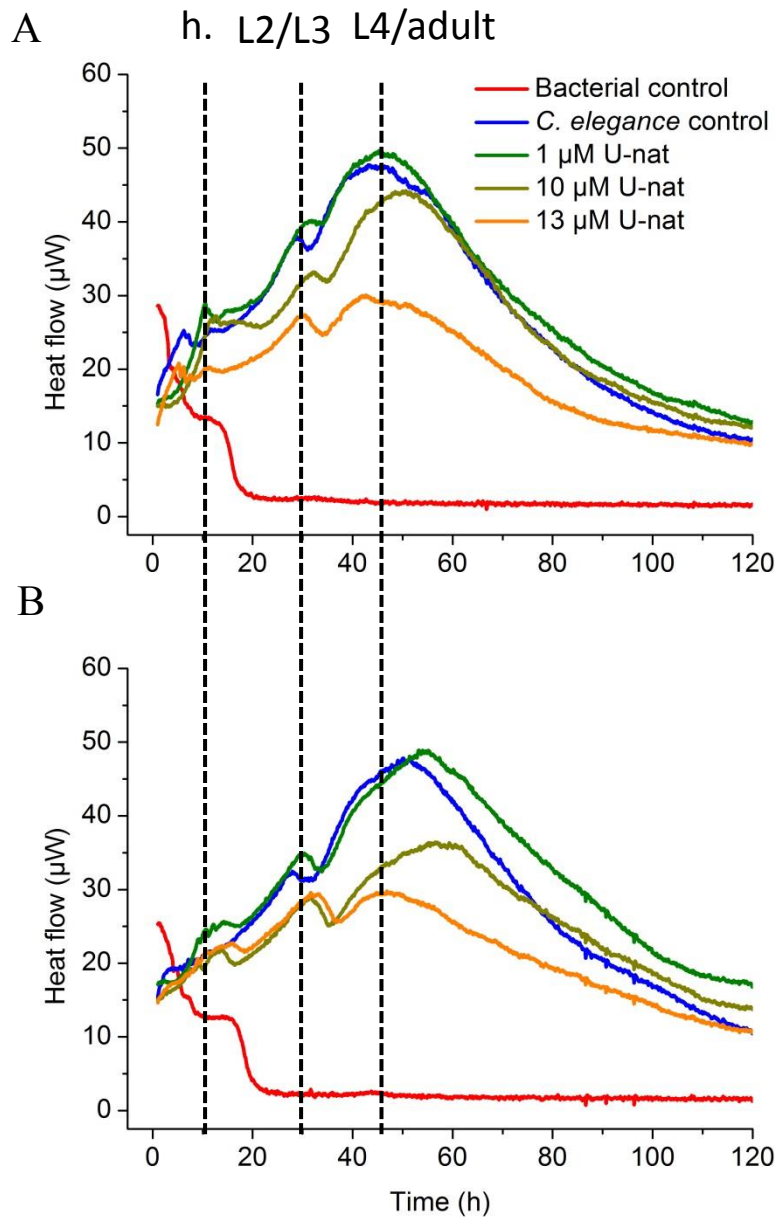


Figure 5-1: Metabolic heat flow of developing *C. elegans* under the effect of different uranium isotopes with different concentration.

A: Heat flow is plotted vs. time. Bacteria were co-cultured at 25 °C in ~ 0.2 ml culture of *C. elegans* with the presence of different concentrations of (A): U-nat and (B): ^{233}U . The dashed lines refer to: h: hatching, L2 / L3: L2 / L3 molt and L4 / ad: L4 / adult molt.

Figure 5-1 shows the effect of uranium sources (A) for natural uranium and (B) for ^{233}U . Since non-metabolizing conditions for the bacteria were chosen (no carbon source in M9 medium), the thermograms are attributable exclusively to the nematode metabolism. A

sufficient description for the thermal signature for the metabolic activity of *C. elegans* needs good knowledge and experience about its development and behavior along its life cycle. Unfortunately, this kind of description is not available at the moment due to the lack of thermal studies of *C. elegans*, yet the signatures of the thermograms can be correlated to the life cycle of *C. elegans* using the well-defined time scale for its development. Figure 5-2 shows the life cycle of *C. elegans* together with the time of each transformation stage (Altun and Hall, 2009).

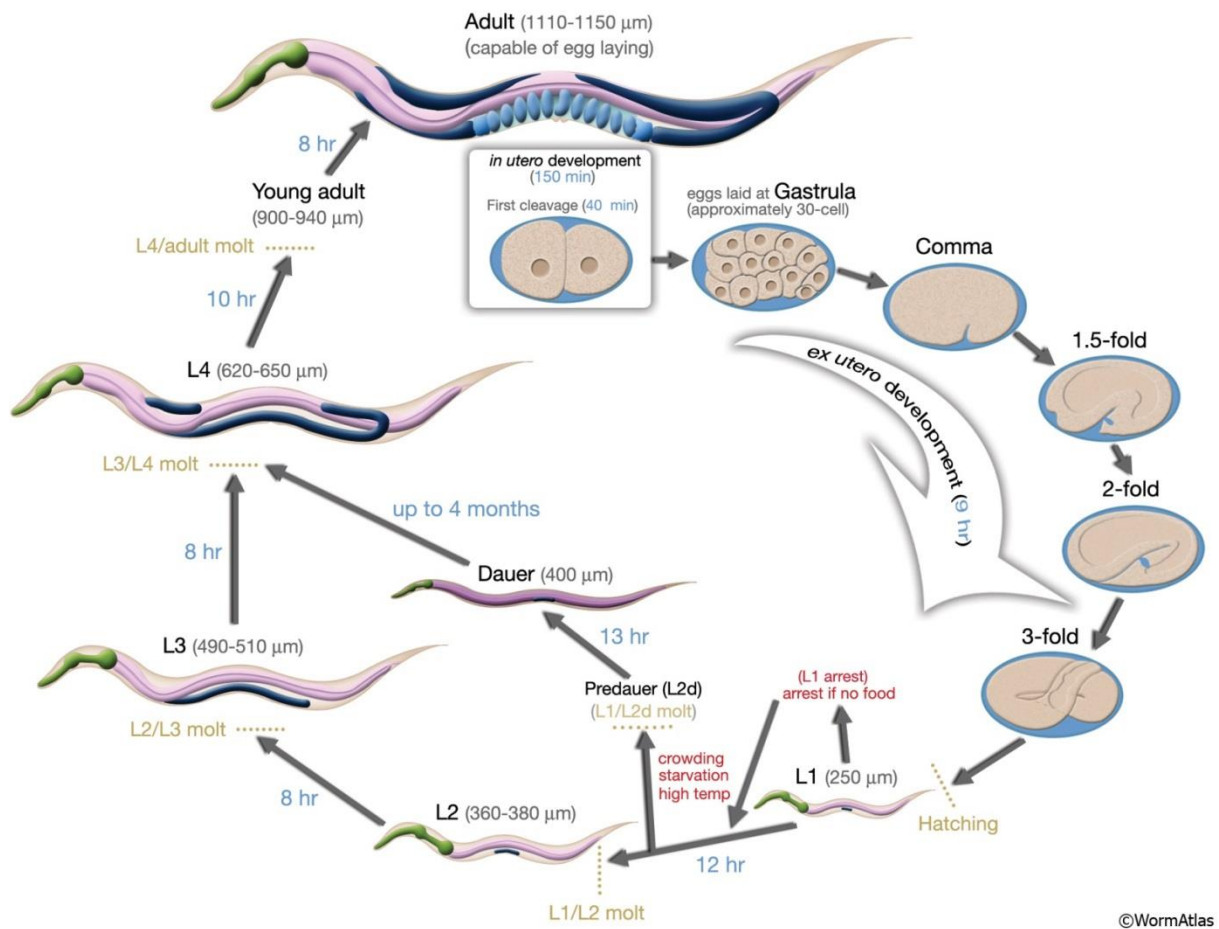


Figure 5-2: Life cycle development of *C. elegans* grown at 22 °C with the related duration of each transformation stage.

This figure shows the development of *C. elegans* from egg to adult, and it was used to relate each developmental stage to its thermal signature shown in Fig. 5-1. This figure was adapted from worm atlas website:

<http://www.wormatlas.org/hermaphrodite/introduction/Introframeset.html>

By comparing these two figures, hatching of eggs is expected ~11 h after insertion of the samples into the calorimeter (Fig. 5-1 dotted line h). A complete development to an adult is expected after ~46 h from hatching. However, a maximal heat flow showed up after ~38 h from hatching, which is assigned according to Figure 5-2 to the L4 / adult molt (Fig. 5-1 dotted line L4/ad). The proceeding rise in heat flow can thus be assigned to growth of the first

and second larval states L1 and L2 ending with the L2/L3 molt which is assigned here to the peak in heat flow at ~30 h (Fig. 5-1 dotted line L2/L3). The thermograms in Fig. 5-1 (A) and (B) do not show a clear delay in the peaks neither among different concentrations of the same uranium isotope nor between the two different uranium isotopes. Rather, it was the height of the heat flow that was affected by uranium. The time course and the increase of heat flow during the L1 and L2 stage is little affected by the different uranium isotopes. However, the thermogram that covers the growth of the L3 larval stage after ~30 h was clearly affected by the radionuclides if their concentration exceeded 1 μM . Natural uranium at 10 μM caused a slight delay and a decrease for the maximal heat flow, which was typically observed after ~48 h. At the same concentration, ^{233}U is formally twice as effective as natural uranium with respect to both reduction and delay of the maximal heat flow. Remarkably, at 13 μM both uranium sources showed the same effect, and the related thermograms were almost identical.

The experiments show for the first time that the calorimetric approach has a great potential for radioecology because it allows establishing complex *in vivo* systems as demonstrated here for a well-defined food chain model.

5.5 Conclusions

The study showed that *C. elegans* was affected with slight differences at low dose concentrations of both natural uranium and the strong α -emitter ^{233}U . Clearly, microcalorimetry allows a highly sensitive distinction of radio- and chemitoxic effects in a multicellular organism. Here the thermograms can be interpreted as an average signal that represents the metabolic state of one individual. This is different from the bacterial studies where lethality and proliferation coexist and thermograms reflect the state of the population rather than individual cells. In the case of ^{233}U toxicity in *C. elegans* it is likely that individual cells become lethally damaged by the α -particles but the organism survived by cell replacement or by surviving a small number of cell loss. The study has laid the ground for more detailed analyses of radionuclide-dependent metabolic effects in radioecologically important model organisms, with the present limited information on uranyl effects in *C. elegans*.

Conclusions

The aim of this work was to quantify and distinguish the effects of low doses radiotoxicity on microorganisms and higher organisms. Motivated by the existence of microorganisms in an environment polluted by heavy metals and raises the following questions about metabolic response of microorganisms to these pollutants:

- Are the bacterial strains that exist in a uranium waste pile adapted to uranium toxicity, and how would low doses of uranium affect the metabolic activity of these strains?
- Is it possible to differentiate radiotoxicity from chemotoxicity of uranium?
- Is it possible to identify molecular mechanisms that mediate the detoxification of radionuclides?
- How are radionuclides transferred to the food chain?

The investigations were carried out using isothermal microcalorimetry to monitor the metabolic activity of the organisms during their growth under the stress of uranium. The data showed that isothermal microcalorimetry-based evaluation of metabolic activity is powerful method to quantitative assessments of uranyl toxicity particularly at low doses, when traditional methods based on survivals counting and turbidity measurements stand powerless in the absence of lethality. The data also showed to which degree this non-specific instrument that monitors the overall metabolic heat released from the sample can be related to highly specific metabolic pathways of an organism when combined with genetic engineering, providing a very important breakthrough in the applications of this instrument in the field of living systems.

Through this project, bacterial strains and nematodes were used as model organisms to perform the investigation. The bacterial-growth parameters of the thermograms were studied deeply, which might help setting a standard experimental protocol for investigating toxicity by providing correct interpretation for these parameters when relating them to the toxicological effects, bacteriostat and bactericide. While bacteriostatic effect is related to a change in the growth rate, retardation is related to bactericidal effect, cell cycle arrest or

Conclusions

metabolic reorientation accompanied with change of growth rate. On the other hand, the maximal heat flow indicates a change in the metabolic activity, or in the effective volume of the medium.

At the beginning, the toxicity of natural uranium was investigated at concentration range 0.1–150 μM . The results show that metabolic effects can be measured at environmentally-relevant nuclide concentrations down to the sub-micro-molar range. The investigated strains showed adaptation mechanisms to uranium at low concentrations up to 10 – 50 μM where the effectiveness limit of this adaptation was reached, after which purely uranium-inhibited phase with decreasing growth rates and metabolic activity and increasing growth retardation were predominant. However, if the waste pile isolate has evolved these specific defense mechanisms against U, the data show that they were evolved exclusively for chemitoxicity, but not for radiotoxicity. That is because the affinity of the surface protein S-layer to uranium, which protects the cell by preventing uranium from penetrating into the cell, will play a negative role in the presence of radiotoxicity due to the accumulated α -particle source on the cell surface. The data showed that radiotoxicity is about 100 times greater than chemical toxicity in strain JG-B53. On the other hand, the data showed the protective role of GSH against these environmentally relevant concentrations of uranium. While the production of intercellular GSH enhanced tolerance to uranium, it has enhanced the sensitivity to copper.

Finally unlike bacteria, there is a lack of information about the thermal signature of growth of nematodes. Nevertheless, the data showed that *C. elegans* was affected by both uranium isotopes U_{nat} and ^{233}U with slight differences. The reason is that in case of ^{233}U individual cells will get affected by the α -particles but the organism survived by cell replacement or by surviving a small number of cell loss.

Outlooks

The interesting results revealed by this project opened the door for further investigations:

- Investigating the defensive mechanism observed in Chapter 2 by studying the changes in the molecular level in the cells to address the molecules and proteins that stand behind this action using two-dimensional electrophoresis, and later to try to improve this mechanism through genetic engineering.
- Investigating other model organisms that are known to be resistance toward radiotoxicity like *Deinococcus radiodurans* and *Tardigrada*.
- Investigating the toxicity of alpha particles (different alpha particle emitters that have different energies) would be interesting and would allow studying the relation between the energy of alpha particle and its relative biological effectiveness (RBE).
- Investigating the food chain with one of the isolated strain instead of *E. coli*, by growing the strain in the presence of uranium, washing them and then add them as a food source to the nematodes.
- Investigating the developments of animal eggs (fish, frogs ...) and plant seeds under the stress of radiotoxicity and use it to address transgenerational effects of long term low dose exposure of higher organisms in the in the environment.
- Finally, since *C. elegans* responds physiologically and morphologically to different stress situations, the effect of radionuclides will be particularly addressed during formation of draught-resistant dauer state, where heavy metals may get further concentrated. It was shown that under these conditions lipid head-groups are altered to interact preferentially with a cryo-protective disaccharide trehalose (Sharkh, 2015). Molecular mechanisms of cellular uranyl uptake are expected to critically depend on the metal-coordinating properties of these membrane constituents which will be further studied *in vitro* to complement the *in vivo* data.

References

- Alklint, C., et al., 2005. Accelerated storage and isothermal microcalorimetry as methods of predicting carrot juice shelf-life. *Journal of the Science of Food and Agriculture*. 85, 281-285.
- Alpen, E. L., Chapter 6 - Radiation Chemistry. In: E. L. Alpen, (Ed.), *Radiation Biophysics (Second Edition)*. Academic Press, San Diego, 1998, pp. 104-131.
- Altun, Z. F., Hall, D. H., 2009. Introduction to *C. elegans* Anatomy. In *WormAtlas*. <http://www.wormatlas.org/hermaphrodite/introduction/Introframeset.html>.
- Baldoni, D., et al., 2009. Performance of Microcalorimetry for Early Detection of Methicillin Resistance in Clinical Isolates of *Staphylococcus aureus*. *Journal of Clinical Microbiology*. 47, 774-776.
- Barbero, A., et al., 2005. Experimental and mathematical study of the influence of growth factors on the growth kinetics of adult human articular chondrocytes. *Journal of Cellular Physiology*. 204, 830-838.
- Basset, C., et al., 2013. Revision of the Biodistribution of Uranyl in Serum: Is Fetuin-A the Major Protein Target? *Chemical Research in Toxicology*. 26, 645-653.
- Bentley, K. W., et al., 1985. Transient Proteinuria and Aminoaciduria in Rodents Following Uranium Intoxication. *Bulletin of Environmental Contamination and Toxicology*. 34, 407-416.
- Bismondo, A., Rizzo, L., 1992. Thermodynamics of the Complex-Formation between Uranyl(Vi) and Some Polypeptides in Aqueous-Solution. *Thermochemica Acta*. 196, 131-136.
- Braeckman, B. P., et al., 2002. Assessing metabolic activity in aging *Caenorhabditis elegans*: concepts and controversies. *Aging Cell*. 1, 82-88.
- Braissant, O., et al., 2013. Microbial growth and isothermal microcalorimetry: Growth models and their application to microcalorimetric data. *Thermochemica Acta*. 555, 64-71.
- Braissant, O., et al., 2014. Seven Hours to Adequate Antimicrobial Therapy in Urosepsis Using Isothermal Microcalorimetry. *Journal of Clinical Microbiology*. 52, 624-626.
- Braissant, O., et al., 2010a. "The heat is on": Rapid microcalorimetric detection of mycobacteria in culture. *Tuberculosis*. 90, 57-59.
- Braissant, O., et al., 2010b. Use of isothermal microcalorimetry to monitor microbial activities. *Fems Microbiology Letters*. 303, 1-8.
- Brenner, D. J., 2009. Extrapolating Radiation-Induced Cancer Risks from Low Doses to Very Low Doses. *Health Physics*. 97, 505-509.
- Brenner, D. J., 2011. We don't know enough about low-dose radiation risk. *Nature*. Published online 5 April 2011.
- Brenner, D. J., et al., 2003. Cancer risks attributable to low doses of ionizing radiation: Assessing what we really know. *Proceedings of the National Academy of Sciences of the United States of America*. 100, 13761-13766.
- Brenner, D. J., Sachs, R. K., 2006. Estimating radiation-induced cancer risks at very low doses: rationale for using a linear no-threshold approach. *Radiation and Environmental Biophysics*. 44, 253-256.

References

- Bricheux, G., et al., 2013. Microcalorimetry: A powerful and original tool for tracking the toxicity of a xenobiotic on *Tetrahymena pyriformis*. *Ecotoxicology and Environmental Safety*. 98, 88-94.
- Buckton, G., 1995. Applications of Isothermal Microcalorimetry in the Pharmaceutical Sciences. *Thermochimica Acta*. 248, 117-129.
- Changela, A., et al., 2003. Molecular basis of metal-ion selectivity and zeptomolar sensitivity by CueR. *Science*. 301, 1383-1387.
- Cheeseman, K. H., Slater, T. F., 1993. An Introduction to Free-Radical Biochemistry. *British Medical Bulletin*. 49, 481-493.
- Chillappagari, S., et al., 2010. Copper Stress Affects Iron Homeostasis by Destabilizing Iron-Sulfur Cluster Formation in *Bacillus subtilis*. *Journal of Bacteriology*. 192, 2512-2524.
- Christensen, D. M., et al., 2014. Ionizing Radiation Injuries and Illnesses. *Emergency Medicine Clinics of North America*. 32, 245-+.
- Ciriolo, M. R., et al., 1990. Reconstitution of Cu,Zn-Superoxide Dismutase by the Cu(I).Glutathione Complex. *Journal of Biological Chemistry*. 265, 11030-11034.
- Clarkson, T. W., Kench, J. E., 1956. Urinary Excretion of Amino Acids by Men Absorbing Heavy Metals. *Biochemical Journal*. 62, 361-372.
- Consortium, C. e. S., 1998. Genome sequence of the nematode *C-elegans*: A platform for investigating biology. *Science*. 282, 2012-2018.
- Contingencies, A. D., 2009. Alpha and Beta Ranges. Retrived on 25.08.2015 from: <http://www.alpharubicon.com/basicnbc/article16radiological71.htm>.
- Cothorn, R. C., Lappenbusch, W. L., 1983. Occurrence of Uranium in Drinking Water in the US. *Health Physics*. 45, 89-99.
- Criddle, R. S., et al., 1988. Effects of Temperature and Oxygen Depletion on Metabolic Rates of Tomato and Carrot Cell-Cultures and Cuttings Measured by Calorimetry. *Plant Cell and Environment*. 11, 695-701.
- Dameron, C. T., Harrison, M. D., 1998. Mechanisms for protection against copper toxicity. *American Journal of Clinical Nutrition*. 67, 1091s-1097s.
- Dauncey, M., et al., 1978. A human calorimeter for the direct and indirect measurement of 24 h energy expenditure. *British Journal of Nutrition*. 39, 557-566.
- Domingo, J. L., 2001. Reproductive and developmental toxicity of natural and depleted uranium: a review. *Reproductive Toxicology*. 15, 603-609.
- Domingo, J. L., et al., 1987. Acute Toxicity of Uranium in Rats and Mice. *Bulletin of Environmental Contamination and Toxicology*. 39, 168-174.
- Domingo, J. L., et al., 1989. The Developmental Toxicity of Uranium in Mice. *Toxicology*. 55, 143-152.
- Donnelly, E. H., et al., 2010. Acute Radiation Syndrome: Assessment and Management. *Southern Medical Journal*. 103, 541-544.
- Duff, M. C., et al., 1997. The chemistry of uranium in evaporation pond sediment in the San Joaquin Valley, California, USA, using X-ray fluorescence and XANES techniques. *Geochimica Et Cosmochimica Acta*. 61, 73-81.
- Duwat, P., et al., 2001. Respiration capacity of the fermenting bacterium *Lactococcus lactis* and its positive effects on growth and survival. *Journal of Bacteriology*. 183, 4509-4516.
- Ebbs, S. D., et al., 1998. Role of uranium speciation in the uptake and translocation of uranium by plants. *Journal of Experimental Botany*. 49, 1183-1190.
- Eckerman, K., et al., 2013. ICRP Publication 119: Compendium of Dose Coefficients based on ICRP Publication 60. *Annals of the ICRP*. 42, e1-e130.
- Eisenbud, M., Gesell, T., Chapter 1 - Introduction. In: M. E. Gesell, (Ed.), *Environmental Radioactivity (Fourth Edition)*. Academic Press, San Diego, 1997a, pp. 1-9.

References

- Eisenbud, M., Gesell, T., Chapter 6 - Natural Radioactivity. In: M. E. Gesell, (Ed.), Environmental Radioactivity (Fourth Edition). Academic Press, San Diego, 1997b, pp. 134-200.
- Fahey, R. C., et al., 1978. Occurrence of Glutathione in Bacteria. *Journal of Bacteriology*. 133, 1126-1129.
- Ferreira, A. M. D., et al., 1993. Copper(I) Transfer into Metallothionein Mediated by Glutathione. *Biochemical Journal*. 292, 673-676.
- Forbisher, M., 1965. Growth of microorganisms. In: *Fundamentals of microbiology*. Chapter 16.
- Forrest, W., 1961. Calorimeter for the continuous study of the heat production of microbial systems. *Journal of Scientific Instruments*. 38, 143.
- Frost, L., et al., 2011. Interaction of uranium (VI) towards glutathione—an example to study different functional groups in one molecule. *Proceedings in Radiochemistry A Supplement to Radiochimica Acta*. 1, 357-362.
- Fu, R. Y., et al., 2006. Introducing glutathione biosynthetic capability into *Lactococcus lactis* subsp. *cremoris* NZ9000 improves the oxidative-stress resistance of the host. *Metabolic Engineering*. 8, 662-671.
- Gao, W. M., Francis, A. J., 2008. Reduction of uranium(VI) to uranium(IV) by clostridia. *Applied and Environmental Microbiology*. 74, 4580-4584.
- Garedeu, A., et al., 2004. Microcalorimetric investigation on the antimicrobial activity of honey of the stingless bee *Trigona* spp. and comparison of some parameters with those obtained with standard methods. *Thermochimica Acta*. 415, 99-106.
- Gilbert, B. C., et al., 1984. The oxidation of some polysaccharides by the hydroxyl radical: an ESR investigation. *Carbohydrate research*. 125, 217-235.
- Goddu, S. M., et al., 1997. *MIRD Cellular S. Values* (Book). Society of Nuclear Medicine. Appendix III, 172-178.
- Goussen, B., et al., 2013. Consequences of a multi-generation exposure to uranium on *Caenorhabditis elegans* life parameters and sensitivity. *Ecotoxicology*. 22, 869-878.
- Grosse, C., et al., 2014. Survival of *Escherichia coli* Cells on Solid Copper Surfaces Is Increased by Glutathione. *Applied and Environmental Microbiology*. 80, 7071-7078.
- Guan, Y. H., et al., 1999. A calorimetric flow vessel optimised for measuring the metabolic activity of animal cells. *Thermochimica Acta*. 332, 211-220.
- Handley-Sidhu, S., et al., 2010. A review of the environmental corrosion, fate and bioavailability of munitions grade depleted uranium. *Science of the Total Environment*. 408, 5690-5700.
- Hartman, P. S., 1985. Epistatic Interactions of Radiation-Sensitive (Rad) Mutants of *Caenorhabditis-Elegans*. *Genetics*. 109, 81-93.
- Harvey, R. B., et al., 1986. Acute Toxicity of Uranyl-Nitrate to Growing Chicks - a Pathophysiological Study. *Bulletin of Environmental Contamination and Toxicology*. 37, 907-915.
- Helbig, K., et al., 2008. Cadmium toxicity in glutathione mutants of *Escherichia coli*. *Journal of Bacteriology*. 190, 5439-5454.
- Herman, R. K., et al., 1976. Chromosome Rearrangements in *Caenorhabditis-Elegans*. *Genetics*. 83, 91-105.
- Holzel, R., et al., 1994. Kinetic Investigations of Microbial-Metabolism by Means of Flow Calorimeters. *Thermochimica Acta*. 239, 17-32.
- Honglin, Z., et al., 1995. Establishment of Experimental-Model of Bacterial-Growth under Inhibitory Conditions - Study of Optimum Growth Temperature. *Journal of Thermal Analysis*. 44, 105-109.

References

- Howell, M., et al., 2012. Application of a Microcalorimetric Method for Determining Drug Susceptibility in Mycobacterium Species. *Journal of Clinical Microbiology*. 50, 16-20.
- IAEA, 2010. Radiation Biology: A Handbook for Teachers and Students. INTERNATIONAL ATOMIC ENERGY AGENCY. TRAINING COURSE SERIES No. 42.
- IAEA, 2015. Live Chart of Nuclides.
- Jiang, G. C. T., et al., 2009. Caenorhabditis elegans Metallothioneins Protect against Toxicity Induced by Depleted Uranium. *Toxicological Sciences*. 111, 345-354.
- Johansson, P., Wadso, I., 1999. Towards more specific information from isothermal microcalorimetric measurements on living systems. *Journal of Thermal Analysis and Calorimetry*. 57, 275-281.
- Karnebogen, M., et al., 1993. Microcalorimetric investigations on isolated tumorous and non-tumorous tissue samples. *Thermochimica Acta*. 229, 147-155.
- Kelly, W. J., et al., 2013. Interaction between the genomes of Lactococcus lactis and phages of the P335 species. *Frontiers in Microbiology*. 4.
- Kemp, R. B., 1991. Calorimetric Studies of Heat-Flux in Animal-Cells. *Thermochimica Acta*. 193, 253-267.
- Kemp, R. B., Guan, Y. H., 2000. The application of heat flux measurements to improve the growth of mammalian cells in culture. *Thermochimica Acta*. 349, 23-30.
- Kemp, R. B., Lamprecht, I., 2000. La vie est donc un feu pour la calorimetrie: half a century of calorimetry - Ingemar Wadso at 70. *Thermochimica Acta*. 348, 1-+.
- Kimura, T., Takahashi, K., 1985. Calorimetric Studies of Soil Microbes - Quantitative Relation between Heat Evolution during Microbial-Degradation of Glucose and Changes in Microbial Activity in Soil. *Journal of General Microbiology*. 131, 3083-3089.
- Knoll, G. F., 2010. Radiation detection and measurement. John Wiley & Sons.
- Kratz, J.-V., Lieser, K. H., 2013. Nuclear and radiochemistry fundamentals and applications third edition Chapter 1.
- Kuen, B., et al., 1997. Molecular characterization of the Bacillus stearothermophilus PV72 S-layer gene sbsB induced by oxidative stress. *Journal of bacteriology*. 179, 1664-1670.
- Latinwo, L. M., et al., 1998. Effects of intracellular glutathione on sensitivity of Escherichia coli to mercury and arsenite. *Biochemical and Biophysical Research Communications*. 242, 67-70.
- Lederer, F. L., et al., 2013. Identification of multiple putative S-layer genes partly expressed by Lysinibacillus sphaericus JG-B53. *Microbiology-Sgm*. 159, 1097-1108.
- Li, W. B., et al., 2009. Radiation dose assessment of exposure to depleted uranium. *Journal of Exposure Science and Environmental Epidemiology*. 19, 502-514.
- Li, Y., et al., 2003. Glutathione protects Lactococcus lactis against oxidative stress. *Applied and Environmental Microbiology*. 69, 5739-5745.
- Li, Y., et al., 2005. Using Lactococcus lactis for glutathione overproduction. *Applied Microbiology and Biotechnology*. 67, 83-90.
- Lin, G. M., et al., 2011. Microcalorimetry studies on the antibacterial effect of crude monkshood polysaccharide. *Journal of Zhejiang University-Science B*. 12, 563-567.
- Llobet, J. M., et al., 1991. Influence of Chronic Exposure to Uranium on Male Reproduction in Mice. *Fundamental and Applied Toxicology*. 16, 821-829.
- Lloyd, J. R., Macaskie, L. E., 2002a. Biochemical basis of microbe-radionuclide interactions. In: *Interactions of bacteria with radionuclides*. Elsevier Science, Oxford, UK. 313 - 342.
- Lloyd, J. R., Macaskie, L. E., Chapter 11 Biochemical basis of microbe-radionuclide interactions. In: M. J. Keith-Roach, F. R. Livens, Eds.), *Radioactivity in the Environment*. Elsevier, 2002b, pp. 313-342.

References

- Macomber, L., Imlay, J. A., 2009. The iron-sulfur clusters of dehydratases are primary intracellular targets of copper toxicity. *Proceedings of the National Academy of Sciences of the United States of America*. 106, 8344-8349.
- Macomber, L., et al., 2007. Intracellular copper does not catalyze the formation of oxidative DNA damage in *Escherichia coli*. *Journal of bacteriology*. 189, 1616-1626.
- Mancini, S., et al., 2014. Copper resistance and its regulation in the novel sulfate reducing bacterium *Desulfosporosinus* sp. OT. *J. Bacteriology*, in preparation.
- Markich, S. J., 2002. Uranium speciation and bioavailability in aquatic systems: an overview. *The Scientific World Journal*. 2, 707-729.
- McClain, D. E., et al., 2001. Biological effects of embedded depleted uranium (DU): summary of Armed Forces Radiobiology Research Institute research. *Science of the Total Environment*. 274, 115-118.
- McDiarmid, M. A., et al., 2000. Health effects of depleted uranium on exposed Gulf War veterans. *Environmental Research*. 82, 168-180.
- Merroun, M. L., et al., 2005. Complexation of uranium by cells and S-layer sheets of *Bacillus sphaericus* JG-A12. *Applied and Environmental Microbiology*. 71, 5532-5543.
- Merroun, M. L., Selenska-Pobell, S., 2008. Bacterial interactions with uranium: An environmental perspective. *Journal of Contaminant Hydrology*. 102, 285-295.
- Miller, A. C., et al., 2002. Depleted uranium-catalyzed oxidative DNA damage: absence of significant alpha particle decay. *Journal of Inorganic Biochemistry*. 91, 246-252.
- Monod, J., 1949. The Growth of Bacterial Cultures. *Annual Review of Microbiology*. 3, 371-394.
- Monti, M., 1990. Application of Microcalorimetry to the Study of Living Cells in the Medical Field. *Thermochimica Acta*. 172, 53-60.
- Monti, M., et al., 1980. Microcalorimetric measurement of production heat in isolated human adipocytes. *Scan. J. clin. Lab. Invest*. 40, 581-587.
- Murigande, C., et al., 2009. A Comparison Between (3H)-thymidine Incorporation and Isothermal Microcalorimetry for the Assessment of Antigen-induced Lymphocyte Proliferation. *Immunological Investigations*. 38, 67-75.
- Musci, G., et al., 1996. Reconstitution of ceruloplasmin by the Cu(I)-glutathione complex. Evidence for a role of Mg²⁺ and ATP (vol 271, pg 1972, 1996). *Journal of Biological Chemistry*. 271, 9870-9870.
- Nieboer, E., Richardson, D. H. S., 1980. The replacement of the nondescript term 'heavy metals' by a biologically and chemically significant classification of metal ions. *Environmental Pollution Series B, Chemical and Physical*. 1, 3-26.
- Parrish, R. R., et al., 2008. Depleted uranium contamination by inhalation exposure and its detection after similar to 20 years: Implications for human health assessment. *Science of the Total Environment*. 390, 58-68.
- Paternain, J. L., et al., 1989. The Effects of Uranium on Reproduction, Gestation, and Postnatal Survival in Mice. *Ecotoxicology and Environmental Safety*. 17, 291-296.
- Penninckx, M. J., Elskens, M. T., 1993. Metabolism and functions of glutathione in microorganisms. *Adv. Microb. Physiol*. 34, 239-301.
- Pollmann, K., et al., 2006. Metal binding by bacteria from uranium mining waste piles and its technological applications. *Biotechnology advances*. 24, 58-68.
- Pollmann, K., et al., 2005. Novel surface layer protein genes in *Bacillus sphaericus* associated with unusual insertion elements. *Microbiology-Sgm*. 151, 2961-2973.
- Potter, A. J., et al., 2012. *Streptococcus pneumoniae* Uses Glutathione To Defend against Oxidative Stress and Metal Ion Toxicity. *Journal of Bacteriology*. 194, 6248-6254.
- Pourahmad, J., et al., 2006. A search for cellular and molecular mechanisms involved in depleted uranium (DU) toxicity. *Environmental Toxicology*. 21, 349-354.

References

- Prado, A. G. S., Airoidi, C., 2000. Effect of the pesticide 2,4-D on microbial activity of the soil monitored by microcalorimetry. *Thermochimica Acta*. 349, 17-22.
- Raff, J., 2010. Bioinspired nanomaterials. https://nano.tu-dresden.de/pubs/slides_others/2010_11_11_Johannes_Raff.pdf.
- Raff, J., et al., 2005. Uranium binding by S-layer carrying isolates of the genus *Bacillus*. Annual Report Forschungszentrum Dresden-Rossendorf.
- Raff, J., et al., 2006. Uranium binding by cells and S-layer proteins of two *Bacillus* isolates and their corresponding reference strains. Annual Report Forschungszentrum Dresden-Rossendorf.
- Regan, M. D., et al., 2013. A simple and affordable calorespirometer for assessing the metabolic rates of fishes. *Journal of Experimental Biology*. 216, 4507-4513.
- Reitz, T., 2011. U(VI) bioaccumulation by *Paenibacillus* sp. JG-TB8 and *Sulfolobus acidocaldarius*; Au(0) nanoclusters formation on the S-layer of *S. acidocaldarius*. Ph.D. Thesis
- Reitz, T., et al., Interactions of *Paenibacillus* sp. and *Sulfolobus acidocaldarius* strains with U(VI). In: B. Merkel, A. Hasche-Berger, (Eds.), *Uranium, Mining and Hydrogeology*. Springer Berlin Heidelberg, 2008, pp. 703-710.
- Reitz, T., et al., 2014. Decrease of U(VI) Immobilization Capability of the Facultative Anaerobic Strain *Paenibacillus* sp JG-TB8 under Anoxic Conditions Due to Strongly Reduced Phosphatase Activity. *Plos One*. 9.
- Riley, P. A., 1994. Free-Radicals in Biology - Oxidative Stress and the Effects of Ionizing-Radiation. *International Journal of Radiation Biology*. 65, 27-33.
- Robinson, K. G., et al., 1998. Impact of organic ligands on uranium removal during anaerobic biological treatment. *Water Science and Technology*. 37, 73-80.
- Rong, X. M., et al., 2007. Isothermal microcalorimetry: A review of applications in soil and environmental sciences. *Pedosphere*. 17, 137-145.
- Sakashita, T., et al., 2010. Radiation Biology of *Caenorhabditis elegans*: Germ Cell Response, Aging and Behavior. *Journal of Radiation Research*. 51, 107-121.
- Santoro, R., et al., 2011. Real-Time Measurements of Human Chondrocyte Heat Production During In Vitro Proliferation. *Biotechnology and Bioengineering*. 108, 3019-3024.
- Schuler, M. M., et al., 2012. Investigation of the potential of biocalorimetry as a process analytical technology (PAT) tool for monitoring and control of Crabtree-negative yeast cultures. *Applied Microbiology and Biotechnology*. 93, 575-584.
- Selenska-Pobell, S., Chapter 8 Diversity and activity of bacteria in uranium waste piles. In: M. J. Keith-Roach, F. R. Livens, (Eds.), *Radioactivity in the Environment*. Elsevier, 2002, pp. 225-254.
- Selenska-Pobell, S., et al., 1999. Selective accumulation of heavy metals by three indigenous *Bacillus* strains, *B. cereus*, *B. megaterium* and *B. sphaericus*, from drain waters of a uranium waste pile. *Fems Microbiology Ecology*. 29, 59-67.
- Sharkh, S. E. A., 2015. SPECTROSCOPIC & THERMODYNAMIC INVESTIGATIONS OF THE PHYSICAL BASIS OF ANHYDROBIOSIS IN CAENORHABDITIS ELEGANS DAUER LARVAE. Technische Universität Dresden.
- Sivaprakasam, S., et al., 2011. Biocalorimetry as a process analytical technology process analyser; robust in-line monitoring and control of aerobic fed-batch cultures of crabtree-negative yeast cells. *Journal of Thermal Analysis and Calorimetry*. 104, 75-85.
- Sleytr, U. B., Beveridge, T. J., 1999. Bacterial S-layers. *Trends in microbiology*. 7, 253-260.
- Stulova, I., et al., The effect of milk heat treatment on the growth characteristics of lactic acid bacteria. *Agronomy Research*, Vol. 9. Estonian Research Institute of Agriculture, 2011, pp. 473-478.

References

- Suhr, M., 2015. Isolierung und Charakterisierung von Zellwandkomponenten der gram-positiven Bakterienstämme *Lysinibacillus sphaericus* JG-A12 und JG-B53 und deren Wechselwirkungen mit ausgewählten relevanten Metallen und Metalloiden. Technische Universität Dresden.
- Suhr, M., et al., 2014. Investigation of metal sorption behavior of Slp1 from *Lysinibacillus sphaericus* JG-B53: a combined study using QCM-D, ICP-MS and AFM. *Biometals*. 27, 1337-1349.
- Takahashi, K., 1990. Application of Calorimetric Methods to Cellular Processes - with Special References to Quantitative-Evaluation of Drug-Action on Living Cells. *Thermochemica Acta*. 163, 71-80.
- Takahashi, K., 2000. Calorimetric characterization of the inhibitory action of antimicrobial drugs and a proposal of a bacteriostatic / bactericidal index. *Netsu Sokutei*. 27, 8.
- Takanami, T., et al., 2003. Efficient repair of DNA damage induced by heavy ion particles in meiotic prophase I nuclei of *Caenorhabditis elegans*. *Journal of Radiation Research*. 44, 271-276.
- Thun, M. J., et al., 1985. Renal Toxicity in Uranium Mill Workers. *Scandinavian Journal of Work Environment & Health*. 11, 83-90.
- Trampuz, A., et al., 2007. Rapid diagnosis of experimental meningitis by bacterial heat production in cerebrospinal fluid. *Bmc Infectious Diseases*. 7.
- Tubiana, M., 2005. Dose-effect relationship and estimation of the carcinogenic effects of low doses of ionizing radiation: The joint report of the Académie des Sciences (Paris) and of the Académie Nationale de Médecine. *International Journal of Radiation Oncology*Biology*Physics*. 63, 317-319.
- Tubiana, M., et al., 2006. Recent reports on the effect of low doses of ionizing radiation and its dose-effect relationship. *Radiation and Environmental Biophysics*. 44, 245-251.
- Valsami-Jones, E., Ragnarsdottir, K. V., 1997. Solubility of uranium oxide and calcium uranate in water, and Ca(OH)₂-bearing solutions. *Radiochimica Acta*. 79, 249-257.
- Vandenhove, H., et al., 2006. Oxidative stress reactions induced in beans (*Phaseolus vulgaris*) following exposure to uranium. *Plant Physiology and Biochemistry*. 44, 795-805.
- Vanhoudt, N., et al., 2008. Effects of uranium and phosphate concentrations on oxidative stress related responses induced in *Arabidopsis thaliana*. *Plant Physiology and Biochemistry*. 46, 987-996.
- Vemuri, N. M., et al., 2004. Use of isothermal microcalorimetry in pharmaceutical preformulation studies - Part I. Monitoring crystalline phase transitions. *Journal of Thermal Analysis and Calorimetry*. 78, 47-54.
- Vidaud, C., et al., 2005. Screening of human serum proteins for uranium binding. *Chemical Research in Toxicology*. 18, 946-953.
- Viehweger, K., et al., 2011. Impact of uranium (U) on the cellular glutathione pool and resultant consequences for the redox status of U. *Biometals*. 24, 1197-1204.
- von Ah, U., et al., 2009. Isothermal micro calorimetry - a new method for MIC determinations: results for 12 antibiotics and reference strains of *E. coli* and *S. aureus*. *Bmc Microbiology*. 9.
- Wadso, I., 1985. Isothermal Biocalorimetry - a Status-Report. *Thermochemica Acta*. 88, 35-48.
- Wadso, I., 1995. Microcalorimetric techniques for characterization of living cellular systems. Will there be any important practical applications? *Thermochemica Acta*. 269, 337-350.
- Wadso, I., 1997. Trends in isothermal microcalorimetry. *Chemical Society Reviews*. 26, 79-86.

References

- Wadso, I., 2002. Isothermal microcalorimetry in applied biology. *Thermochimica Acta*. 394, 305-311.
- Wadso, I., 2009. Characterization of Microbial Activity in Soil by Use of Isothermal Microcalorimetry. *Journal of Thermal Analysis and Calorimetry*. 95, 843-850.
- Wadso, I., Goldberg, R. N., 2001. Standards in isothermal microcalorimetry (IUPAC technical report). *Pure and Applied Chemistry*. 73, 1625-1639.
- Wadso, L., Galindo, F. G., 2009. Isothermal calorimetry for biological applications in food science and technology. *Food Control*. 20, 956-961.
- Wadso, L., et al., 2004. Measurements on two mould fungi with a calorespirometric method. *Thermochimica Acta*. 422, 63-68.
- Webster, N., 2004. *The New International Webster's Comprehensive Dictionary of the English Language*. Imprint von Karl Müller Verlag. ISBN-10: 3-89893-979-0.
- Wirkner, S., Takahashi, K., 2000. Some Theoretical Considerations on Calorimetrically Determined Bactericidalities of Antimicrobial Drugs and Its Concentration Dependence. *Netsu Sokutei*. 27, 179-185.
- Wirkner, S., et al., 2001. Calorimetric Analysis of the Effect of ^{60}Co γ -rays on the Growth of *Saccharomyces cerevisiae*. *Netsu Sokutei*. 28, 7.
- Wirkner, S., et al., 2002. Calorimetric study on the effect of ^{60}Co γ -rays on the growth of microorganisms. *Radiation Physics and Chemistry*. 63, 327-330.
- Xie, C. L., et al., 1988. Microcalorimetric Study of Bacterial-Growth. *Thermochimica Acta*. 123, 33-41.
- Xu, H., et al., 2014. Microcalorimetric investigation on antibacterial activity of the peptide from *Plutella xylostella*. *Journal of Thermal Analysis and Calorimetry*. 115, 2463-2470.
- Yang, L. N., et al., 2008. Microcalorimetric studies on the antimicrobial actions of different cephalosporins. *Journal of Thermal Analysis and Calorimetry*. 93, 417-421.
- Zhang, J., et al., 2007. Glutathione protects *Lactococcus lactis* against acid stress. *Applied and Environmental Microbiology*. 73, 5268-5275.
- Zhang, T.-D., et al., 2012. Effects of tourmaline on growth of three kinds of microorganisms. *African Journal of Biotechnology*. 11.
- Zhao, Y. L., et al., 2014. Microcalorimetry coupled with chemometric techniques for toxicity evaluation of *Radix Aconiti Lateralis Preparata* (Fuzi) and its processed products on *Escherichia coli*. *Applied Microbiology and Biotechnology*. 98, 437-444.

Appendix

Publications:

- 1- Muhammad Hassan Obeid, Jana Oertel, Marc Solioz, Karim Fahmy, Expression of glutathione in *Lactococcus lactis* attenuates uranyl toxicity, submitted to the Applied and Environmental Microbiology, under revision.

Conferences and meetings:

- 1- Obeid, M. H.; Geissler, A.; Solioz, M.; Fahmy, K.; Oertel, J., Influence of low (radio)metal concentrations on bacterial growth using calorimetric metabolic monitoring
Jahrestagung der Deutschen Gesellschaft für Biophysik, 23.-26.09.2012, Göttingen, Germany. (Poster)
- 2- Bilaterales meeting IRE-IRS, Adaptation of bacterial strains to low_doses of uranium inferred from microcalorimetry, 05.-06.06.2014, Leibniz Universität Hannover, Hannover, Germany. (Talk)
- 3- Seminar “Microcalorimetry in Life Science”, Microcalorimetric Determination of Low Dose Radiotoxicity: From Bacterial Phenotypes to Molecular Mechanisms, 16.10.2014, the Biozentrum, Basel University, Switzerland in Basel University, Basel, Switzerland. (Talk)

Declaration

I herewith declare that I have produced this paper without the prohibited assistance of third parties and without making use of aids other than those specified; notions taken over directly or indirectly from other sources have been identified as such.

This paper has not previously been presented in identical or similar form to any other German or foreign examination board. The thesis work was conducted from February the 4th, 2012 to October the 22nd, 2015 under the supervision of Prof. Dr. Karim Fahmy at department of Biophysics, HZDR Institute. I declare that I have not undertaken any previous unsuccessful doctorate proceedings. I declare that I recognize the doctorate regulations of the Faculty of Science of Dresden University of Technology.

Dresden, October the 27th, 2015

Muhammad Hassan Obeid

Erklärung

Hiermit versichere ich, dass ich die vorliegende Arbeit ohne unzulässige Hilfe Dritter und ohne Benutzung anderer als der angegebenen Hilfsmittel angefertigt habe; die aus fremden Quellen direkt oder indirekt übernommenen Gedanken sind als solche kenntlich gemacht. Die Arbeit wurde bisher weder im Inland noch im Ausland in gleicher oder ähnlicher Form einer anderen Prüfungsbehörde vorgelegt.

Die Dissertation wurde im Zeitraum vom 4. Februar 2012 bis 22. Oktober 2015 verfasst und von Prof. Dr. Karim Fahmy, am Abteilung Biophysik , HZDR institut. Meine Person betreffend erkläre ich hiermit, dass keine früheren erfolglosen Promotionsverfahren stattgefunden haben. Ich erkenne die Promotionsordnung der Fakultät für Mathematik und Naturwissen-Schaften der Technischen Universität Dresden an.

Dresden, den 27. Oktober 2015

Muhammad Hassan Obeid